QUENCH - DEBRIS: Scientific Report NUSAFE 3572

Results of the QUENCH-DEBRIS (QUENCH-17) test with strongly oxidized Zircaloy-4 and hafnium claddings filled with segmented pellet simulators

J. Stuckert, M. Große, Y. Onel, C. Rössger,
U. Stegmaier, M. Steinbrück

Karlsruher Institut für Technologie

Karlsruher Institut für Technologie

in der Helmholtz-Gemeinschaft

Wissenschaftliche Berichte

NUSAFE 3572

Results of the QUENCH-DEBRIS (QUENCH-17) test with strongly oxidized Zircaloy-4 and hafnium claddings filled with segmented pellet simulators

J. Stuckert, M. Große, Y. Onel*, C. Rössger, U. Stegmaier, M. Steinbrück

Institut für Angewandte Materialien:
Angewandte Werkstoffphysik (IAM-AWP)

Programm Nukleare Entsorgung, Sicherheit und Strahlenforschung

*Bundesanstalt für Materialforschung und -prüfung

Karlsruher Institut für Technologie

2018

DOI: 10.5445/IR/1000088591

Impressum
Karlsruher Institut für Technologie (KIT)

Institut für Angewandte Materialien

Angewandte Werkstoffphysik IAM-AWP

Nukleare Sicherheitsforschung

Hermann-von-Helmholtz-Platz 1

76344 Eggenstein-Leopoldshafen

www.iam.kit.edu/awp/666.php

Abstract

In the framework of the SARNET-2 European program the QUENCH-DEBRIS test was conducted as the 17th severe accident test using the QUENCH facility at KIT to investigate the formation and coolability of a prototypic debris bed. The test scenario was defined by pre-test calculations using the MELCOR code. The test bundle with a length of about 2 m contains the hafnium shroud tube and 12 heated peripheral rods with claddings made of hafnium. Hafnium was chosen because of its much higher melting temperature and the about one order of magnitude lower oxidation rate compared to zirconium. The claddings of the inner nine rods were made of Zry-4. They were filled with pre-fragmented zirconia pellets. The test started with an oxidation phase of 20 h at peak cladding temperature about 1800 K to reach complete oxidation of the Zry-4 claddings over a height of 500 mm. The temperatures expected from the pre-test simulation fitted well the experimentally observed evolution of the bundle conditions.

The possibly surviving inner Zry-4 claddings were destroyed by the application of an axial mechanical force resulting in material relocation and formation of a heterogeneous debris bed consisting of segmented pellets and larger cladding tube fragments at the grid spacer #2 (350 mm bundle elevation) and in a smaller amount at grid spacer #3 (1050 mm elevation). The so destroyed bundle was quenched with 10 g/s water. The evaporation rate generally showed an increasing trend during the reflood, except at the time of water penetration through the debris bed at spacer #2 when stagnation was observed. During the oxidation phase about 100 g hydrogen was released.

The post-test examinations comprised videoscope inspections, high energy X-ray-tomography and metallographic investigations. Most of the Zry-4 claddings experienced relatively limited damage, and there was generally only minor damage of the geometrical integrity of the internal 9 rod sub-assembly. All peripheral hafnium claddings survived the whole test. The oxidation degree of Hf claddings inside the high temperature region of the bundle was noticeably lower compared with the oxidation of Zry claddings. The porosity of the debris bed was significant, no dense packing of debris particles was observed. Large empty volumes formed due to bending of rods.

Contents

List of Tables

List of Figures

Introduction

The main goal of the QUENCH program at KIT is to investigate the core thermal response, the cladding oxidation with accompanying hydrogen release and the cooling efficacy of water injection under design basis (DBA) and beyond design basis (BDBA) accident conditions. The program was initiated in 1996 and is still on-going. Eighteen high temperature bundle tests were performed (Table 1).

The experiment QUENCH-17 on debris formation was successfully conducted at KIT on 30…31 January 2013. It was performed in the framework of the European SARNET-2 program (WP 5.1). Debris bed coolability plays an important role in the termination and stabilization of a severe accident. Towards the quantitative understanding of debris bed coolability, many experiments have been conducted in the framework of the SARNET2 network to investigate two-phase flow and heat transfer in particle beds. These particle beds were prepared by uniform filling of cylindrical (facilities POMECO, DEBRIS, PRELUDE, PEARL; [1]) or conical (COOLOCE; [2]) columns with spherical, cylindrical or irregular (equivalent diameters from 2 to 12 mm) metallic or ceramic particles. Such kind of axial symmetrical pre-formed debris beds may be well described analytically. On the other hand such simplification is not very representative for the real geometry of a destroyed reactor core. Therefore, it was decided to use the electrically heated QUENCH facility with the prototypical rod geometry [3] to investigate the process of bundle destruction.

The QUENCH-17 test protocol was determined on the basis of planning calculations by PSI (MELCOR), GRS (ATHLET-CD), IRSN (ICARE/CATHARE), NRI (MELCOR), IBRAE (SOCRAT) and RUB (ATHLET-CD) and was aimed at achieving the test objectives agreed to in the following discussions between the SARNET partners [4]. The primary aims were to examine the formation of a debris bed inside the completely oxidized region of the bundle without melt formation, and to investigate the coolability phenomena during the reflood of the damaged bundle with fuel simulator debris particles without active volumetric heat sources. The course of the experiment showed clearly the objectives were met. The post-test analysis with the SOCRAT code showed that calculated results are in a good agreement with experimental data [5].

1 Test facility

The main component of the QUENCH test facility is the test section with the test bundle (Figs. 1…5). The facility can be operated in two modes: (a) a forced-convection mode and (b) a boil-off mode with the steam inlet line closed. QUENCH-17 was conducted in forced-convection mode, in which superheated steam from the steam generator and super-heater together with argon as a carrier gas for off-gas measurements enter the test bundle at the bottom. The system pressure in the test section is usually around 2 bar absolute.

Additionally to the gas inlet (steam and argon as carrier gas), the test section has separate inlets at the bottom to inject water for reflood (bottom quenching). The steam, argon and all other gases injected or produced flow from the bundle outlet at the top through a water-cooled off-gas pipe to the condenser where the steam is separated from the non-condensable gases. The water cooling circuits for bundle head and off-gas pipe are temperature-controlled to guarantee that the steam/gas temperature is high enough so that condensation at the test section outlet and inside the off-gas pipe is avoided and measurements of steam by mass spectrometer are allowed.

The design characteristics of the bundle are given in Table 2. The extensively instrumented test bundle with a length of about 2 m consisted of the shroud tube made of hafnium, twelve heated peripheral rods, all with hafnium cladding (Fig. 6), and nine unheated internal rods with Zry-4 claddings (Fig. 7). Additionally, four hafnium corner rods with integrated inner thermocouples were installed at the bundle periphery. Hafnium was chosen because of its by approx. 400 K higher melting temperature and the about one order of magnitude lower oxidation rate compared to zirconium, i.e. the heated rods, the shroud and the corner rods should survive the hard test conditions. The claddings of the inner nine rods were made of Zry-4. Four grid spacers made of Zry-4 were installed at elevations 0, 350, 1050 and 1350 mm. The heated rods were filled with Kr, the unheated rods with He; both with pressure of 2.3 bar. Tungsten heating elements of 6 mm diameter are installed in the center of the heated rods. The tungsten heaters (chemically clean tungsten) are connected to molybdenum heaters (chemically clean molybdenum) and copper electrodes (material 2.1293 with Cr 0.8, Zr 0.08 and rest Cu) at each end of the tungsten heater. The molybdenum and copper parts are joined by high-frequency/high-temperature brazing under vacuum (2x10-3 mbar) using an AuNi 18 powder (particle size <105 µm). The electrical resistance of the internal rod heating system, combined from W and Mo heaters and copper electrodes, was measured before (at the end of bundle assembling) and after the test (Table 4). For electrical insulation the surfaces of both types of electrodes are plasma-coated with 0.2 mm ZrO_2. To protect the copper electrodes and the O-ring-sealed wall penetrations against excessive heat they are water-cooled (lower and upper cooling chambers filled with demineralized water). The copper electrodes are connected to the DC electric power generator (only one in this QUENCH test) by means of special sliding contacts at the top and bottom.

The debris would be produced by collapse of the rods with oxidized Zircaloy claddings. According to experimental observations, large cracks, penetrating the oxide layer and the embrittled α-Zr(O) metal substrate, can be observed by quenching of claddings with a 200 µm oxide layer thickness (Fig. 15, [6]). It was decided to perform the full oxidation of the Zry-4 claddings over a height by more than 500 mm. The Zry-4 tubes of the nine

unheated rods were filled with pre-fragmented zirconia pellets (Fig. 16). The number of radial segments (eight) corresponds to pellets of PWR fuel rods with average linear rod power between 200 and 300 W/cm (PWR pellets cracked due to thermal expansion) [7]. The physical properties of the pellet material are described in Table 3. The gaps between segments were filled with zirconia powder to model the fine fraction of high burn-up fuel (Fig. 18). Previously, a single rod test on debris release was performed (Fig. 17).

The lower boundary of the lower cooling chamber is a sealing plate made of stainless steel with plastic inlays for electrical insulation, sealed toward the system by O-shaped rings. The upper boundary of the lower cooling chamber is a sealing plate of stainless steel. An insulation plate made of plastic (PEEK) forms the top of the upper cooling chamber; and a sealing plate of Al_2O_3, functioning as a heat-protection shield, is the lower boundary of the upper cooling chamber (Fig. 6).

In the region below the upper Al_2O_3 plate the copper electrode is connected firmly to the cladding. This is done by rotary swaging the cladding onto the electrode. In the swaging region a sleeve of boron nitride is put between electrode and cladding for electrical insulation. The axial position of the fuel rod simulator in the test bundle is fixed by a groove and a locking ring in the top Cu electrodes. Referred to the test bundle the fixing point of the fuel rod simulators is located directly above the upper edge of the upper insulation plate. So, during operation the fuel rod simulators are allowed to expand downwards. Clearance for expansion of the test rods is provided in the region of the lower sealing plate. Also in this region, relative movement between cladding and internal heater/electrode can take place.

The shroud is surrounded by a 34 mm thick ZrO_2 fiber insulation (physical properties are given in Table 5) and an annular cooling jacket made of Inconel 600 (inner tube) and stainless steel (outer tube) (Fig. 5). The annulus between shroud and cooling jacket was filled (after several cycles of degasing) with stagnant argon of 0.22 MPa and was connected to a flow-controlled argon feeding system in order to prevent steam access to the annulus after shroud failure. The 6.7 mm annulus of the cooling jacket is cooled by an argon flow. Above the heated zone, i.e. above the 1024 mm elevation there is no ZrO_2 fiber insulation to allow for higher radial heat losses. This region of the cooling jacket is cooled by a water flow (Figs. 3 and 4). Both the lack of ZrO_2 insulation above the heated region and the water cooling force the axial temperature maximum downward.

2 Instrumentation and data acquisition

The bundle is instrumented with 37 high-temperature (W/Re) thermocouples (TC) in the upper hot region (bundle and shroud thermocouples between elevations 650 and 1350 mm), 4 low-temperature (NiCr/Ni) thermocouples at elevations 1250 and 1350 mm (shroud), and 32 low-temperature (NiCr/Ni) thermocouples in the lower “cold” bundle region (bundle and shroud thermocouples between -250 and 550 mm) (Figs. 8, 9). The composition and fastening of thermocouples are presented in Figs. 10…12. The thermocouples are listed in Table 6 together with other measurement devices. The dimensions of high temperature thermocouples, which were manufactured by KIT, are provided in Table 7, some properties of the HfO_2 thermocouple insulator are given in Table 8. The thermocouples attached to the outer surface of the rod cladding at elevations

between -250 and 1350 mm are designated “TFS” for all heated rods (21 thermocouples). At elevations 950 and 650 mm there are two centreline high-temperature thermocouples in the central rod (designation “TCC”), which are protected from oxidizing influence of steam. Four other protected high temperature thermocouples are installed at elevations 550, 650, 750, and 850 mm inside the corner rods G, E, C and A and designated “TIT”. The shroud thermocouples (designation “TSH”) are mounted at the outer surface between 250 and 1250 mm. Due to oxidation of Zr cladding of thermocouples, many thermocouples not isolated from steam failed during the test (Table 9).

Additionally, the test section incorporates pressure gauges, flow meters, and a water level detector.

The off-gas including Ar, He, Kr, H_2, and H_2O is analysed by mass spectrometer Balzers “GAM300” whose sampling position is located at the off-gas pipe ≈2.66 m downstream the test section (Figs. 13, 14). The mass spectrometer allows indicating the failure of rod simulators by detection of He and Kr release.

Three unheated rods (#2, #4, and #8) were equipped in the low part with a center line Zr wire welded into holes punched through claddings at elevations 550 and 650 mm (Fig. 37). The on-line measurement of electrical resistivity of these connections allowed indicating the time point of complete oxidation at the corresponding elevations.

3 Test performance and results of online measurements

In common with the previous QUENCH experiments, the bundle was heated by a series of stepwise increases of electrical power from room temperature to a maximum of 900 K in an atmosphere of flowing argon (2 g/s) and superheated steam (2 g/s). The bundle was stabilised at this temperature, the electrical power being 4 kW. During this time the operation of the various systems was checked.

The detailed sequence of the test events is described in Table 10. To initiate the oxidation the bundle was first heated to 1750 K during 4000 s by power increase to 10 kW (Fig. 19). The power was further increased stepwise to about 12 kW after 10000 s to reach a maximum temperature of 1900 K. The readings of all thermocouples installed at the cladding surface (TFS) are presented in Fig. 20. Temperatures measured at each elevation between -250 and 1250 mm are shown in Figs. 21…36.

The power level of 12 kW was maintained constant during the most of the oxidation phase to reach the target extent of oxidation. During this phase the peak temperature decreased to 1800 K due to 1) diminishing chemical energy release, and 2) additional flow of relatively cold gas via leakage of unheated rods, whose first failure was detected at 5235 s, and shroud, which failed at 25245 s (Fig. 39). To increase the oxidation rate the power was increased to 14 kW at 67000 s and continued to the end of the oxidation phase at 77770 s. At this time the indicating devices showed that complete oxidation had been achieved at bundle elevation of 650 mm, as required by the test specification (Fig. 37). The hydrogen release was continuously monitored and showed the behavior expected according to the planning calculation with total release of about 100 g (Fig. 38).

No clear indication of debris relocation was observed during the pre-oxidation so far. This was as expected in the absence of any strong mechanical, thermal or hydrodynamic loading. In order to establish the debris bed prior to reflood, the largely intact inner Zry-4 claddings were destroyed by the application of an axial short pulse mechanical force resulting in material relocation and formation of a heterogeneous debris bed consisting of the pre-segmented pellets and larger cladding tube fragments at the two middle grid spacers. The debris bed formation at the top of the grid spacer #2 was confirmed by the response of fluid thermocouples installed at this location (Fig. 40).

Preparation for reflood was initiated at 77773 s by simultaneously turning off the steam flow, reducing the power to 4 kW, and switching the argon injection to the top of the bundle. Water was then injected with the flow rate of 10 g/s. The sequence led to a delay of 70 s between stopping the steam flow and starting the water injection. Power was then kept constant at 4 kW during the reflood.

A temperature increase of about 150 K was observed by fluid thermocouples during the delay period, indicating heat transfer from debris to the nearly stagnant steam and argon (Fig. 40). Following the start of injection a temporary reduction was observed lasting about 60 s. This may have been due to rapid steam generation for a short period at the start of refilling. A second temperature increase of up to 120 K then followed, lasting about 250 s while refilling of the lower volume continued, with the result that a maximum temperature of 1250 K inside the debris bed was observed at 78200 s. This coincided with the first indication of rod quenching at the bundle bottom (Fig. 41), after which the debris temperatures progressively reduced. At the same time the quench front advanced from the bottom of the bundle to the debris region, at which point the temperatures there dropped sharply to saturation indicating quench of the debris.

The quench progression correlated with a steady increase in the evaporation rate until the start of debris quenching, when the rate of increase remained approximately constant for about 150 s, before accelerating again (Fig. 42). This suggests a possible hindering of the quench process inside the debris itself. No significant hydrogen release was indicated during the quenching of debris bed. Simulation with cold water with the same flow rate (10 g/s) showed the front propagation time through the cold debris of about 27 s (Fig. 43).

Generally the quench progression indicated from thermocouples corresponded to the refilling as indicated by the measured collapsed water level. However, the water level stagnated at 78720 s when the elevation of 850 mm was reached, indicating the position of shroud breach. A sharp increase in hydrogen release at this time indicated water penetration through the breach and consequent strong reaction with the external metallic surface of the shroud.

4 Posttest investigations

The surface of the Hf corner rods withdrawn after the test showed a white oxide layer (HfO_2) between about 50 and 1100 mm (Fig. 44). The appearance of oxide layers below 1400 mm (below the upper grid spacer) is different for Zry (Fig. 45) and Hf (Fig. 46) claddings for all withdrawn upper parts of rods: whereas the oxide layer at the

surface of Hf claddings is white below and above this level, the oxide layer at the Zry surface is black below 1400 mm. The white surface of Hf claddings in this upper region was observed also by endoscope (Figs. 48, 49). The metallographic analysis showed that the oxidation of Zry claddings in this upper region was significantly stronger than the oxidation of Hf claddings. The tube segment of Zry-rod #7 was extracted from the third grid spacer and cut at elevation 1100 mm. Metallographic observation of the corresponding cross section showed complete oxidation of the cladding. The oxide thickness of the same rod at elevation 1430 mm was 30 µm, but the α-Zr(O) layer was very thick (270 µm). The Hf cladding of the heated rod #17 was cut at elevation 1050 mm for the determination of the hafnium oxidation. Metallographic measurements showed the formation of the hafnium oxide layer with a thickness of 110 µm; the residual cladding metal was completely converted to the α-Hf(O) phase. The surface of the middle part of the Hf shroud appeared also as white oxide layer (Fig. 51).

Both upper spacers at 1050 and 1350 mm were heavily oxidized but remained intact. The fourth spacer (at 1350 mm) was pulled out of the bundle without damaging of the spacer (Fig. 47). Large cladding fragments (as spalled oxide scales and tube segments) together with the pellet segments were collected between two upper grid spacers (Fig. 73).

Figs. 48 and 49 show that pellet segments from withdrawn (*after the test*) upper parts of the inner rods were collected at the upper surface of the spacer grid #3 (about 1100 mm). Inspections of the bundle top under this spacer (below 1050 mm) using an endoscope shows also the formation of a heterogeneous debris bed consisting of segmented pellets located in the sub-channels between the rods (Fig. 50). Completely oxidised Zry claddings exhibited some local shedding of spalled fragments; however the general morphology of the rods was mostly as large shards consistent with only minor damage prior to the imposed axial loading.

The bundle was filled with epoxy resin to perform tomography and metallographic examination. High energy X-ray tomography (maximal energy 12 MeV, axial scan step 295 µm) of the bundle (Fig. 52) was performed at the Bundesanstalt für Materialforschung und -prüfung (BAM) Berlin. Fig. 53 shows the achieved results for the longitudinal bundle section between elevations 300 and 900 mm, and the cross section (top view) at elevation 400 mm. The W heaters are red, the Hf components blue, zirconia parts orange and the empty space (epoxy) grey. The image analysis results in 85% blockage of the cooling channel at 400 mm. The elevations away from the grid spacer GS2 show either complete absence of the blockage under spacer (at 350 mm) or only slight blockage above the spacer (at 518 mm) (Fig. 54).

Results of metallographic investigations of bundle cross sections are presented in Figs. 55…71. It is important to note that metallographic analysis showed the formation of both external and *internal* oxide layers. The reason for the development of the inner oxide layer, which was observed also for QUENCH-06, QUENCH-12, QUENCH-14, and QUENCH-15 [8], should be the penetration of steam through circumferential and longitudinal cladding cracks going through the claddings. Another interesting finding is the lower oxidation of Hf claddings in comparison to Zry claddings. Table 11 and Table 13 show results of detailed measurements of thicknesses of ZrO_2 and α-Zr(O) layers at elevations 450, 550, 650 and 750 mm for each internal unheated rod (with Zry claddings). Similar data for HfO_2 and α-Hf(O) layers are collected in Table 12 and Table 14 for all outer heated rods (with Hf claddings). The averaged data on outer oxide thicknesses at each elevation (between 150 and 1350 mm) are collected in Table 15 for Zry and Hf claddings; Table 16 shows average internal oxide thicknesses at

elevations 150…1000 mm for Hf shroud and corner rods. The corresponding axial distributions of oxide layer thicknesses are presented in Fig. 72.

Both procedures (tomography and metallography) confirmed the formation of a debris bed between elevations 400 and 750 mm, which was indicated by the stagnation of evaporation rate in this region (Fig. 42). The debris particles are randomly distributed without formation of dense packing. Partial blockages (maximum 85% at 400 mm) by relocated pellet segments and oxide scales spalled from Zircaloy claddings as well as large empty volumes between bended rods were detected.

5 Summary and Conclusions

The QUENCH-17 bundle test with 9 unheated internal rods (Zry-4 claddings) and 12 heated external rods (Hf claddings) was performed in two stages: 1) long pre-oxidation stage (about 21.7 hours) at $T_{pct} \approx 1800$ K with complete oxidation of Zry-4 claddings between about 650 and 1150 mm; 2) reflood stage with slow flooding from bottom (10 g/s; or about 3 mm/s through the debris bed).

First failure of Zry-4 cladding was registered at about 5250 s. Hf claddings of heated rods were intact during the whole test; Hf shroud failed at about 800 mm after 25000 s. Oxidation degree of Hf claddings inside the high temperature region of the bundle was noticeably lower compared with the oxidation of Zry claddings.

Mechanical impact on the end of the pre-oxidation phase caused debris relocation to third and mainly to second grid spacers at elevations 1050 mm and 350 mm correspondingly.

The steam production rate stagnated during the propagation of flooding water through the debris collected above the second grid spacer. The videoscope, tomographic and metallographic observations confirmed the debris bed formation between about 400 and 750 mm.

Most of the Zry-4 claddings experienced relatively limited damage, and there was generally only minor damage of the geometrical integrity of the internal 9 rod sub-assembly. Ceramic debris collected at the top of spacers consist of separate pellet segments and relatively large oxidized cladding segments. The porosity of the debris bed is significant, no dense packing of debris particles was observed. Large empty volumes formed due to bending of rods. The maximum bundle blockage was about 85%. This blockage doesn't affect noticeably the bundle coolability.

6 Acknowledgments

The QUENCH-DEBRIS test was performed in framework of the European SARNET-2 program with financial support from the HGF Program NUSAFE. The authors thank all colleagues involved in the investigations, particularly J. Moch, J. Laier and U. Peters for bundle preparation, U. Peters also for metallographic analysis, B. Redmer from the BAM Berlin for his help to perform the high energy X-ray investigations. Furthermore the

very valuable support of the test planning by pre-test calculations performed at GRS, IBRAE, IRSN, NRI, PSI and RUB is strongly acknowledged.

7 References

1. G. Repetto, T. Garcin, M. Rashid, R. Kulenovic, Weimin Ma, Liangxing Li. „Investigation of Multidimensional Effects during Debris Cooling". 5th European Review Meeting on Severe Accident Research (ERMSAR-2012), Cologne, Germany (March 21-23, 2012).

2. E. Takasuo, S. Holmström, T. Kinnunen, P.H. Pankakoski, V. Hovi, M. Ilvonen, S. Rahman, M. Bürger, M. Buck, G. Pohlner. „Experimental and Computational Studies of the Coolability of Heap-like and Cylindrical Debris Beds". 5th European Review Meeting on Severe Accident Research (ERMSAR-2012), Cologne, Germany (March 21-23, 2012).

3. J. Stuckert, J. Birchley, M. Grosse, B. Jaeckel, M. Steinbrück. „Experimental and calculation results of the integral reflood test QUENCH-14 with M5 cladding tubes". Annals of Nuclear Energy, 37 (2010), 1036–1047, https://doi.org/10.1016/j.anucene.2010.04.015.

4. J. Stuckert. M. Große, Y. Onel, C. Rössger, M. Steinbrück. "Results of the QUENCH-DEBRIS Test". Proceedings of ICAPP 2014, Charlotte, USA, April 6-9, 2014, Paper 14150, https://publikationen.bibliothek.kit.edu/240095438/3816532

5. A. Vasiliev, J. Stuckert. " Post-test calculation of the QUENCH-17 bundle experiment with debris formation and bottom water reflood using thermal hydraulic and severe fuel damage code SOCRAT/V3". Nuclear Engineering and Design 283 (2015), 21–32, https://doi.org/10.1016/j.nucengdes.2014.03.011.

6. L. Steinbock, J. Stuckert. „Determination of the crack pattern of quenched Zircaloy tubes". Scientific Report FZKA-6013, Forschungszentrum Karlsruhe (1997). http://bibliothek.fzk.de/zb/berichte/FZKA6013.pdf .

7. M. Oguma. "Cracking and relocation behavior of nuclear fuel pellets during rise to power". Nuclear Engineering and Design, **76** (1983), 35-45, https://doi.org/10.1016/0029-5493(83)90045-6.

8. J. Stuckert, J. Birchley, M. Große, B. Jaeckel, M. Steinbrück. „Experimental and calculation results of the integral reflood test QUENCH-15 with ZIRLO™ cladding tubes in comparison with results of previous QUENCH tests". Nuclear Engineering and Design 241 (2011) 3224–3233, https://doi.org/10.1016/j.nucengdes.2011.05.004.

Tables and Figures

Table 1 QUENCH Test Matrix 1997 – 2013

Test	Quench medium and injection rate	Temp. at onset of flooding[1)]	Max. ZrO_2 before transient[2)]	Max. ZrO_2 (*X s*) before flooding[2)]	Posttest average ZrO_2 thickness[3)]	H_2 production before / during cooldown	Remarks, objectives
QUENCH-00 Oct. 9 - 16, 97	Water 80 g/s	≈ 1800 K			completely oxidized		Commissioning tests.
QUENCH-01 Febr 26, 98	Water 52 g/s	≈ 1830 K	312 µm		500 µm at 913 mm	36 / 3	COBE Project; partial fragmentation of pre-oxidized cladding.
QUENCH-02 July 7, 98	Water 47 g/s	≈ 2400 K			completely oxidized	20 / 140	COBE Project; no additional pre-oxidation; quenching from high temperatures.
QUENCH-03 January 20, 99	Water 40 g/s	≈ 2350 K			completely oxidized	18 / 120	No additional pre-oxidation, quenching from high temperatures.
QUENCH-04 June 30, 99	Steam 50 g/s	≈ 2160 K	82 µm		280 µm	10 / 2	Cool-down behavior of slightly pre-oxidized cladding by cold steam injection.
QUENCH-05 March 29, 2000	Steam 48 g/s	≈ 2020 K	160 µm		420 µm	25 / 2	Cool-down behavior of pre-oxidized cladding by cold steam injection.
QUENCH-06 Dec 13 2000	Water 42 g/s	≈ 2060 K	207 µm[5)]	300 µm, (60 s), SVECHA modeling	630 µm[4)]	32 / 4	OECD-ISP 45; prediction of H_2 source term by different code systems.
QUENCH-07 July 25, 2001	Steam 15 g/s	≈ 2100 K	230 µm		completely oxidized	66 / 120	COLOSS Project; impact of B_4C absorber rod failure on H_2, CO, CO_2, and CH_4 generation.
QUENCH-09 July 3, 2002	Steam 49 g/s	≈ 2100 K			completely oxidized	60 / 400	As QUENCH-07, steam-starved conditions prior to cooldown.

QUENCH-08 July 24, 2003	Steam 15 g/s	≈ 2090 K	274 µm		completely oxidized	46 / 38	As QUENCH-07, no absorber rod.
QUENCH-10 July 21, 2004	Water 50 g/s	≈ 2200 K	514 µm	613 µm (at 850 mm)	completely oxidized	48 / 5	LACOMERA Project; Air ingress.
QUENCH-11 Dec 08, 2005	Water 18 g/s	≈ 2040 K		170 µm	completely oxidized	9 / 132	LACOMERA Project; Boil-off.
QUENCH-12 Sept 27, 2006	Water 48 g/s	≈ 2100 K	160 µm, breakaway	300 µm, (110 s), breakaway	completely oxidized	34 / 24	ISTC Project #1648.2; VVER bundle with E110 claddings.
QUENCH-13 Nov 7, 2007	Water 52 g/s	≈ 1820 K		400 µm,after AgInCd rod failure	750 µm	42 / 1	SARNET; impact of AgInCd absorber rod failure on aerosol generation.
QUENCH-14 July 2, 2008	Water 41 g/s	≈ 2100 K	170 µm[6)]	470 µm[6)] (30 s)	900 µm	34 / 6	ACM series: M5® cladding
QUENCH-15 May 27, 2009	Water 48 g/s	≈ 2100 K	145 µm[6)]	380 µm[6)] (30 s)	620 µm	41 / 7	ACM series: ZIRLO™ cladding.
QUENCH-16 July 27, 2011	Water 53 g/s	≈ 1870 K*	135 µm	130 µm at 450-950 mm, breakaway	1075 µm at 550-650 mm	144 / 128	LACOMECO Project; Air ingress.
QUENCH-17 Jan. 31, 2013	Water 10 g/s	≈ 1800 K		completely oxidized	completely oxidized	110 / 1	SARNET-2; Debris formation and coolability.

[1)] Maximum measured bundle temperature at 950 mm elevation.
[2)] Measured (or calculated for LOCA tests) at the withdrawn corner rod at 950 mm elevation.
[3)] Measured posttest at the bundle elevation of maximum temperature, i.e. 950 mm.
[4)] Some claddings were completely oxidized at 950 mm elevation.
[5)] Oxide thickness during transient phase.
[6)] Zircaloy-4 corner rods.

Revised: Mai 2018

Table 2 Design characteristics of the QUENCH-17 test bundle

Bundle type		PWR
Bundle size		21 rods: 9 unheated rods (with Zry-4 claddings), 12 unheated rods (with Hf claddings)
Pitch		14.3 mm
Coolant channel area		30.1 cm^2
Hydraulic diameter		11.6 mm
Cladding material	inner / outer rods	Zry-4 / Hf
Cladding outside / inside diameter / thickness		10.75 / 9.3 / 0.725 mm
Cladding length (elevations)		2278 mm (-593 to 1685 mm)
Full length of rods(levels)	heated unheated	2480 mm (-690 to 1790 mm) 2140 mm (-250 to 1890 mm)
Material of middle heater	 surface roughness	Tungsten (W) Ra = 1.6 µm
Tungsten heater length (elevations)		1024 mm (0 to 1024 mm)
Tungsten heater diameter		6 mm
Pellets	material dimensions	ZrO_2;Y_2O_3-stabilized OD = 8.8 mm, L=10.5 mm (segmented in *24 segments* for unheated rods) OD = 9.15 mm, ID = 6.15 mm, L=11 mm (annular for heated rods);
Pellet stack	unheated rod heated rod	annular pellets: -250 to 500 mm segmented pellets: 500 to 1610 mm annular pellets: 0 to 1020 mm
Internal rod pressure at room temperature (gas)	unheated heated	0.23 MPa abs. (He) 0.23 MPa abs. (Kr)
Corner rod (8)	material instrumented (A, C) not instrumented (B, D)	Hf tube ∅ 6x0.9 (bottom: -1140 mm) rod ∅ 6 mm (top: +1300 mm) rod ∅ 6 mm (-1350 to +1155 mm)
Grid spacer	designation height location of lower edge	Zircaloy-4 42 mm 0, 350, 1050, 1410 mm
Shroud	material wall thickness outside diameter length (extension)	Hf (flange: Zry-4) 2.56 ± 0.24 mm (ultrasound at 1200 points) 83.3 mm 1600 mm (-300 to 1300 mm)
Shroud insulation	material insulation thickness elevation	ZrO_2 fiber 37 mm -300 mm to 1020 mm
Molybdenum heaters and Copper electrodes	length of upper part length of lower part diameter: - prior to coating - after coating with ZrO_2 coating surface roughness	766 mm (576 Mo, 190 mm Cu) 690 mm (300 Mo, 390 mm Cu) 7.6 mm 8.0 mm Ra = 6- 12 µm
Cooling jacket	Material: inner/outer tube inner tube outer tube	Inconel 600 (2.4816) / SS (1.4571) ID = 158.3 mm, OD = 168.3 mm ID = 181.7 mm, OD = 193.7 mm

Table 3 Main characteristics of the ZrO_2 pellet material, yttria-stabilized (type ZYK3)

Property	Data
Y_2O_3 content	5 %
Density	6.07 ± 0.03 g/cm^3
Open porosity	0
Average crystallite size	0.8 µm
Specific heat at 20 °C	400 J/kg K
Thermal conductivity at 100 °C	2.5 W/m K
Linear expansion, 20-1000 °C	11 x 10^{-6}/K
Vickers Hardness HV10	> 12000 N/mm^2
Bending strength	> 1150 MPa
Elastic modulus	> 200 GPa
Weibull modulus	20
Fracture toughness K_{1C}	12 MPa•m$^{1/2}$

According to Barat Ceramics GmbH, 07955 Auma

Table 4 QUENCH-17; electrical resistances of rods [mΩ] at 20 °C

Rod #	10	11	12	13	14	15	16	17	18	19	20	21	ave-rage	**10 rods parallel**
Pre-test	3.8	3.4	3.5	3.3	3.7	3.3	3.4	3.4	3.9	3.3	3.4	3.8	3.52	**0.29**
Post-test	not changed													

Note: Measured values include the resistance of slide contacts R_s=0.75 mΩ

All 12 rods were connected to one DC generator with 4 parallel bonded cables. The resistance of each cable is Rc=1.2 mΩ. Therefore, the external (outside) resistance corresponding to each heated rod (indicated by SCDAP/RELAP as fxwid) is Re=Rs+12*Rc/4=4.35 mΩ.

Table 5 Properties of zirconia fiber insulating boards of type ZYFB3

Chemical composition

Oxide	ZrO_2	Y_2O_3	HfO_2	TiO_2	SiO_2	CaO	MgO	Fe_2O_3	Al_2O_3	Na_2O
typical wt%	88	10	2	0.14	0.12	0.09	0.03	0.04	0.01	0.01

Physical properties

bulk density	porosity	shrinkage		thermal expansion coefficient @298-1453K	melting point	max service temperature	flexural strength	compressive strength @10% compression
		(1 hour @1925 K)	(24 hours @1925 K)					
g/cm³	%	%		1/K	K	K	MPa	MPa
0.48	92	1.2	2.8	$10.7*10^{-6}$	2866	2500	0.59	0.29

Thermal conductivity

temperature, K	673	1073	1373	1673	1923
conductivity, W/(m*K)	0.08	0.11	0.14	0.19	0.24

Specific heat capacity

temperature, K	366	2644
specific heat capacity, J/(kg*K)	544	754

According to specifications of manufacturer ZIRCAR PRODUCTS

Table 6 List of instrumentation for the QUENCH-17 Test

Chan-nel	Designation	Instrument, location	Output in
0		Reserve (W/Re)	K
1	**TFS 13/13**	**TC (W/Re) fuel rod simulator 13 (type 5), 950 mm, 45°**	**K**
2		Reserve (W/Re)	K
3		Reserve (W/Re)	K
4	**TFS 17/17**	**TC (W/Re) fuel rod simulator 17 (type 5), 1350 mm, 135°**	**K**
5		Reserve (W/Re)	K
6		Reserve (W/Re)	K
7	**TFS 16/16**	**TC (W/Re) fuel rod simulator 16 (type 5), 1250 mm, 135°**	**K**
8		Reserve (W/Re)	K
9		Reserve (W/Re)	K
10	**TFS 14/14**	**TC (W/Re) fuel rod simulator 14 (type 4), 1050 mm, 45°**	
11..12		Reserve (W/Re)	
13	**TSH 13/90 I**	**TC (W/Re) shroud outer surface, 950 mm, 116°, behind shroud insulation**	**K**
14		Reserve (W/Re)	
15	**TFS 15/15**	**TC (W/Re) fuel rod simulator 15 (type 5), 1150 mm, 315°**	**K**
16..21		Reserve (W/Re)	K
22	**TGS 9o**	**TC (NiCr/Ni) grid spacer 400 mm, rod 9 outside unheated rods circle**	**K**
23		Reserve (NiCr/Ni)	K
24..31		Reserve (20 mA)	
26..31		Reserve (W/Re)	
32	**TIT A/13**	**TC (W/Re) corner rod A, center, 950 mm**	**K**
33		Reserve (W/Re)	K
34	**TFS 10/10**	**TC (W/Re) fuel rod simulator 10 (type 5), 650 mm, 315°**	**K**
35	**TSH 9/0**	**TC (NiCr/Ni) shroud outer surface, 550 mm, 116°**	**K**
36	**TSH 9/180**	**TC (NiCr/Ni) shroud outer surface, 550 mm, 296°**	**K**
37		Reserve (W/Re), channel defect?	
38	**TFS 18/9**	**TC (NiCr/Ni) fuel rod simulator 18 (type 2), 550 mm, 225°**	**K**
39	**TFS 17/8**	**TC (NiCr/Ni) fuel rod simulator 17, 450 mm, 135°**	**K**
40	**TIT C/11**	**TC (W/Re) corner rod C, center, 750 mm**	**K**

Chan-nel	Designation	Instrument, location	Output in
41	**TIT D/12**	**TC (W/Re) corner rod A, center, 650 mm**	**K**
42	**TFS 16/7**	**TC (NiCr/Ni) fuel rod simulator 16, 350 mm, 225°**	**K**
43	**TFS 13/4**	**TC (NiCr/Ni) fuel rod simulator 13, 50 mm, 315°**	**K**
44	**TFS 12/3**	**TC (NiCr/Ni) fuel rod simulator 12, -50 mm**	**K**
45	T 304	TC (NiCr/Ni) outer surface of pipe after V302	K
46	**TFS 14/5**	**TC (NiCr/Ni) fuel rod simulator 14, 150 mm, 45°**	**K**
47	**TSH 16/180**	**TC (W/Re) shroud outer surface, 1250 mm, 206°, behind shroud insulation**	**K**
48	**TSH 15/180**	**TC (W/Re) shroud outer surface, 1150 mm, 206°, behind shroud insulation**	**K**
49	**TSH 14/90 I**	**TC (W/Re) shroud outer surface, 1050 mm, 116°, behind shroud insulation**	**K**
50	**TIT B/12**	**TC (W/Re) corner rod A, center, 850 mm**	**K**
51	**TFS 11/11**	**TC (W/Re) fuel rod simulator 11 (type 4), 750 mm, 315°**	**K**
52	**TSH 13/270 I**	**TC (W/Re) shroud outer surface, 950 mm, 296°, behind shroud insulation**	**K**
53	**TSH 14/270 I**	**TC (W/Re) shroud outer surface, 1050 mm, 270°, behind shroud insulation**	**K**
54	**TSH 11/180 I**	**TC (W/Re) shroud outer surface, 750 mm, 206°, behind shroud insulation**	**K**
55	**TSH 12/180 I**	**TC (W/Re) shroud outer surface, 850 mm, 206°, behind shroud insulation**	**K**
56	**TSH 12/0 I**	**TC (W/Re) shroud outer surface, 850 mm, 26°, behind shroud insulation**	K
57	**TSH 11/0 I**	**TC (W/Re) shroud outer surface, 750 mm, 26°, behind shroud insulation**	**K**
58	**TGS 7o**	**TC (NiCr/Ni) grid spacer 400 mm, rod 7 outside unheated rods circle**	**K**
59	**TSH 10/90 I**	**TC (W/Re) shroud outer surface, 650 mm, 116°, behind shroud insulation**	
60	**TFS 12/12**	**TC (W/Re) fuel rod simulator 12 (type 5), 850 mm, 225°**	**K**
61		Reserve NiCr/Ni	K
62..63		Reserve (20 mA)	g/s
64	T 402b	Temperature of the tube surface after gas heater	K
65	**TSH 10/270 I**	**TC (W/Re) shroud outer surface, 650 mm, 296°, behind shroud insulation**	**K**

Chan-nel	Designation	Instrument, location	Output in
66	**TSH 15/0 I**	**TC (W/Re) shroud outer surface, 1150 mm, 26°, behind shroud insulation**	**K**
67	**TSH 16/0 I**	**TC (W/Re) shroud outer surface, 1250 mm, 26°, behind shroud insulation**	**K**
68	T 512	Gas temperature bundle outlet	K
69		Reserve (W/Re)	
70		Reserve (W/Re)	K
71	Ref. T 01	Reference temperature 1: contacts of crate #1	K
72	**TFS 10/1**	**TC (NiCr/Ni) fuel rod simulator 10, -250 mm**	**K**
73	**TFS 11/2**	**TC (NiCr/Ni) fuel rod simulator 11, -150 mm**	**K**
74	**TSH 2/90**		**K**
75	**TSH 3/180**		**K**
76	**TSH 5/0**		**K**
77	**TGS 5i**	**TC (NiCr/Ni) grid spacer 350 mm, rod 5 inside unheated rods circle**	**K**
78	**TSH 5/180**		**K**
79	**TSH 6/90**		**K**
80	**TSH 6/270**		**K**
81	**TFS 15/6**	**TC (NiCr/Ni) fuel rod simulator 15 (type 5), 250 mm, 315°**	**K**
82	**TGS 7i**	**TC (NiCr/Ni) grid spacer 400 mm, rod 7 inside unheated rods circle**	**K**
83	**TSH 4/270**	**TC (NiCr/Ni) shroud outer surface, 50 mm, 296°**	**K**
84	T 511	Gas temperature at bundle inlet	**K**
85	**TSH 8/90**	**TC (NiCr/Ni) shroud outer surface, 50 mm. 206°**	**K**
86	**TSH 7/180**	**TC (NiCr/Ni) shroud outer surface, 350 mm, 206°**	**K**
87	**TSH 4/90**	**TC (NiCr/Ni) shroud outer surface, 50 mm, 116°**	**K**
88	**TSH 1/0**	**TC (NiCr/Ni) shroud outer surface, -250 mm, 26°**	**K**
89	**TSH 8/270**	**TC (NiCr/Ni) shroud outer surface, 50 mm, 26°**	**K**
90	**TSH 7/0**	**TC (NiCr/Ni) shroud outer surface, 350 mm, 26°**	**K**
91	TCI 9/270	TC (NiCr/Ni) cooling jacket inner tube wall, 550 mm, 270°	K
92	TCI 10/270	TC (NiCr/Ni) cooling jacket inner tube wall, 650 mm, 270°	K
93	TCI 11/270	TC (NiCr/Ni) cooling jacket inner tube wall, 750 mm, 270°	K
94	TCI 13/270	TC (NiCr/Ni) cooling jacket inner tube wall, 950 mm, 270°	K
95	**TGS 5o**	**TC (NiCr/Ni) grid spacer 400 mm, rod 5 outside unheated rods**	**K**

Chan-nel	Designation	Instrument, location	Output in
96	TCI 1/180	TC (NiCr/Ni) cooling jacket inner tube wall, -250 mm, 180°	K
97	TCI 4/180	TC (NiCr/Ni) cooling jacket inner tube wall, 50 mm, 180°	K
98	TCI 7/180	TC (NiCr/Ni) cooling jacket inner tube wall, 350 mm, 180°	K
99	TCI 11/180	TC (NiCr/Ni) cooling jacket inner tube wall, 750 mm, 180°	K
100	TCI 12/180	TC (NiCr/Ni) cooling jacket inner tube wall, 850 mm, 180°	K
101	TCI 13/180	TC (NiCr/Ni) cooling jacket inner tube wall, 950 mm, 180°	K
102	TCI 15/180	TC (NiCr/Ni) cooling jacket inner tube wall, 1150 mm, 180°	K
103	T002 inlet	Cooling water, inlet of off-gas tube	K
104		TCI 9/90 defect	K
105		TCI 10/90 defect	K
106	TCI 11/90	TC (NiCr/Ni) cooling jacket inner tube wall, 750 mm, 90°	K
107	TCI 13/90	TC (NiCr/Ni) cooling jacket inner tube wall, 950 mm, 90°	K
108	**TGS 3o**	**TC (NiCr/Ni) grid spacer 400 mm, rod 3 outside unheated rods circle**	K
109	TCI 1/0	TC (NiCr/Ni) cooling jacket inner tube wall, -250 mm, 0°	K
110	TCI 4/0	TC (NiCr/Ni) cooling jacket inner tube wall, 50 mm, 0°	K
111	TCI 7/0	TC (NiCr/Ni) cooling jacket inner tube wall, 350 mm, 0°	K
112	TCI 11/0	TC (NiCr/Ni) cooling jacket inner tube wall, 750 mm, 0°	K
113	TCI 12/0	TC (NiCr/Ni) cooling jacket inner tube wall, 850 mm, 0°	K
114	TCI 13/0	TC (NiCr/Ni) cooling jacket inner tube wall, 950 mm, 0°	K
115	TCI 15/0	TC (NiCr/Ni) cooling jacket inner tube wall, 1150 mm, 0°	K
116	T003	Cooling water, outlet of off-gas tube	K
117	TCO 9/270	Reserve (TC defect)	K
118	TCO 4/180	Reserve (TC defect)	K
119	**TGS 3i**	**TC (NiCr/Ni) grid spacer 400 mm, rod 3 inside unheated rod circle**	K
120	TCO 1/0	TC (NiCr/Ni) cooling jacket outer tube surface, -250 mm, 0°	K
121	TCO 7/0	TC (NiCr/Ni) cooling jacket outer tube surface, 350 mm, 0°	K
122	TCO 13/0	TC (NiCr/Ni) cooling jacket outer tube surface, 950 mm, 0°	K
123	T 601	Temperature before off-gas flow instrument (orifice) F 601	K
124	T 513	Outer wall of bundle head	K
125	*T 514*	Cooling water bundle head	
126	T307 off-gas	*TC (NiCr/Ni) inner surface of inlet of off-gas pipe*	K

Chan-nel	Designation	Instrument, location	Output in
127	***TGS 9i***	**TC (NiCr/Ni) grid spacer 400 mm, rod 9 inside unheated rods circle**	**K**
128	T 104	Temperature quench water	K
129	T 201	Temperature steam generator heating pipe	K
130	T 204	Reserve (steam 50 g/s)	K
131	T 205	Temperature before steam flow instrument location 10 g/s	K
132	T 301A	Temperature behind superheater	K
133	T 302	Temperature superheater heating pipe	K
134	T 303	Temperature before total flow instrument (orifice) location	K
135	T 401	Reserve (inlet Ar orifice)	K
136	T 403	Temperature of Ar at cooling jacket inlet	K
137	T 404	Temperature of Ar at outlet cooling jacket	K
138	T 501 cont-t	Temperature in containment (near from bundle head)	K
139	T 502	Temperature at outer surface of containment, 0°, 2.4 m	K
140	T 503	Temperature at outer surface of containment, 270°, 2.2 m	K
141	T 504	Temperature at outer surface of containment, 270°, 3.2 m	K
142	T 505	Temperature at outer surface of containment, 90°, 3.2 m	K
143	T 506	Temperature at outer surface of containment, 270°, 3.6 m	K
144	T 507	Temperature at outer surface of containment, 90°, 3.6 m	K
145	T 508	Temperature at outer surface of containment, 180°, 4.0 m	K
146	T 509	TC (NiCr/Ni) aerosol extraction tube in off-gas pipe	K
147	T 510	Temperature at outer surface of containment, 270°, 4.4 m	K
148		Reserve (NiCr/Ni)	K
149	T 901	Reserve (temperature before F 901)	K
150		Reserve (NiCr/Ni)	**K**
151	Ref. T 02	Reference temperature 2	K
152	P 201	Pressure steam generator	bar
153	P 204	Reserve (pressure steam 50 g/s)	bar
154	P 205	Pressure at steam flow instrument location 10 g/s	bar
155	P 303	Pressure before total flow instrument (orifice) location	bar
156	P 401	Pressure before gas flow instrument location	bar
157	P 511	Pressure at bundle inlet	bar
158	P 512	Pressure at bundle outlet	bar

Chan-nel	Designation	Instrument, location	Output in
159	P 601	Pressure before orifice of off-gas pipe	bar
160	P 901	Pressure after condenser (end of off-gas system)	bar
161	L 201	Liquid level steam generator	mm
162	L 501	Liquid level quench water	mm
163	L 701	Liquid level of condensation vessel	mm
164	**Fm 401**	Argon flow rate (Bronkhorst device)	g/s
165	P 411	Pressure **Kr** supply (heated rod filling)	bar
166	P 403	Pressure Ar cooling of cooling jacket	bar
167	P 406	Pressure insulation shroud/cooling jacket	bar
168	**Fm 104**	Flow rate quench water	l/h
169	F 204	Reserve (steam 50 g/s)	g/s
170	**Fm 205**	Flow rate steam 10 g/s	g/s
171	F 303	Flow rate at bundle inlet (steam + argon), orifice	mbar
172	F 401	Flow rate	Nm^3/h
173	Fm 403	Flow rate cooling gas	g/s
174	F 601	Flow rate off-gas (orifice)	mbar
175	**Fm 406**	Flow rate argon into room between shroud and cooling jacket	g/s
176	E 201	Electric current steam generator	A
177	E 301	Electric current superheater	A
178	E 501	Electric current inner ring of fuel rod simulators	A
179	E 502	Reserve (electric current outer ring of fuel rod simulators)	A
180	E 503	Electric voltage inner ring of fuel rod simulators	V
181	E 504	Reserve (electric voltage outer ring of fuel rod simulators)	V
182	Hub_V302	Gas supply valve lift	%
183	Ref. T 03	Reference temperature 3	K
:			
250	E 505	Electric power inner ring of fuel rod simulators	W
251	E 506	Reserve (electric power outer ring of fuel rod simulators)	W

Table 7 Diameters of the materials used for the high temperature thermocouples [mm]

Material	As-received	Final
W/Re wires	0.254	
HfO_2 insulation OD (see drawing below)	1.1	
Ta tube OD / ID	2.15 / 1.65	1.4 / 0.94
Zr tube OD / ID	2.5 / 1.65 ± 0.05	2.2-2.3 / ~1.4

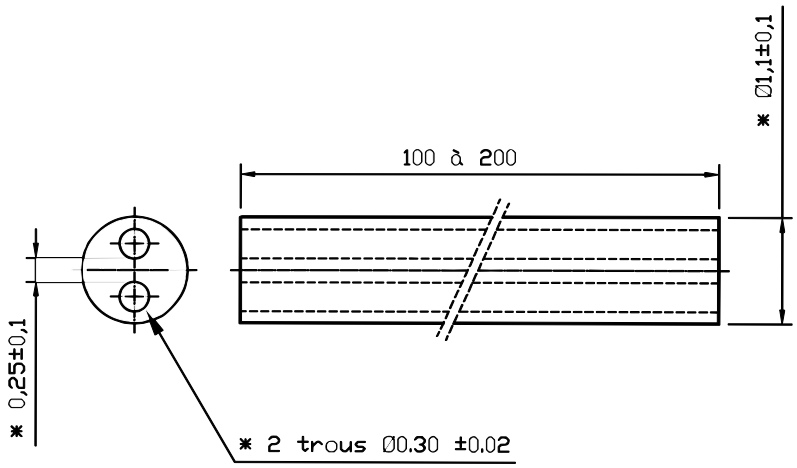

Table 8 Main characteristics of the HfO_2 thermocouple insulator

Property	Data
Composition of basic material	99% HfO_2
Melting temperature	2840 °C
Max. use temperature	2500 °C
Density	8.4 g/cm^3
Thermal conductivity at 20-1000 °C	1.14 W/m K
Linear expansion	5.8 x 10^{-6}/K

According to Saint-Gobain ceramics, 1997

Table 9 QUENCH-17; failures of thermocouples

Thermocouple	Elevation [mm]	Time at failure [s]	Failure temperature [K]
TFS 13/13	950	4349	1607
TFS 12/12	850	4919	1744
TFS 14/14	1050	6960	1438
TFS 11/11	750	10800	1708
TFS 15/15	1150	12494	1221
TFS 16/16	1250	12509	1168
TFS 10/10	650	16830	1674
TSH 13/270	950	27200	1590
TFS 17/17	1350	54602	1045
TFS 18/9	550	77540	1772
TSH 15/0	1150	75746	979
TFS 17/8	450	77898	1765
TSH 10/90	650	78572	865
TSH 10/270	650	78597	860
TSH 14/270	1050	78622	929
TSH 11/0	750	78660	862
TSH 11/180	750	78675	845
TSH 12/0	850	78734	873
TSH 12/180	850	78739	852
TSH 15/180	1150	78751	920
TSH 16/0	1250	78842	861
TSH 14/90	1050	79615	384
TSH 16/180	1250	79697	729

Table 10 QUENCH-17; sequence of events

Time, s	Event
30.01.2013 0 (15:29:52 h)	Start of data recording
5000	TIT A/13 = 1777 K, Pel = 10 kW,
5235	First Zry rod failure (indication of He by MS)
13246	Start of plateau of el. power Pel -= 12.2 kW, TIT A/13 = 1910 K
25245	Shroud failure; additional Ar flow through the damaged shroud
29600	Beginning of constant Ar flow through the shroud crack, 0.3 g/s
33400	R2= ∞ Ohm
56700	R1= ∞ Ohm
66967 - 67242	El. power increase to 14 kW
68785 - 69629	Interim decrease of electrical power during check of the Ar flow
68790 - 68820	Interim interrupt of Ar supply 2 g/s (exchange of gas flasks)
71600	R3 = ∞ Ohm (indication of complete oxidation at 650 mm)
77490	Debris at top of GS#2 (TGS reaction), increase of hydrogen release
77770	El. power decrease from 14 kW to 4 kW
77773	Valve between gas super-heater and bundle inlet closed (decrease of Fm205 reading), Ar switched to bundle top
77773 - 77850	Temporary increase of temperatures inside the bundle (mostly TGS) due to absence of gas flow (no steam, Ar to top)
77930 - 78200	Increase of temperature above GS#2
77790	***Quench pump initiation***
77840	L 501: beginning of water level increase
78006	T 511: water at -350 mm
78186	TFS 10/1: water at -250 mm
78190 - 78480	Mass spectrometer: linear increase of steam release rate
78220 - 78510	L 701: linear increase of steam release rate
78420	Reaction of TGS thermocouples: water at elevation 400 mm (i.e. above GS #2)
78480 - 78625	Mass spectrometer: constant steam release rate
78510 - 78655	L 701 (collection of condensed steam): constant steam release rate (delay 30 s in comparison to mass spectrometer due to long distance)
81084	End of data recording

Table 11 Thickness of outer and inner oxide layers at four circumferential positions of Zry-4 claddings (in µm)

Elevation [mm]		450		550		650		750	
rod	angle	out	in	out	in	out	in	out	in
Rod 1	0°	21	11	223	70	270	543	636	763
	90°	27	15	164	59	458	433	585	550
	180°	19	9	269	72	408	529	553	474
	270°	31	9	291	82	290	563	664	476
Rod 2	0°	20	49	497	67	1153	-	485	530
	90°	26	44	287	53	1018	-	601	423
	180°	40	10	317	43	462	531	460	512
	270°	21	0	371	41	469	572	412	451
Rod 3	0°	33	32	795	282	463	566	352	661
	90°	29	31	367	217	508	535	430	685
	180°	31	28	-	-	401	614	662	531
	270°	37	36	707	322	488	764	426	723
Rod 4	0°	27	8	555	160	-	-	422	608
	90°	26	6	353	147	-	-	456	571
	180°	33	0	261	104	-	-	372	675
	270°	31	0	287	144	-	-	383	773
Rod 5	0°	257	12	278	52	544	544	545	665
	90°	24	124	263	52	539	454	588	486
	180°	29	8	216	42	534	561	531	514
	270°	28	12	259	40	480	382	514	439
Rod 6	0°	22	9	296	79	557	295	346	697
	90°	21	5	432	79	430	289	377	650
	180°	27	0	339	71	824	231	372	710
	270°	26	0	302	72	459	331	386	669
Rod 7	0°	37	0	592	428	597	430	691	859
	90°	35	29	548	433	783	239	521	805
	180°	58	0	676	308	874	159	585	609
	270°	57	13	607	292	741	274	725	416
Rod 8	0°	82	30	-	-	712	217	480	452
	90°	75	28	711	342	558	202	465	573
	180°	65	24	657	373	644	214	482	644
	270°	70	26	732	297	735	307	613	709
Rod 9	0°	24	22	504	358	-	-	597	617
	90°	25	16	406	437	-	-	608	601
	180°	30	5	598	341	-	-	592	626
	270°	30	16	563	395	-	-	313	572

Table 12 Thickness of outer and inner oxide layers at four circumferential positions of Hf claddings (in μm)

Elevation, mm		450		550		650		750	
rod	angle	out	in	out	in	out	in	out	in
Rod 10	0°	127	0	125	0	133	0	188	-
	90°	136	11	117	0	160	0	193	-
	180°	130	0	133	0	155	0	189	-
	270°	119	18	156	0	164	0	227	-
Rod 11	0°	145	0	133	0	167	0	232	-
	90°	142	0	151	0	173	0	193	-
	180°	136	0	156	0	149	0	224	-
	270°	153	0	147	0	172	0	207	-
Rod 12	0°	159	14	-	-	141	0	208	-
	90°	109	13	152	0	146	0	217	-
	180°	141	12	128	0	161	0	196	-
	270°	131	0	162	0	175	0	216	-
Rod 13	0°	142	10	135	0	178	0	218	0
	90°	135	77	138	0	462	0	188	0
	180°	135	0	137	0	-	-	222	0
	270°	105	0	149	0	-	-	200	0
Rod 14	0°	150	0	140	0	177	0	194	0
	90°	133	76	128	0	140	0	196	0
	180°	124	0	143	0	277	0	232	0
	270°	99	0	133	0	-	-	208	0
Rod 15	0°	102	0	134	0	135	0	231	0
	90°	123	0	151	0	177	0	230	0
	180°	159	0	125	0	157	0	229	0
	270°	180	0	117	0	157	0	255	0
Rod 16	0°	133	8	123	0	178	0	265	0
	90°	175	0	137	0	173	0	234	17
	180°	157	0	153	0	183	0	286	0
	270°	120	7	149	0	156	0	268	0
Rod 17	0°	127	0	144	0	165	20	262	0
	90°	142	23	146	0	211	0	280	0
	180°	166	0	165	0	208	17	246	0
	270°	186	0	143	0	174	0	231	0
Rod 18	0°	134	0	128	0	143	0	212	0
	90°	118	0	126	0	189	0	208	0
	180°	138	0	125	0	147	0	219	0
	270°	139	0	133	0	177	0	210	0
Rod 19	0°	192	12	127	0	185	0	242	0
	90°	192	17	150	0	208	0	190	0
	180°	150	14	166	0	189	0	240	0
	270°	150	0	133	0	201	0	229	0
Rod 20	0°	157	9	154	0	214	0	247	0
	90°	142	0	157	0	219	0	263	0
	180°	138	0	146	0	213	0	254	0
	270°	115	12	140	0	199	0	259	0
Rod 21	0°	127	0	110	0	140	0	259	0
	90°	141	15	153	0	180	0	216	0
	180°	154	10	125	0	-	-	248	0
	270°	140	9	135	0	178	0	238	0

Table 13 Thickness of inner and outer α-Zr(O) layer at four circumferential positions of Zry-4 claddings (in μm)

Elevation, mm		450		550		650		750	
rod	angle	α-out	α-in	α-out	□□in	α-out	α-in	α-out	α-in
Rod 1	0°	89		462					
	90°	70	16	501					
	180°	95	11	436					
	270°	106	9	410					
Rod 2	0°	125	72	357					
	90°	107	0	604					
	180°	150	80	206	260				
	270°	183	198	580					
Rod 3	0°	317	41	0					
	90°	241	31	256					
	180°	289	29	-	-				
	270°	345	43	0					
Rod 4	0°	181	0	270					
	90°	77	0	392					
	180°	119	0	458					
	270°	119	0	425					
Rod 5	0°	219	18	521					
	90°	195	14	543					
	180°	141	12	312	62				
	270°	192	13	543					
Rod 6	0°	208	0	474					
	90°	218	0	358					
	180°	185	0	439					
	270°	178	0	477					
Rod 7	0°	112	44	0	0				
	90°	101	0	0	0				
	180°	172	0	0	0				
	270°	122	0	0	0				
Rod 8	0°	83	83	-	-				
	90°	84	79	0	0				
	180°	121	100	0	0				
	270°	101	90	0	0				
Rod 9	0°	228	0	0	0				
	90°	200	25	0	0				
	180°	326	0	0	0				
	270°	336	0	0	0				

Table 14 Thickness of inner and outer α-Hf(O) layer at four circumferential positions of Hf claddings (in μm)

Elevation, mm		450		550		650		750	
rod	angle	α-out	α-in	α-out	α-in	α-out	α-in	α-out	α-in
Rod 10	0°	385	0	704		704		650	
	90°	298	0	727		659		643	
	180°	271	0	707		659		631	
	270°	418	0	697		682	0	676	
Rod 11	0°	459	40	717		378	0	643	
	90°	388	0	738		678	0	667	
	180°	439	0	691		670	0	643	
	270°	418	0	757		650	0	645	
Rod 12	0°	471	0	-	-	684	0	658	
	90°	404	0	694		667	0	630	
	180°	133	0	672		671	0	645	
	270°	314	0	690		650	0	660	
Rod 13	0°	411	0	669		671	0	637	
	90°	378	0	638		692	0	647	
	180°	365	0	698		-	-	636	
	270°	455	0	649		-	-	645	
Rod 14	0°	418	0	722		693	0	635	
	90°	316	0	705		660	0	627	
	180°	272	0	720		671	-	647	
	270°	374	0	735		-	-	659	
Rod 15	0°	329	35	649		698	0	606	
	90°	279	0	688		659	0	489	
	180°	353	0	655		700	0	638	
	270°	307	0	757		679	0	612	
Rod 16	0°	233	109	660		689	0	638	
	90°	227	65	632		651	0	618	
	180°	246	0	698		656	0	615	
	270°	219	0	649		683	0	650	
Rod 17	0°	218	0	743		674	0	614	
	90°	219	33	642		630	0	601	
	180°	244	0	725		664	0	643	
	270°	209	0	731		696	0	631	
Rod 18	0°	163	0	706		664	0	652	
	90°	173	31	481		664	0	641	
	180°	184	0	721		673	0	664	
	270°	188	0	711		696	0	626	
Rod 19	0°	204	82	753		686	0	670	
	90°	237	63	682		537	0	630	
	180°	266	0	690		680	0	653	
	270°	254	0	713		697	0	552	
Rod 20	0°	283	0	691		633	0	607	
	90°	284	48	623		646	0	625	
	180°	366	0	683		643	0	643	
	270°	152	0	669		661	0	642	
Rod 21	0°	308	78	680		684	0	666	
	90°	308	36	685		668	0	622	
	180°	302	0	532		-	-	628	
	270°	363	22	675		696	0	649	

Table 15 QUENCH-17: thicknesses of oxide layer at outer surface of claddings (if not completely oxidized), average values for each elevation

Elevation, mm	**ZrO_2, µm**	HfO_2-clad, µm
150	**10**	200
390	**40**	140
450	**40**	125
550	**700**	140
650	**1100**	200
750	**1100**	180
850	**1100**	750
950	**1100**	1100
1050	**1100**	140
1330	**300**	0

Table 16 QUENCH-17: thicknesses of oxide layer at inner surface of shroud and outer surface of corner rods, average values for each elevation

Elevation, mm	HfO_2-shroud,µm	HfO_2-corner, µm
150	0	0
390	70	115
450	100	140
550	110	150
650	190	180
750	90	160
850	950	270
950	1200	1550
1100	80	70

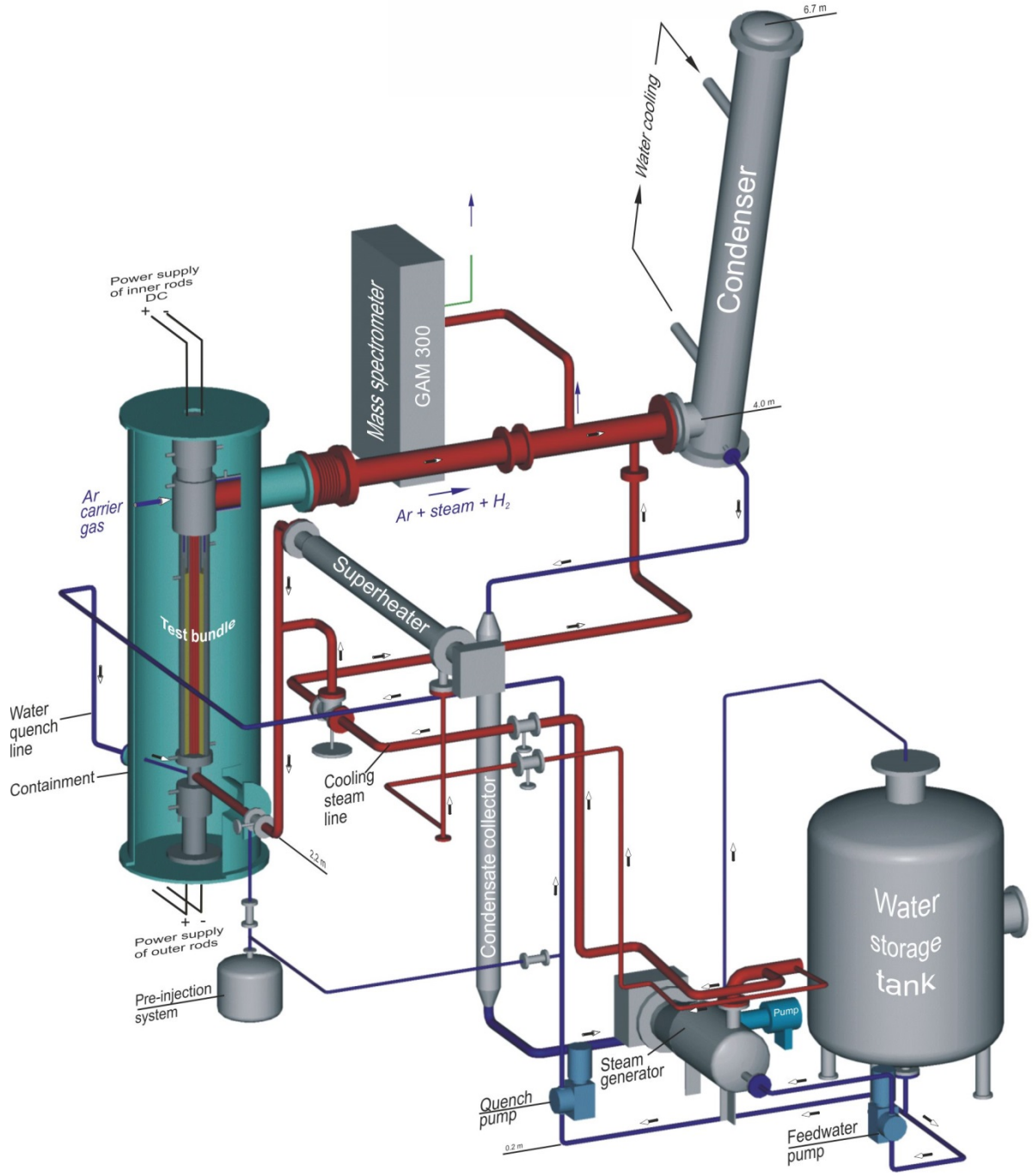

Figure 1 QUENCH Facility - Main components

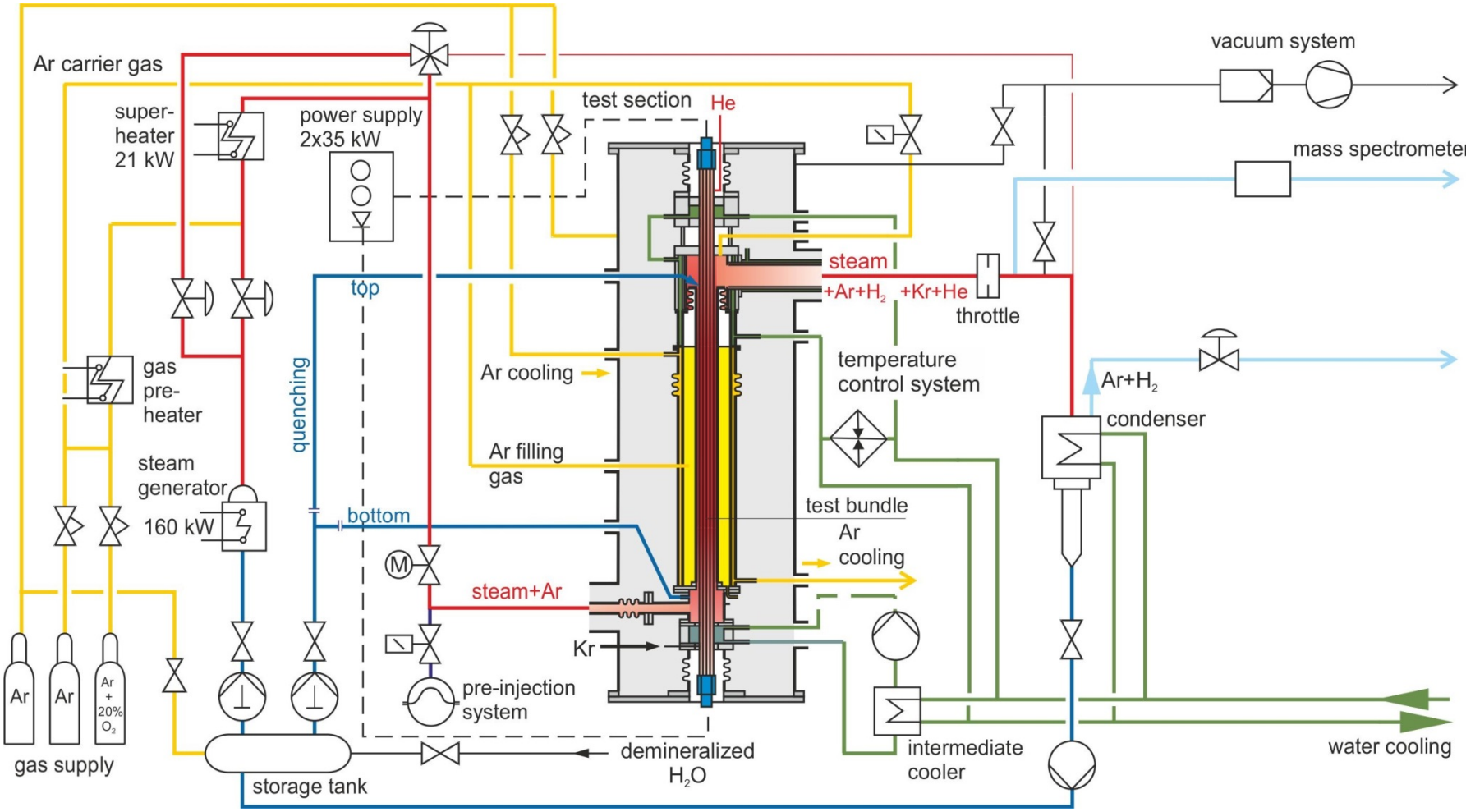

Figure 2 Flow diagram of the QUENCH test facility.

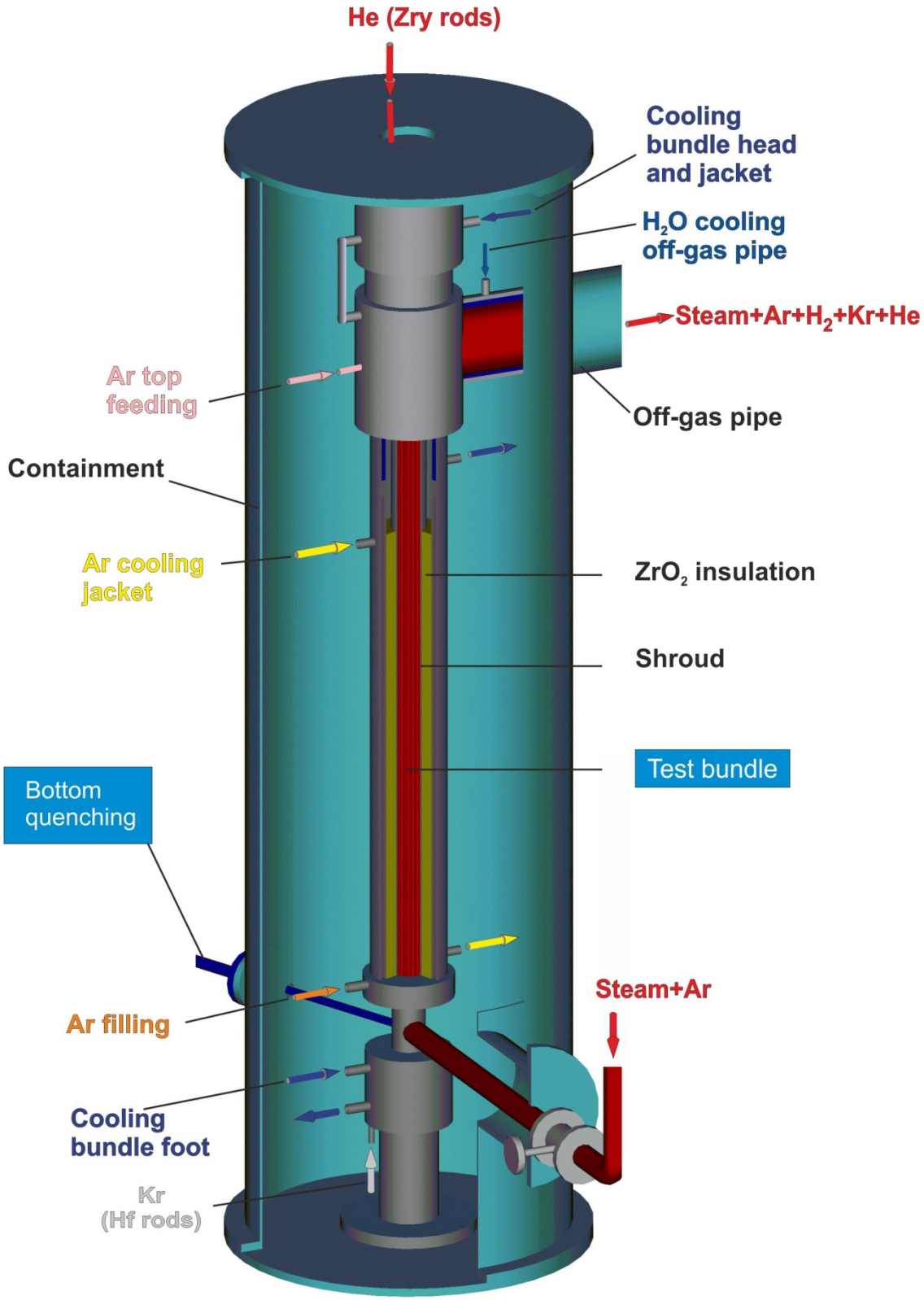

Figure 3 QUENCH-17; QUENCH facility: containment and test section.

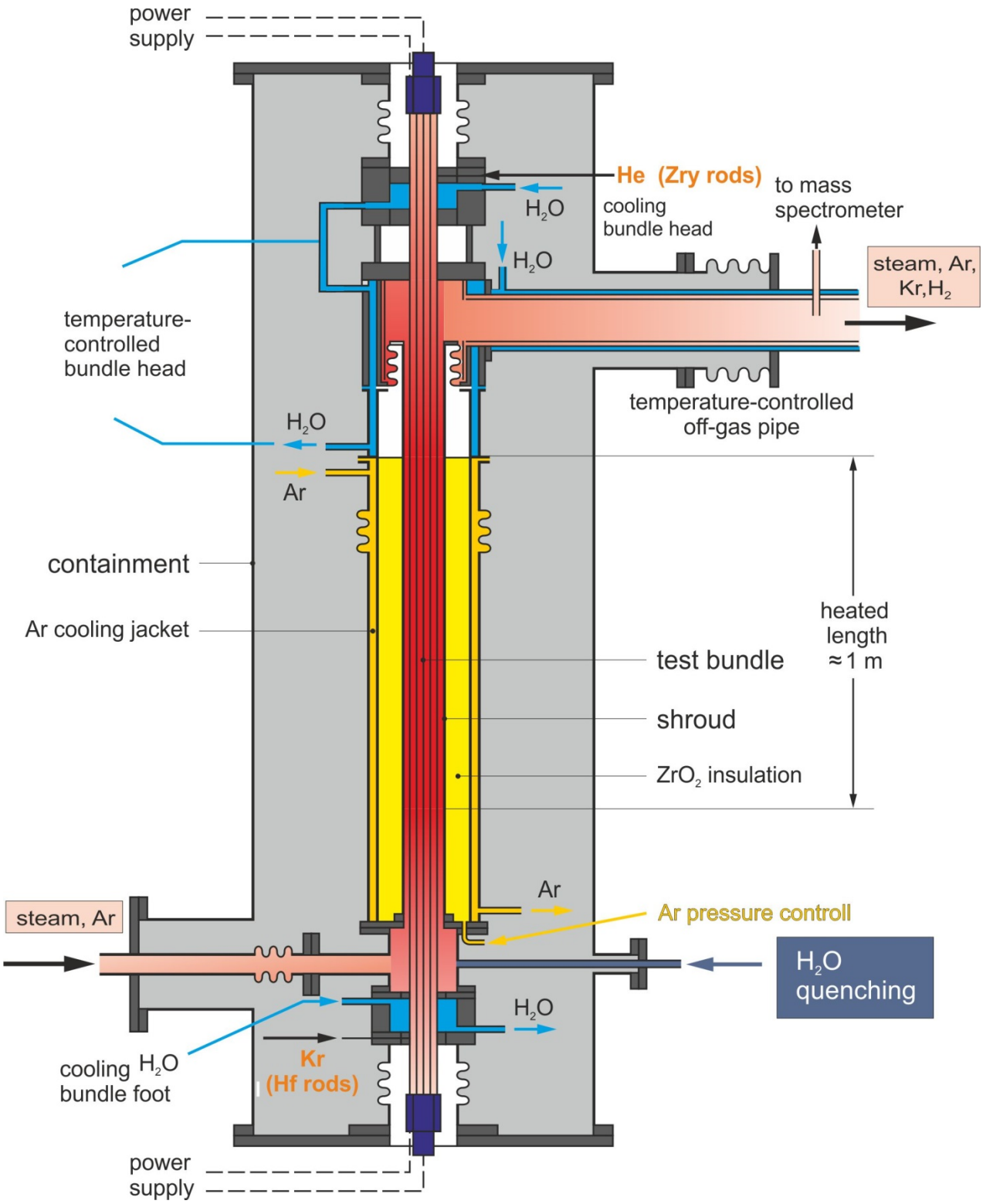

Figure 4 QUENCH-17; test section with flow lines.

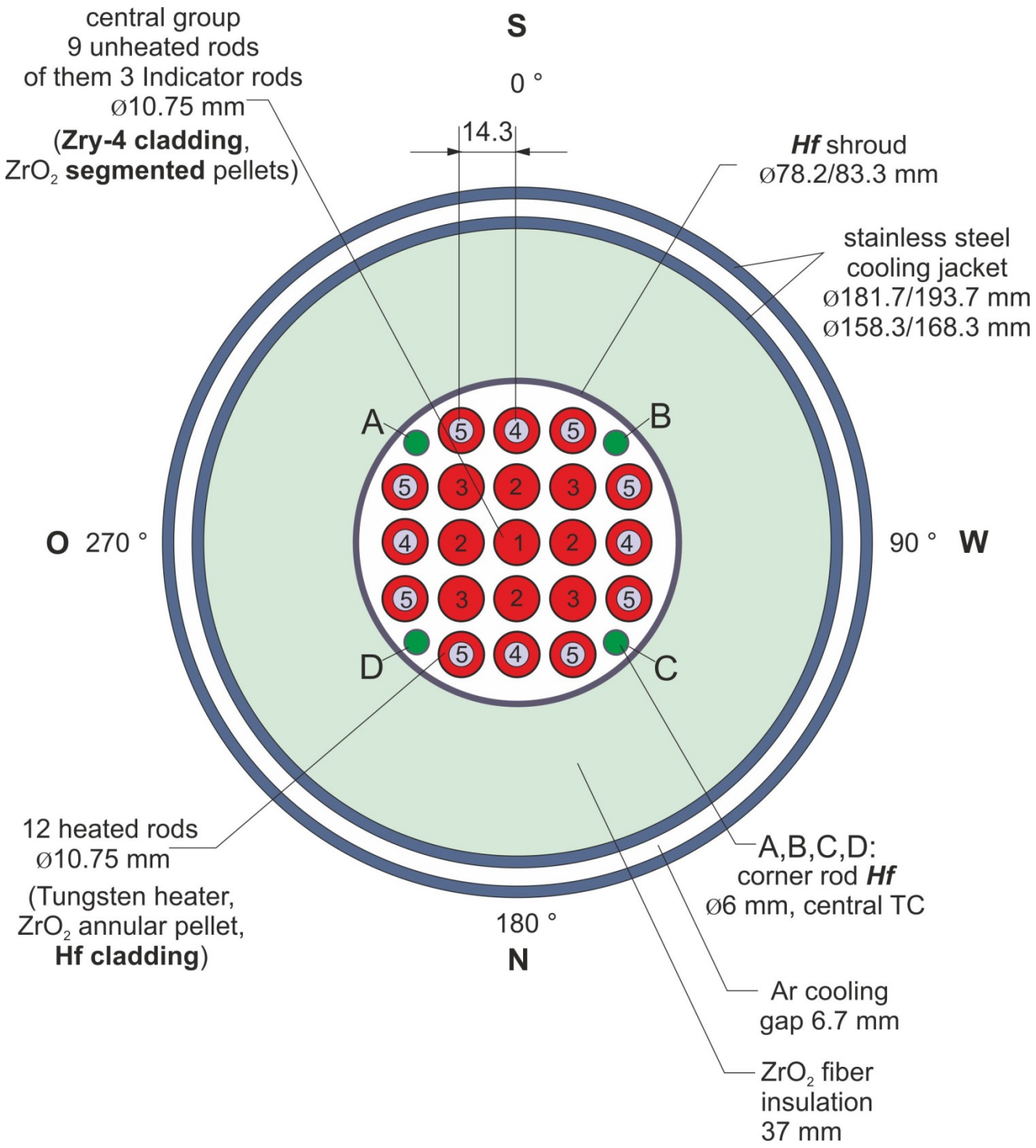

Figure 5 QUENCH-17; fuel rod simulator bundle (cross section, top view) including rod type indications

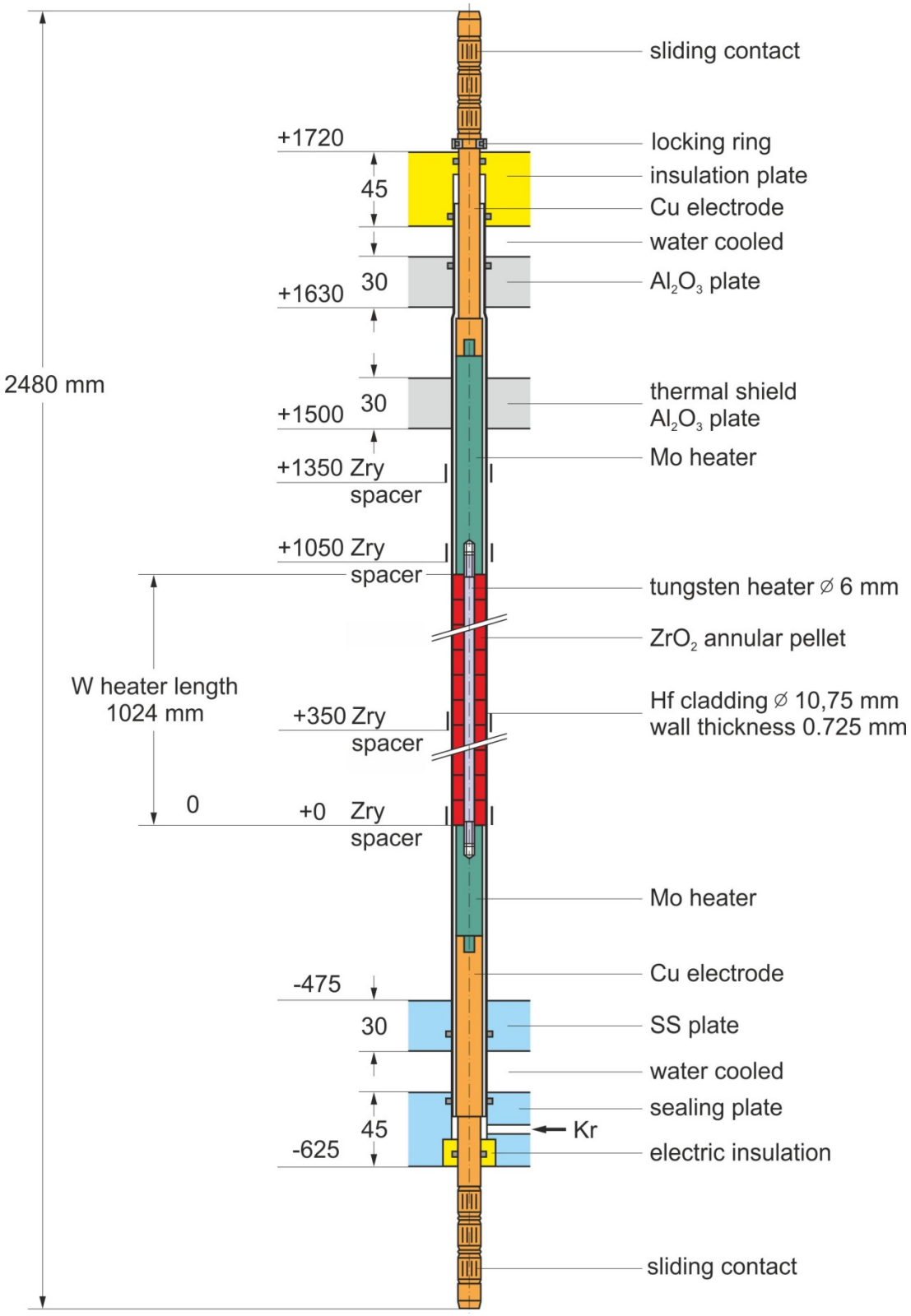

Figure 6 QUENCH-17; heated fuel rod simulator

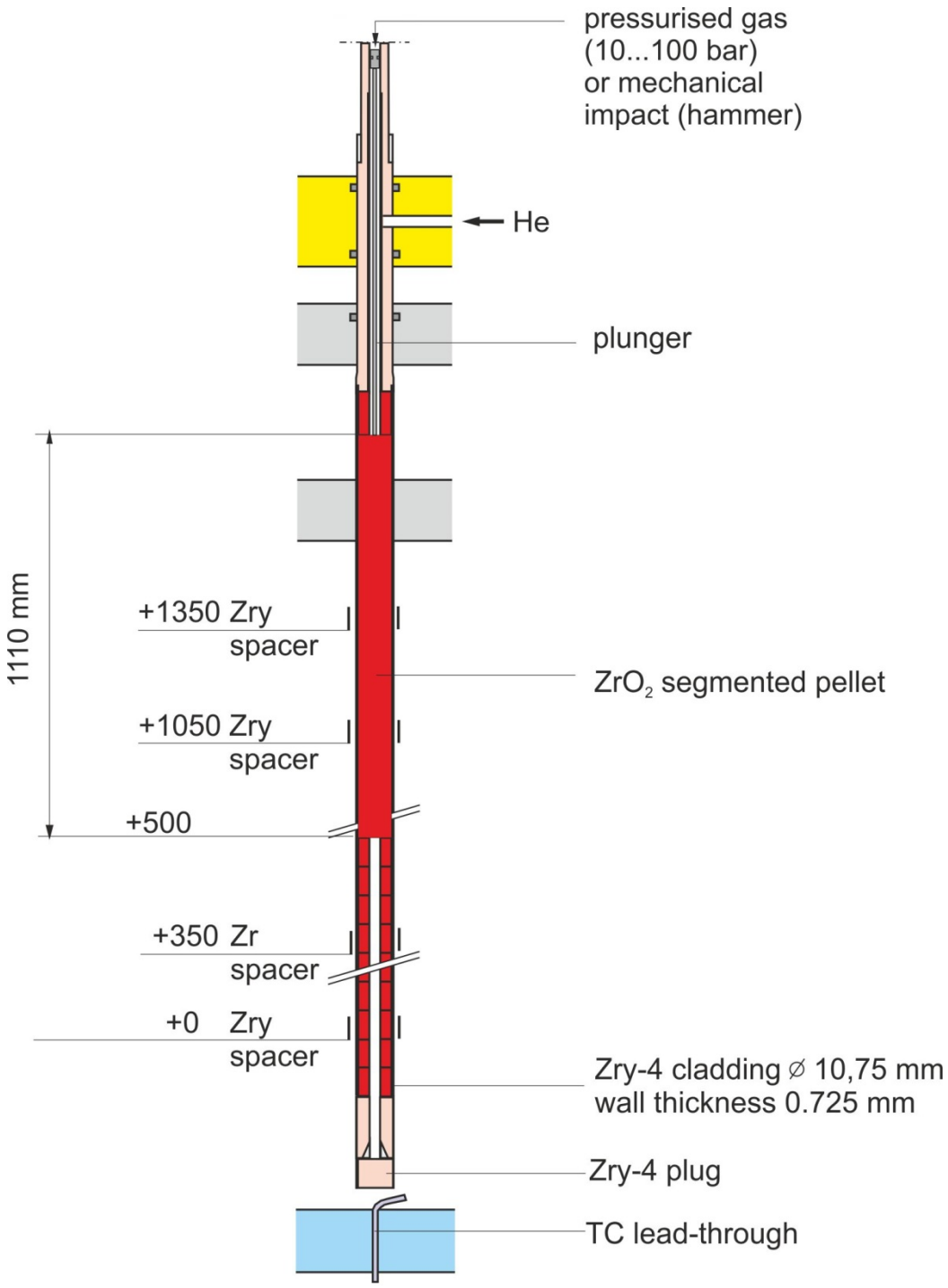

Figure 7 QUENCH-17; unheated fuel rod simulator

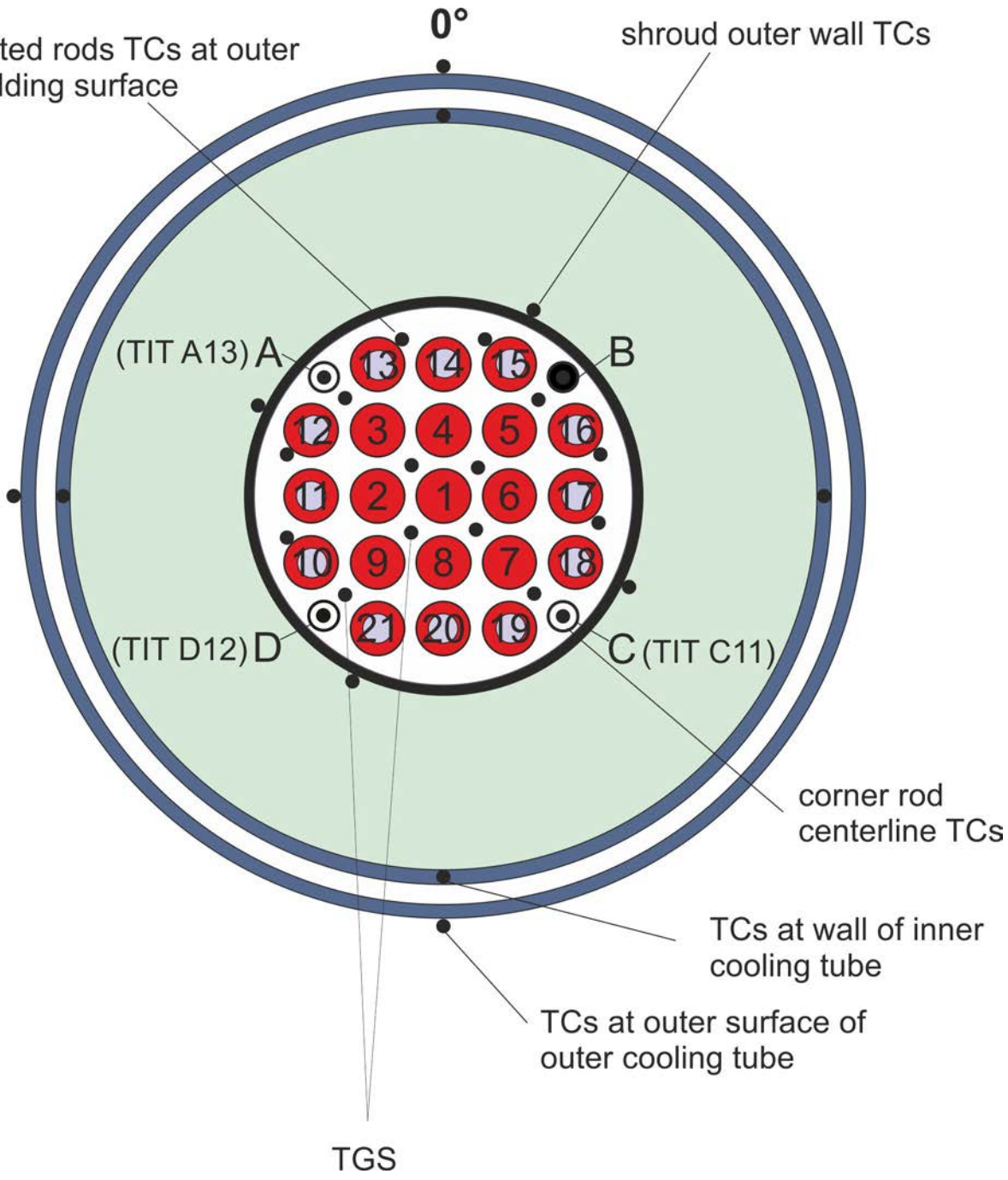

Figure 8 QUENCH-17; TC instrumentation and rod designation (top view).

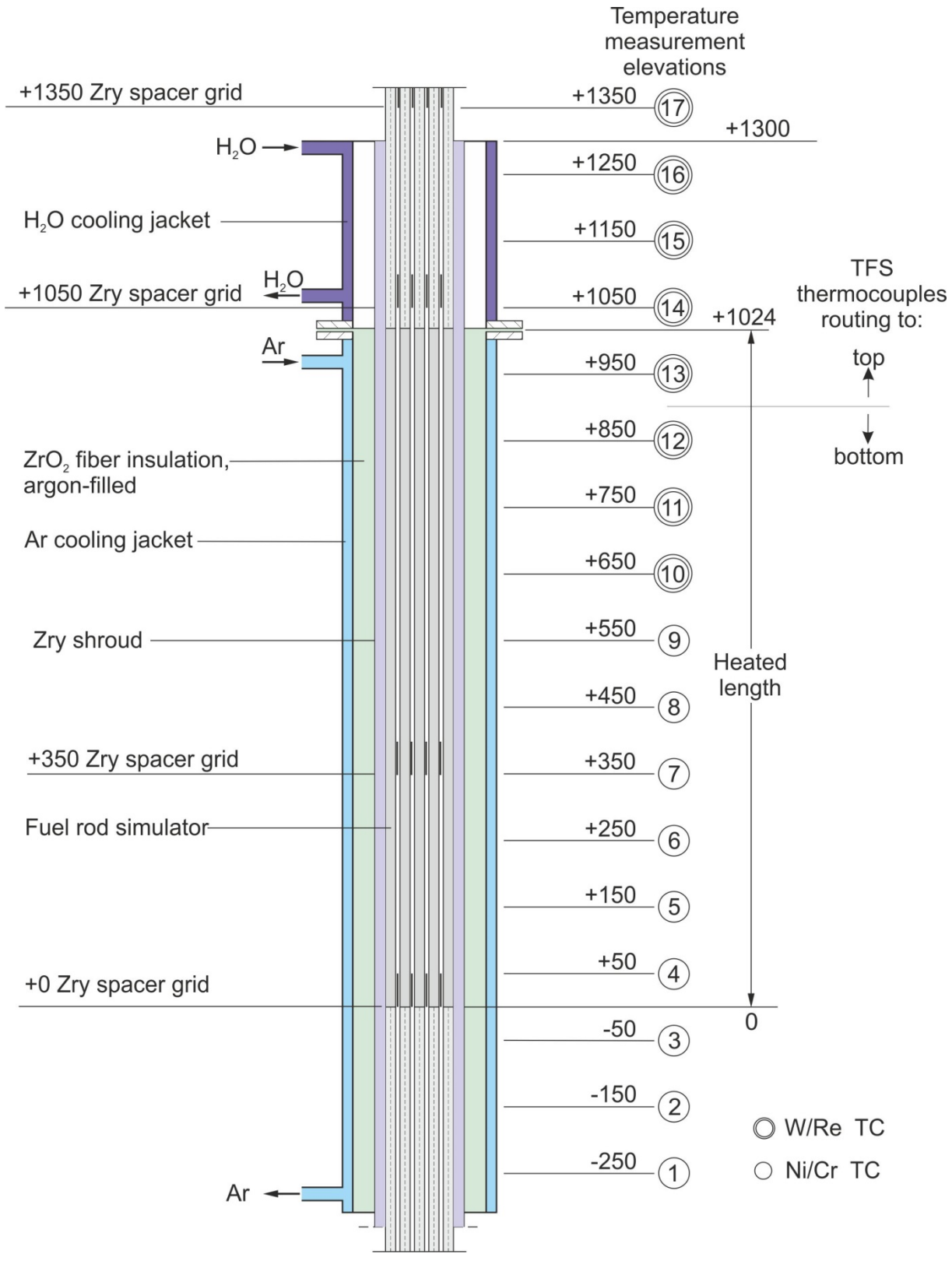

Figure 9 Axial temperature measurement locations in the QUENCH test section.

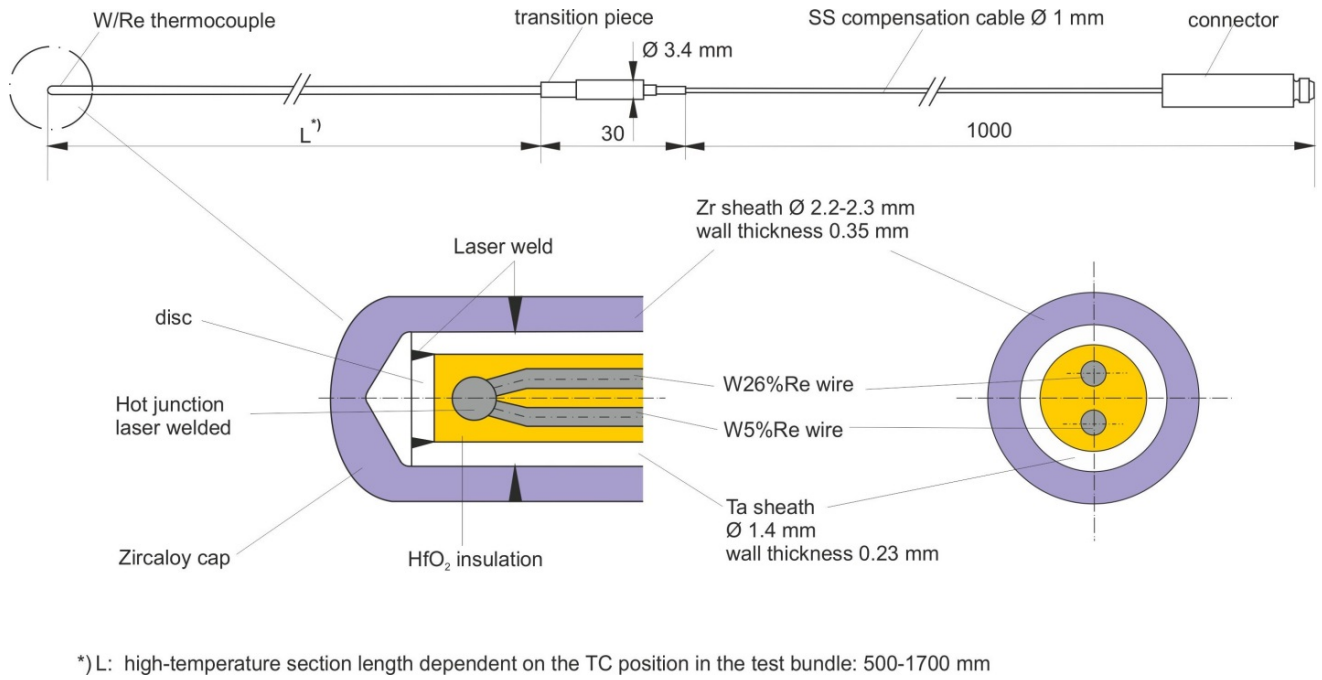

Figure 10 QUENCH; high-temperature thermocouple

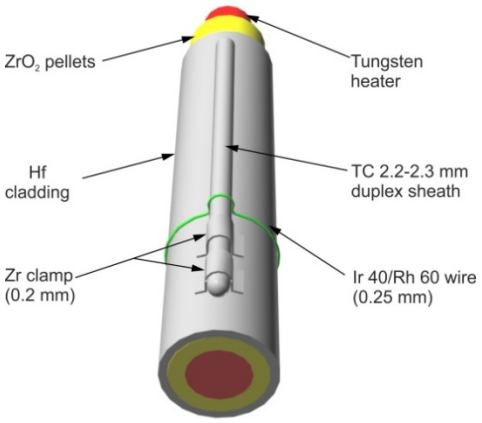

Figure 11 QUENCH-17; concept for TC fastening at the test rod

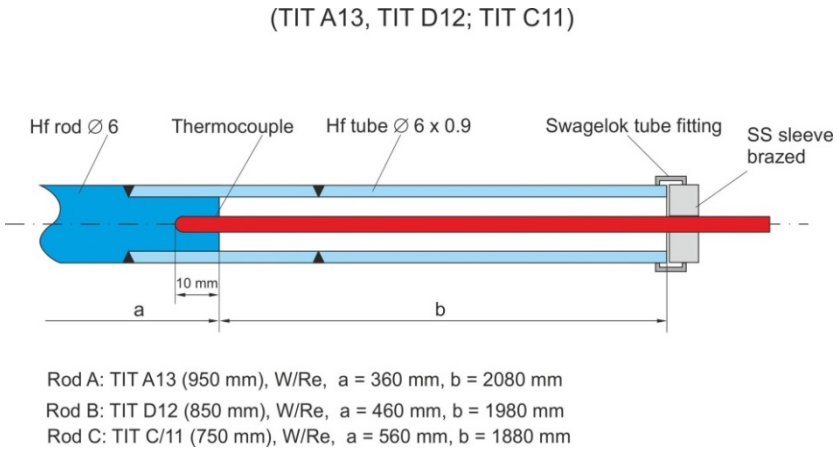

Figure 12 QUENCH-17; arrangement of the thermocouples inside the corner rods

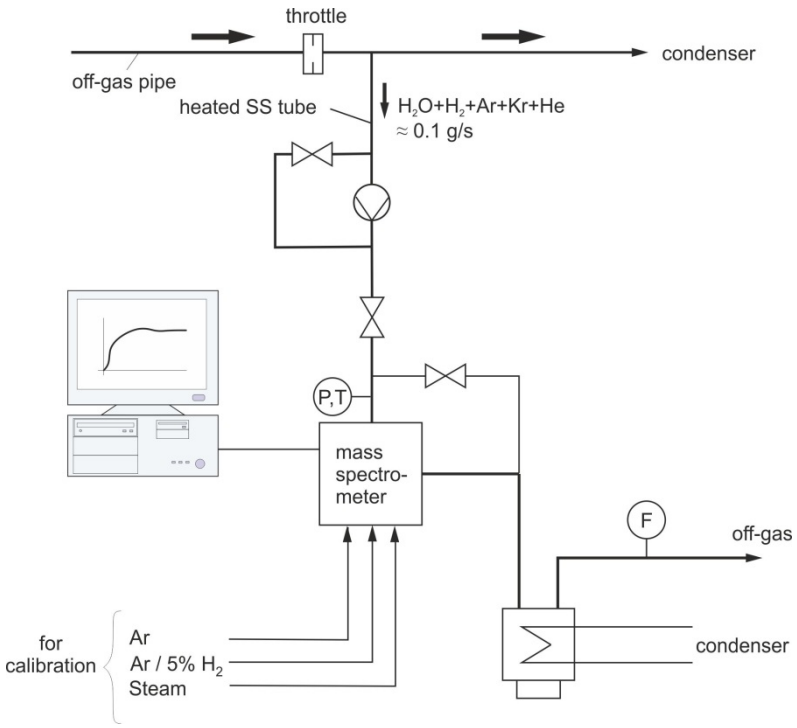

Figure 13 QUENCH-17; gas measurement with the GAM-300 mass spectrometer

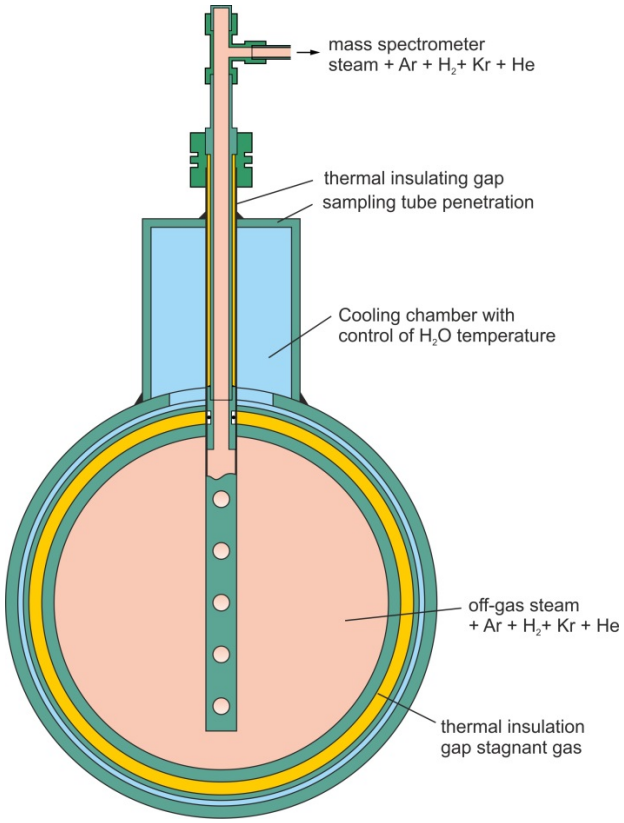

Figure 14 Mass spectrometer sampling position at the off-gas pipe of the QUENCH test facility

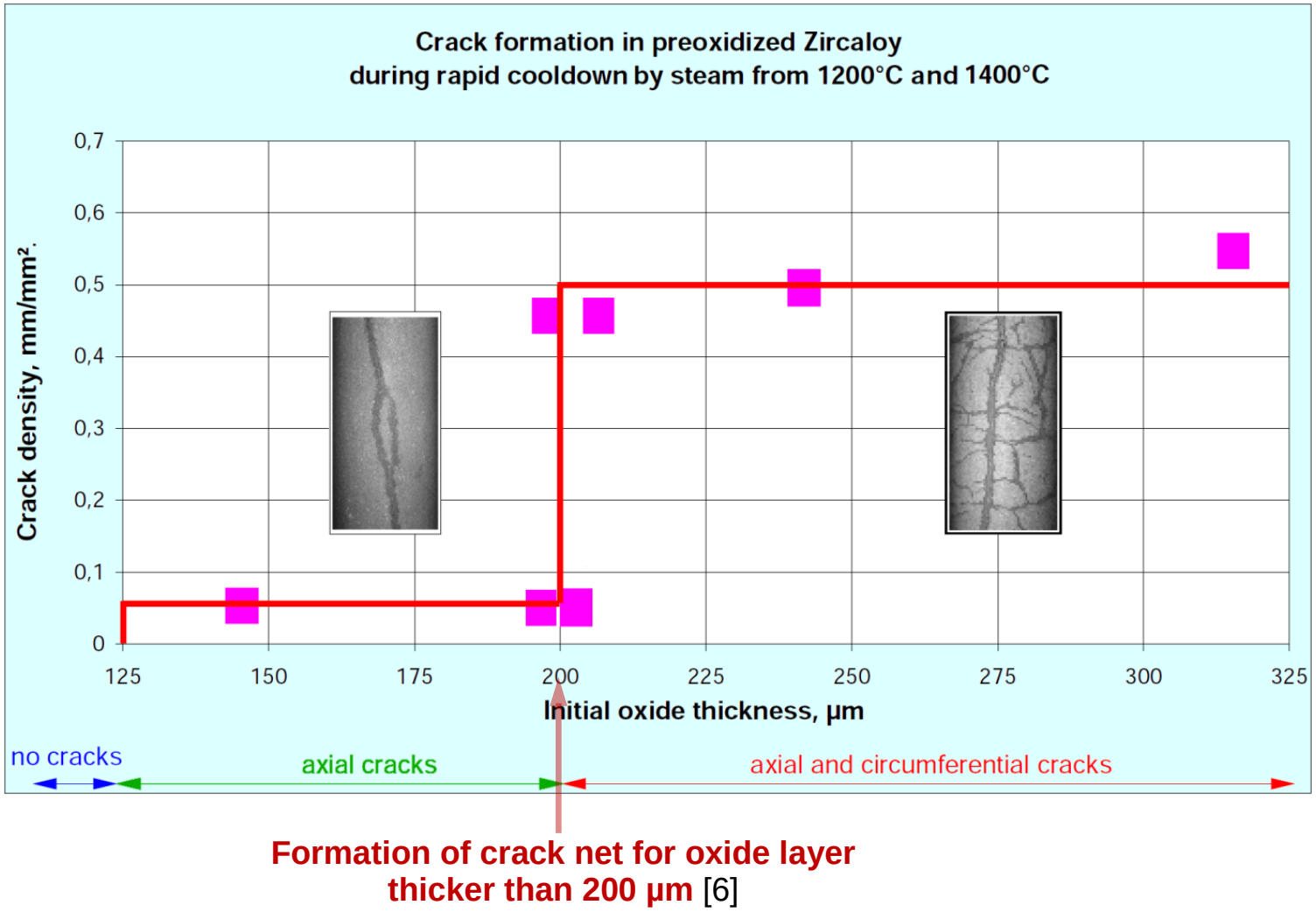

Figure 15 Formation of through going cracks in cladding quenched from high temperatures.

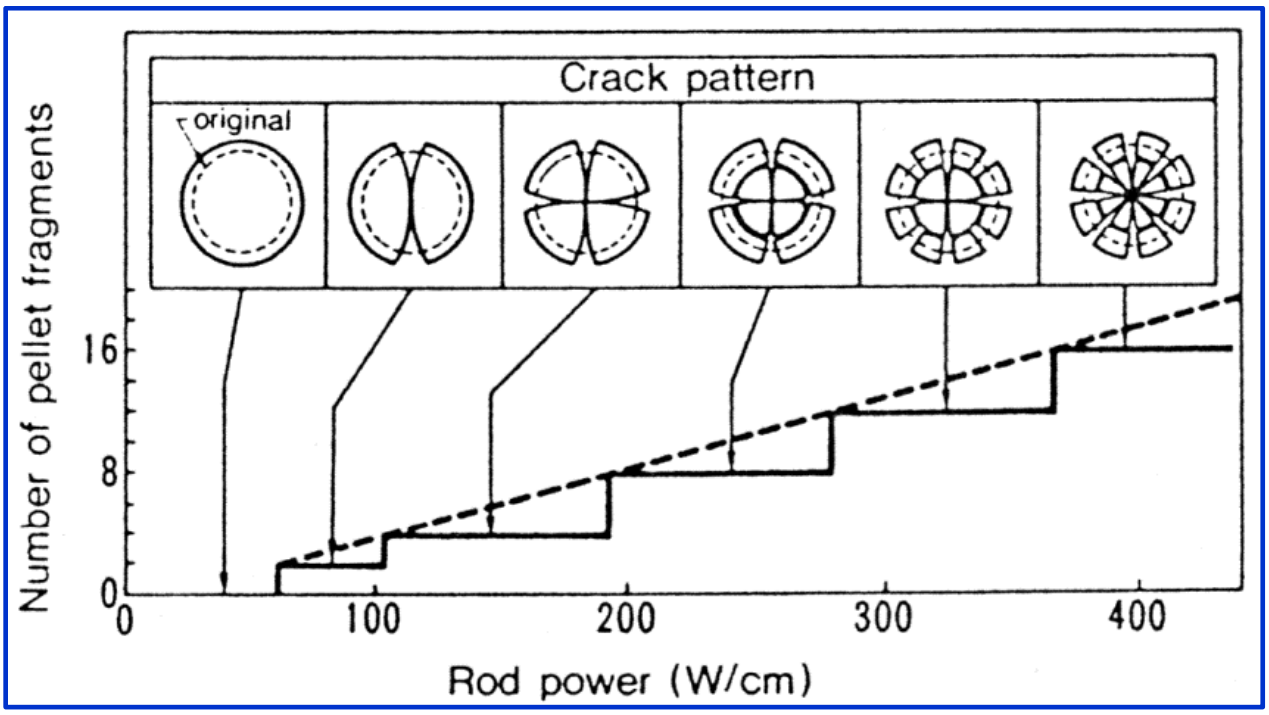

Pellet segmentation during operation [7]

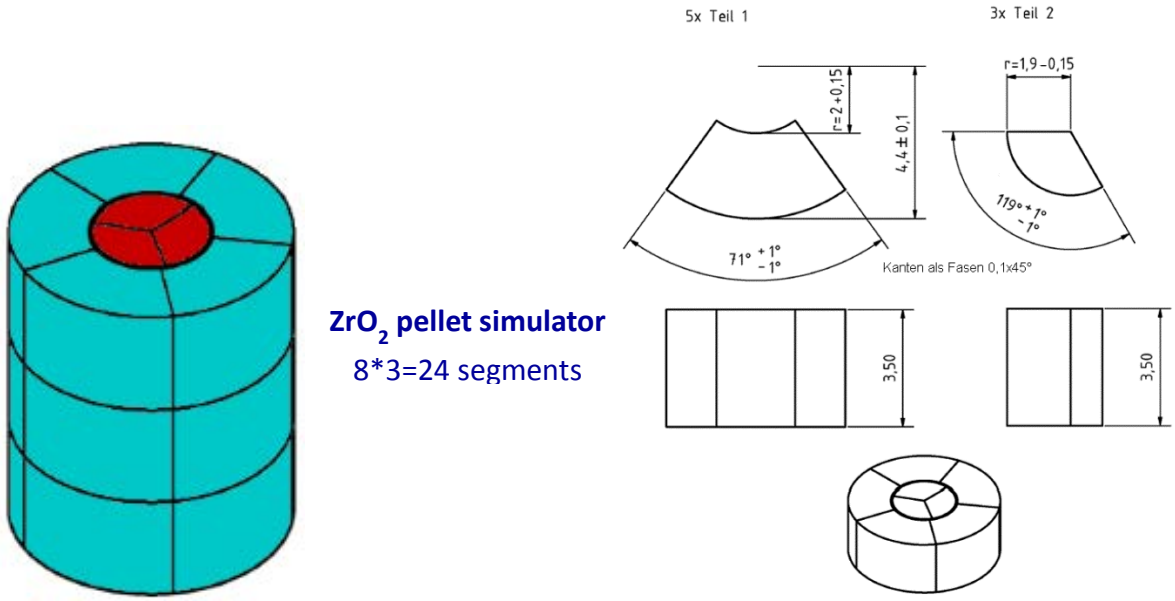

Figure 16 QUENCH-17; pre-segmented pellet

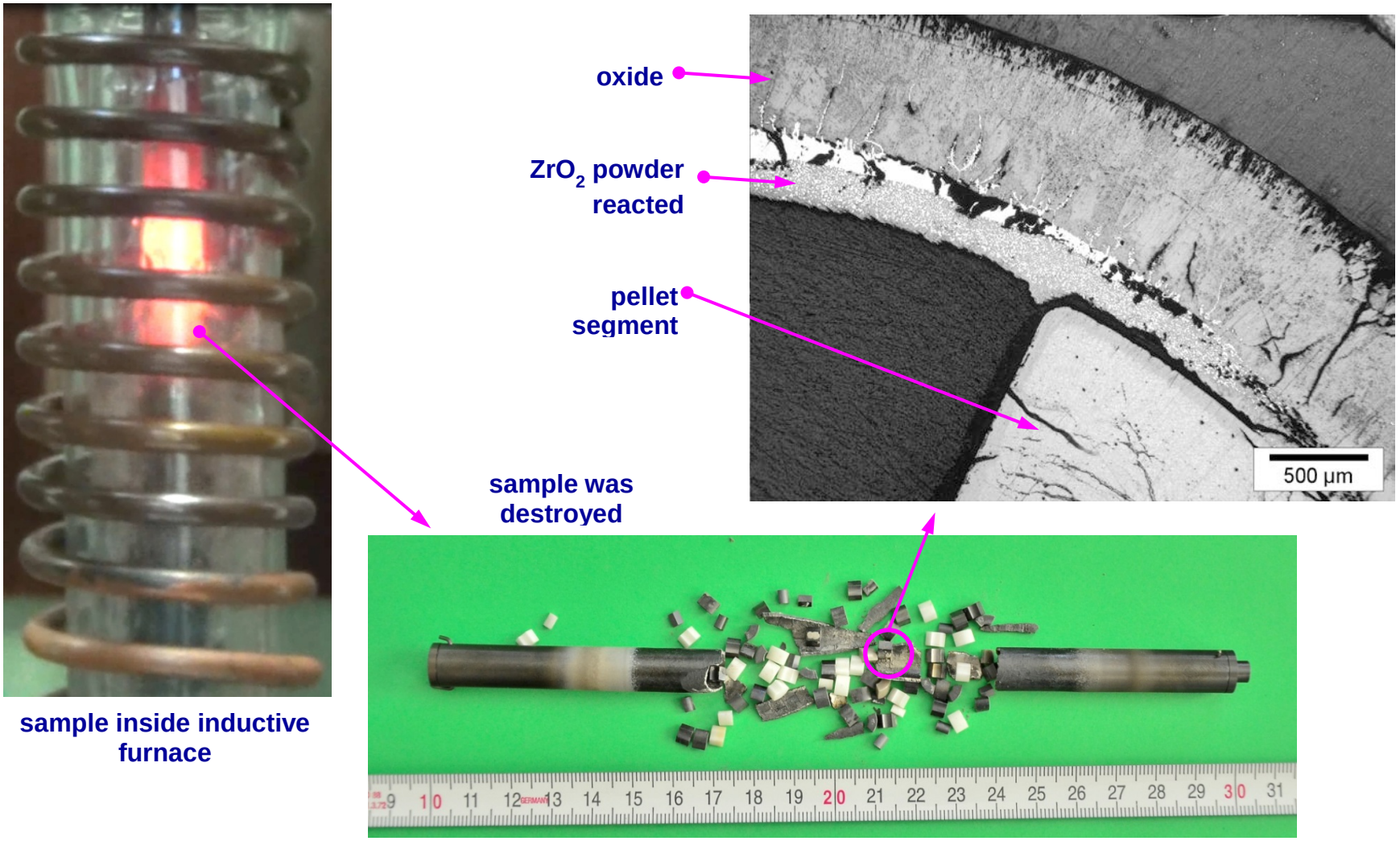

Figure 17 Quench single rod test with completely oxidized cladding filled with segmented pellets (oxidation at 1773 K during 11600 s, quench with water 80 g/h)

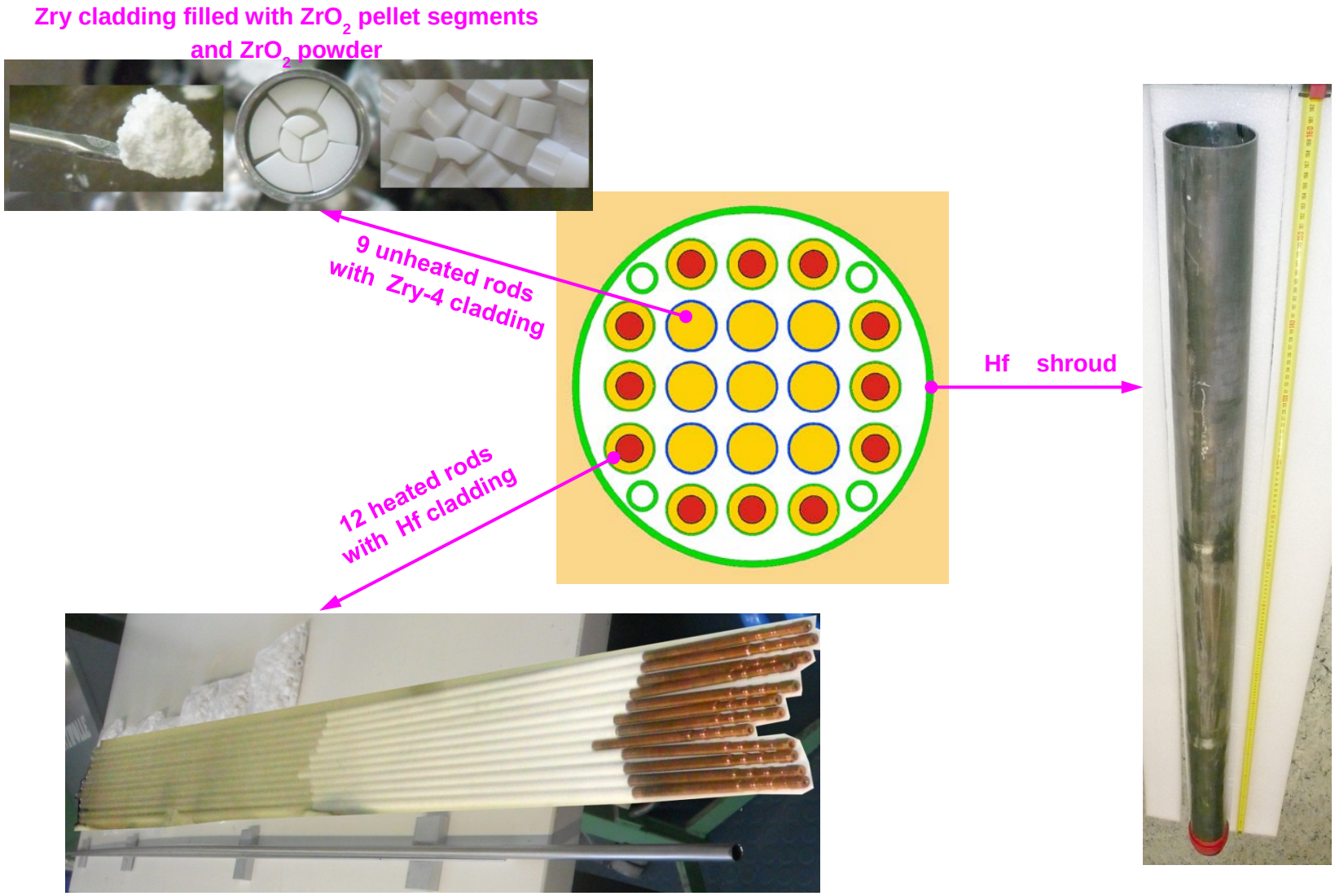

Figure 18 QUENCH-17; test bundle preparation

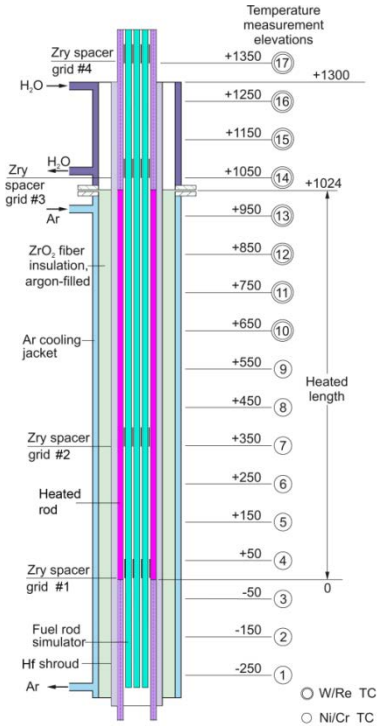

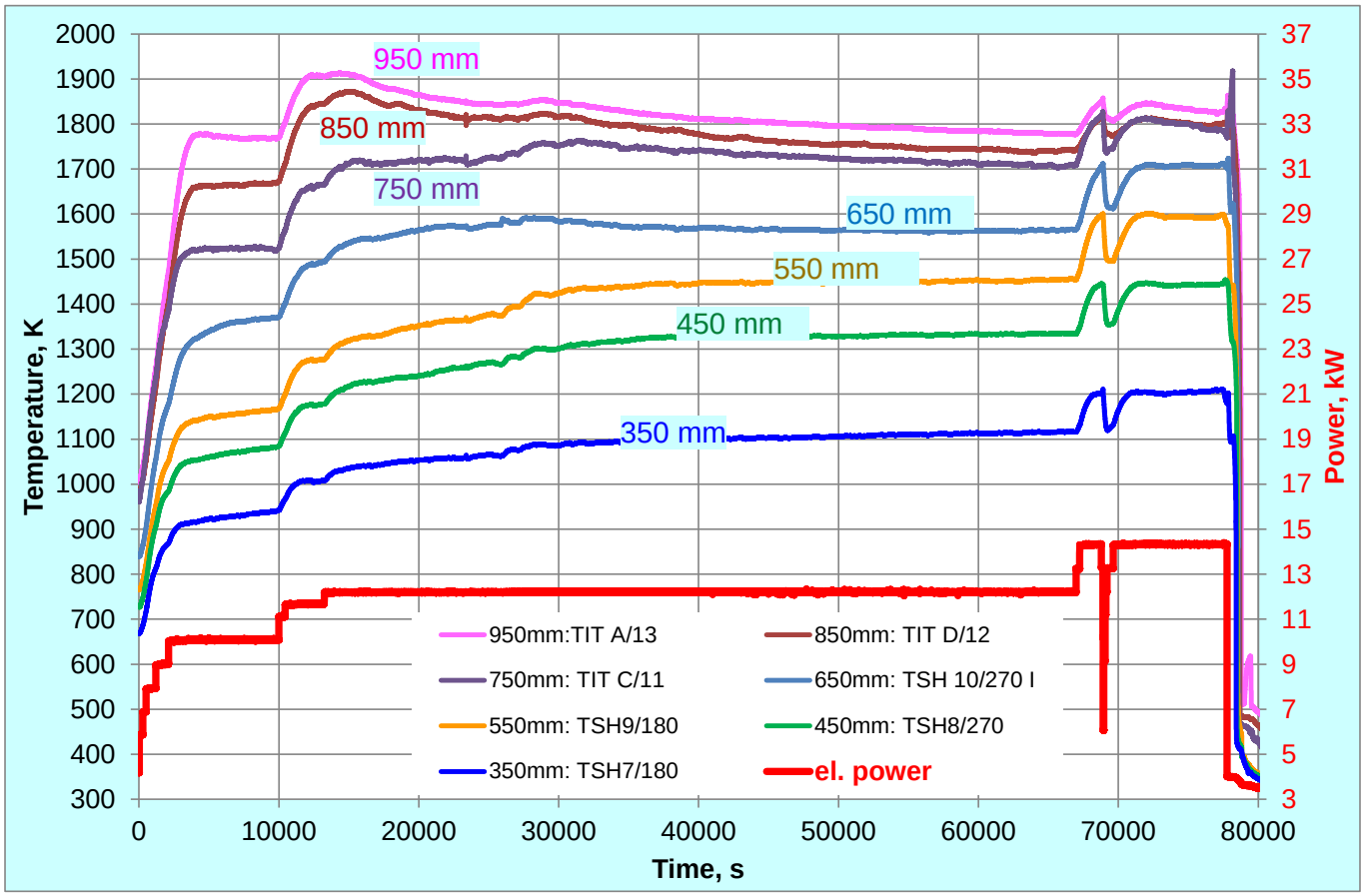

1) pre-oxidation stage with 2 g/s steam and 2 g/s Ar. Complete oxidation of Zry-4 clads between 650 and 1150 mm
2) Test termination: reflood from bottom with water flow rate 10 g/s.

Figure 19 QUENCH-17; test scenario: el. power and TC readings at different elevations

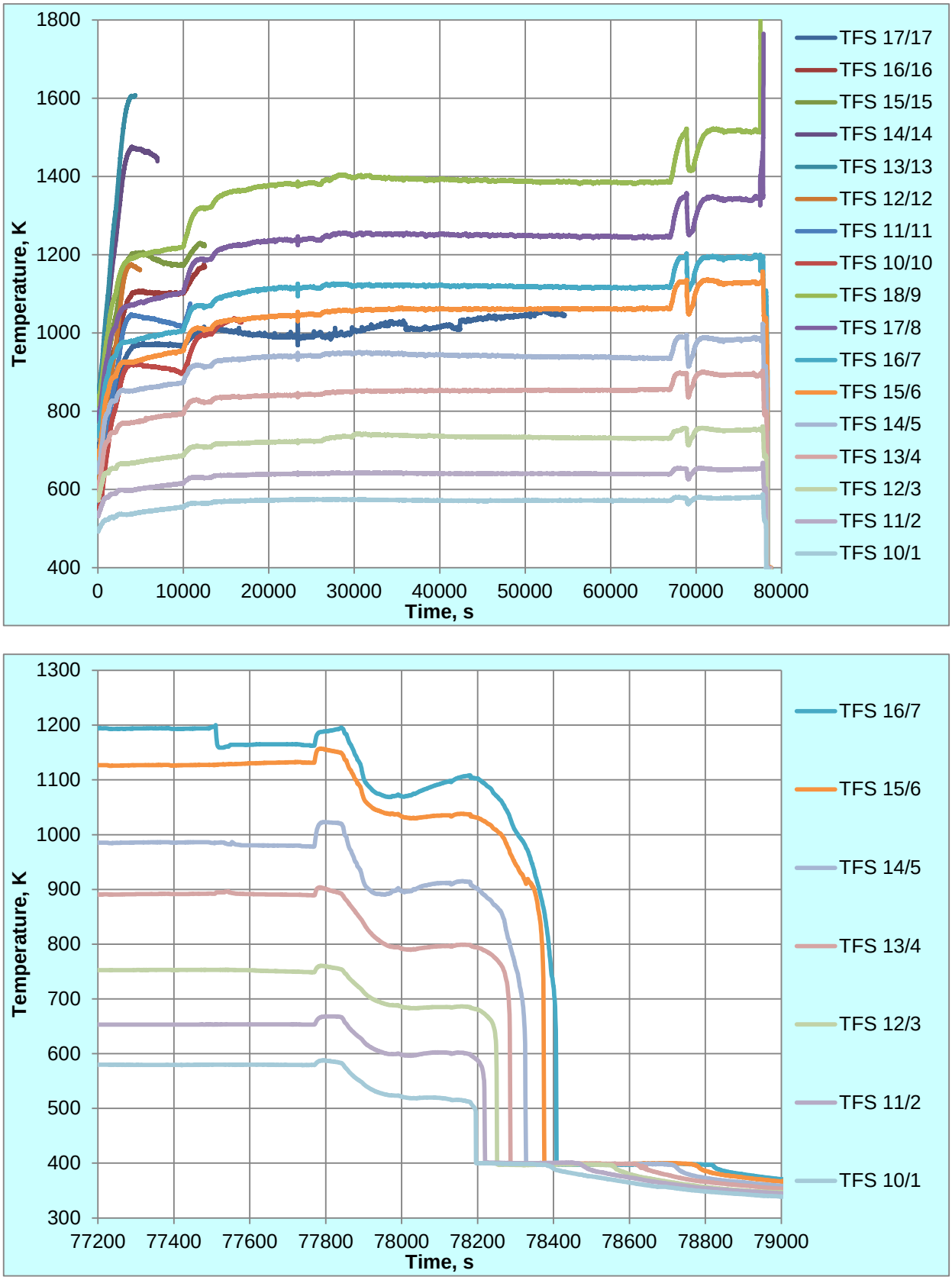

Figure 20 QUENCH-17; readings of all TFS thermocouples during the whole test (top) and survived lower TFS during the quench phase (down)

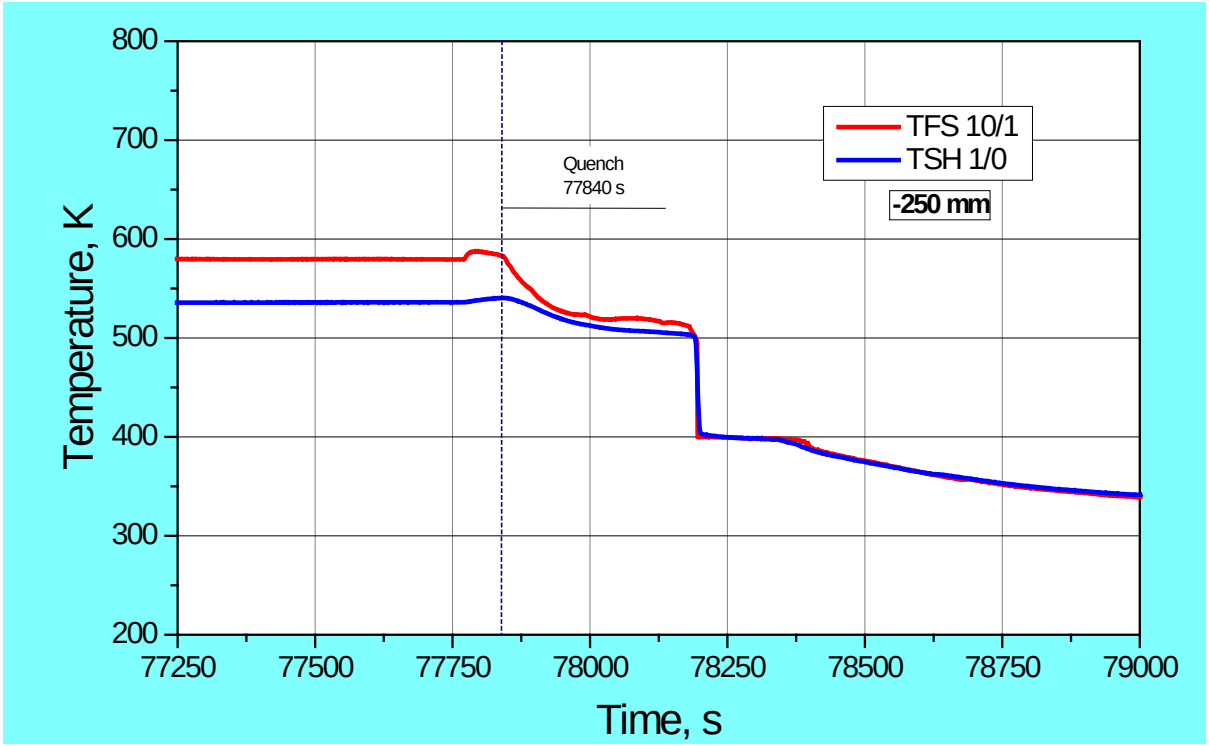

Figure 21 QUENCH-17; temperatures measured by rod cladding (TFS 10/1) and shroud (TSH 1/0) thermocouple at -250 mm elevation.

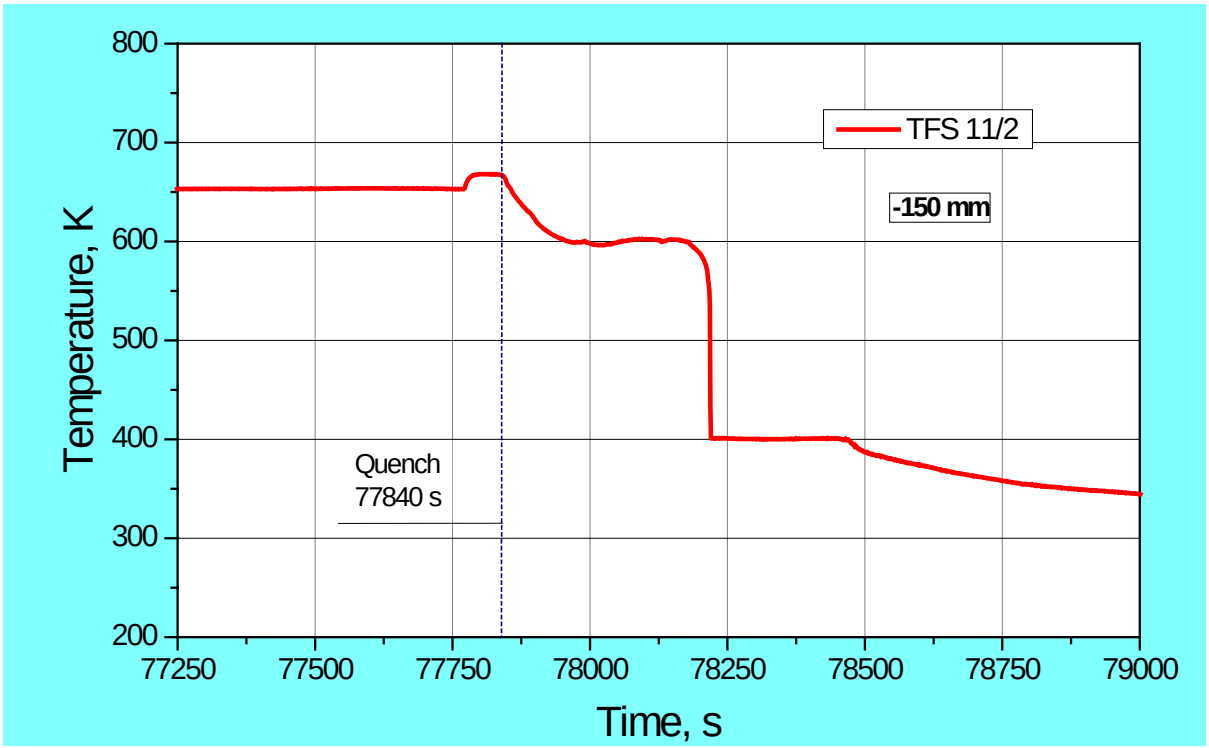

Figure 22 QUENCH-17; temperatures measured by rod cladding (TFS 11/2) thermocouple at -150 mm elevation.

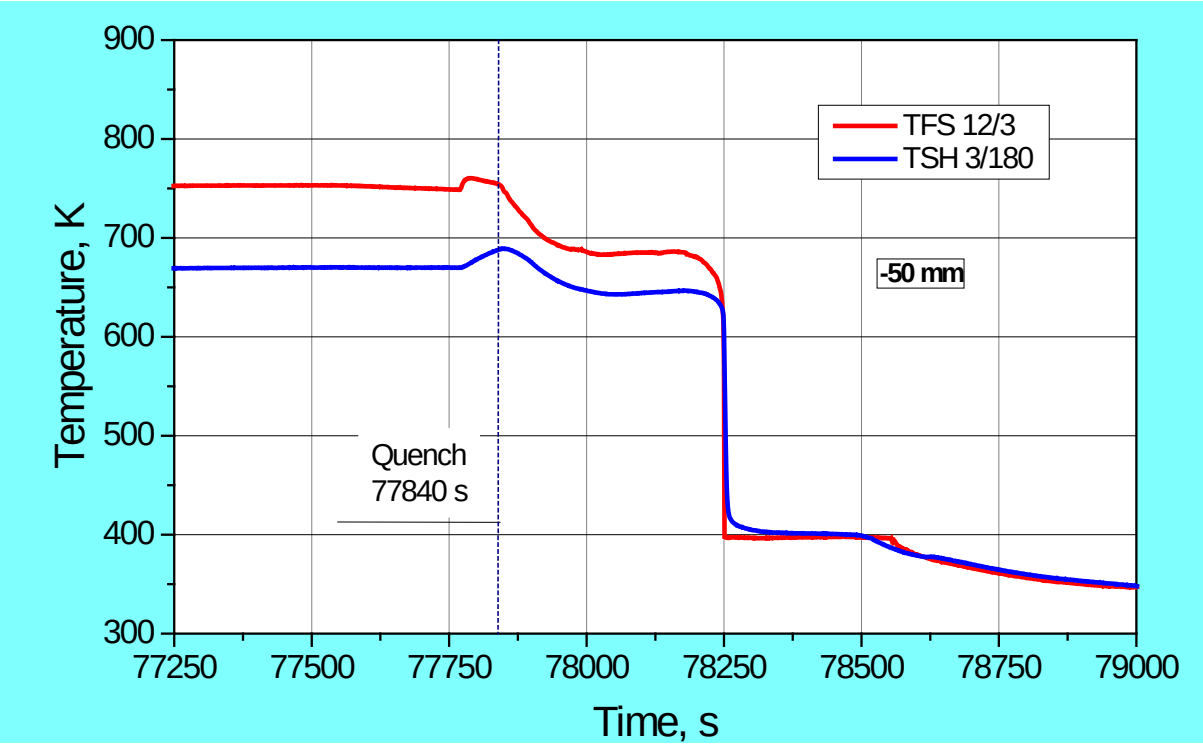

Figure 23 QUENCH-17; temperatures measured by rod cladding (TFS 12/3) and shroud (TSH 3/180) thermocouples at -50 mm elevation.

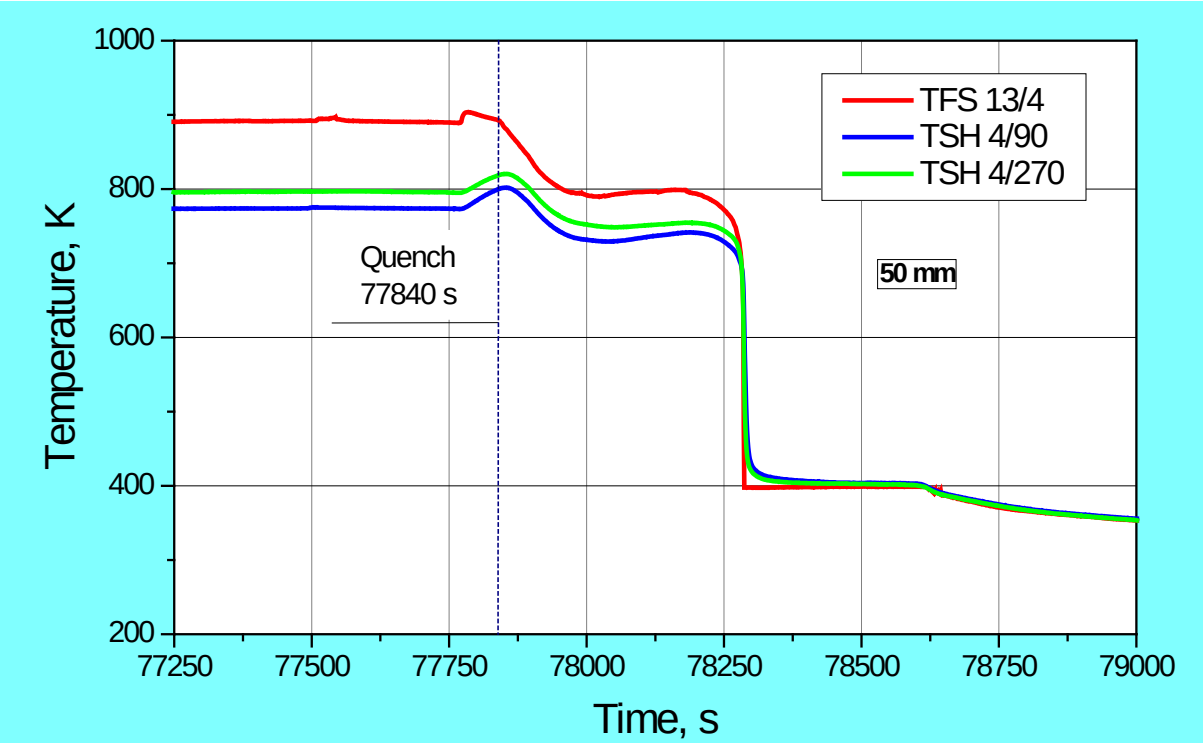

Figure 24 QUENCH-17; temperatures measured by rod cladding (TFS 13/4) and shroud (TSH) thermocouples at 50 mm elevation.

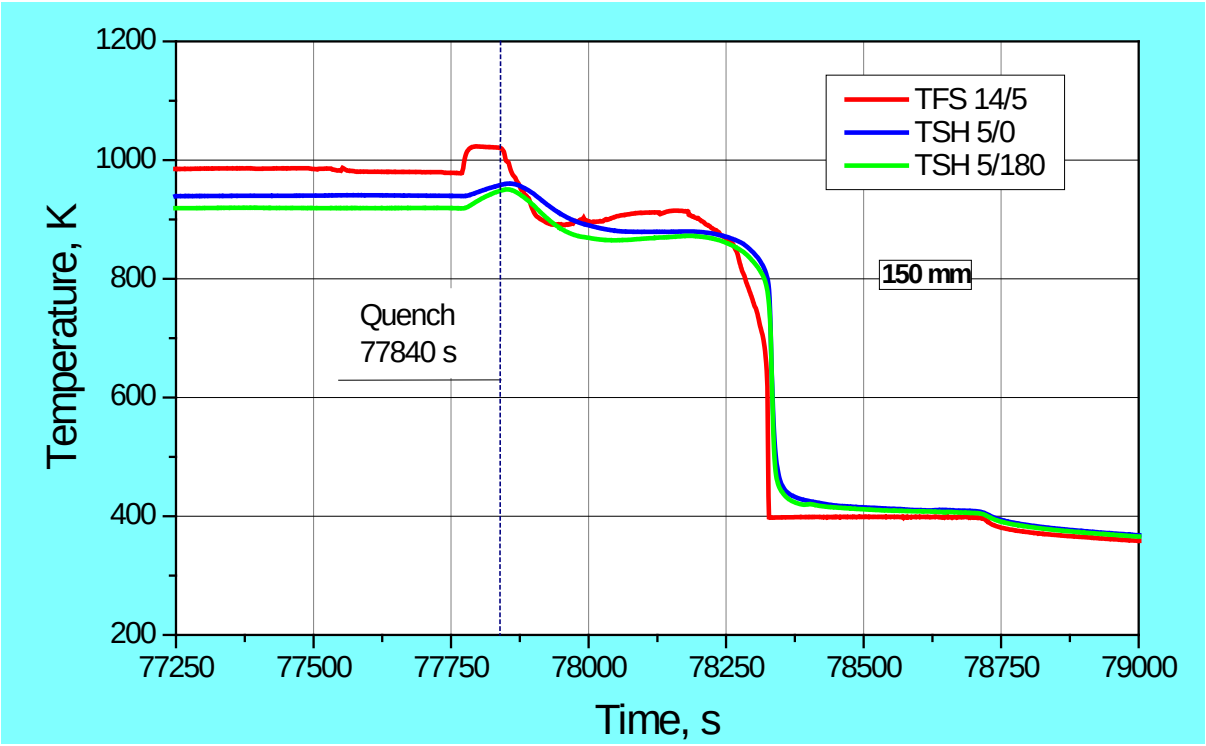

Figure 25 QUENCH-17; temperatures measured by rod cladding (TFS 14/5) and shroud (TSH) thermocouples at 150 mm elevation.

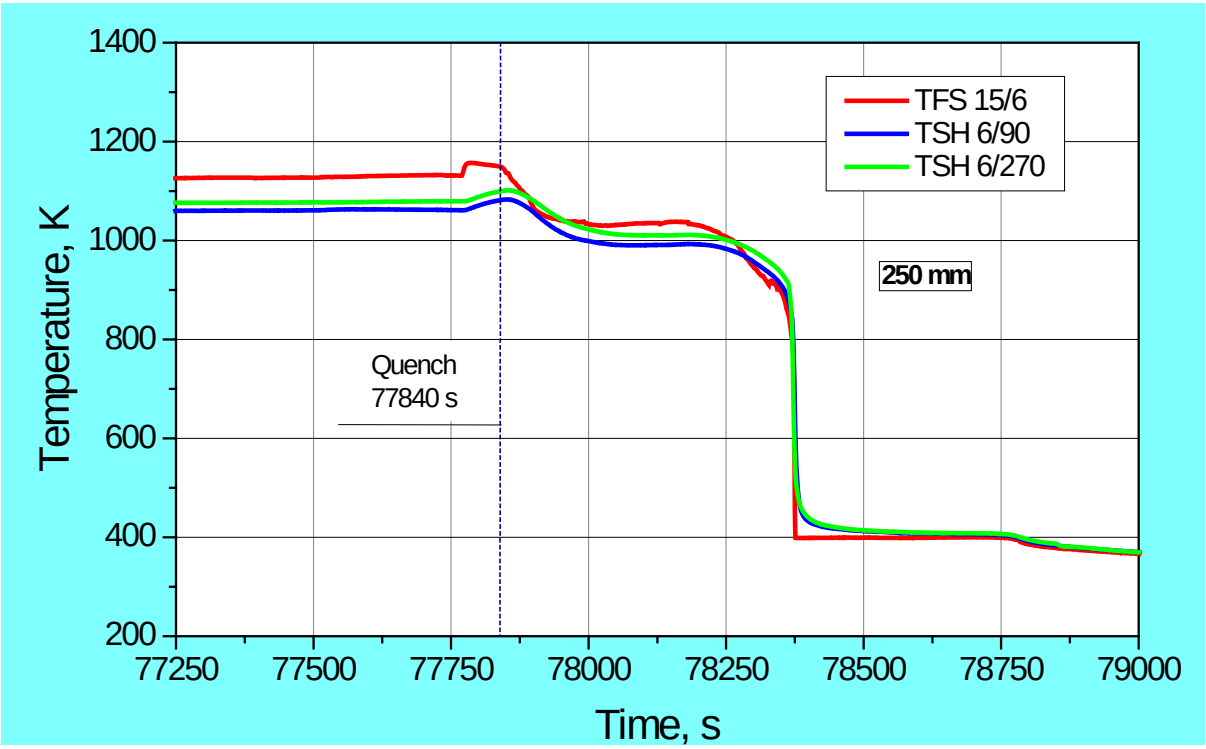

Figure 26 QUENCH-17; temperatures measured by rod cladding (TFS 15/6) and shroud (TSH) thermocouples at 250 mm elevation.

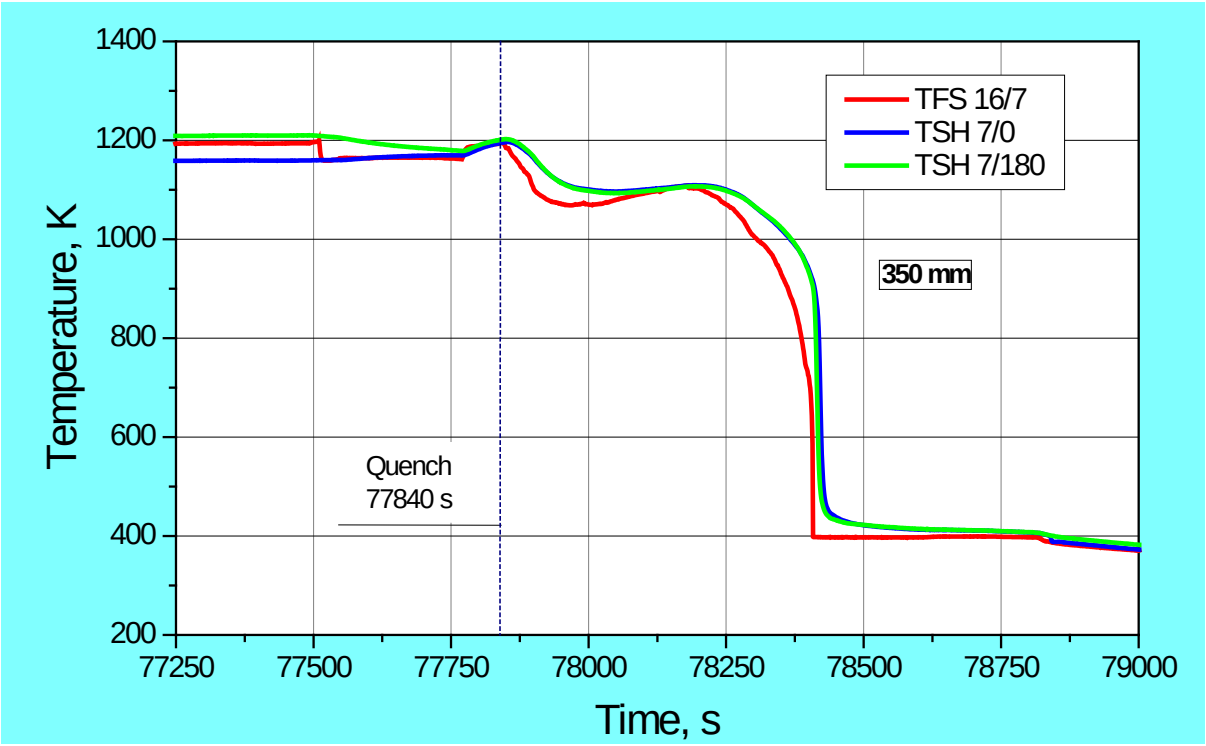

Figure 27 QUENCH-17; temperatures measured by rod cladding (TFS 16/7) and shroud (TSH) thermocouples at 350 mm elevation.

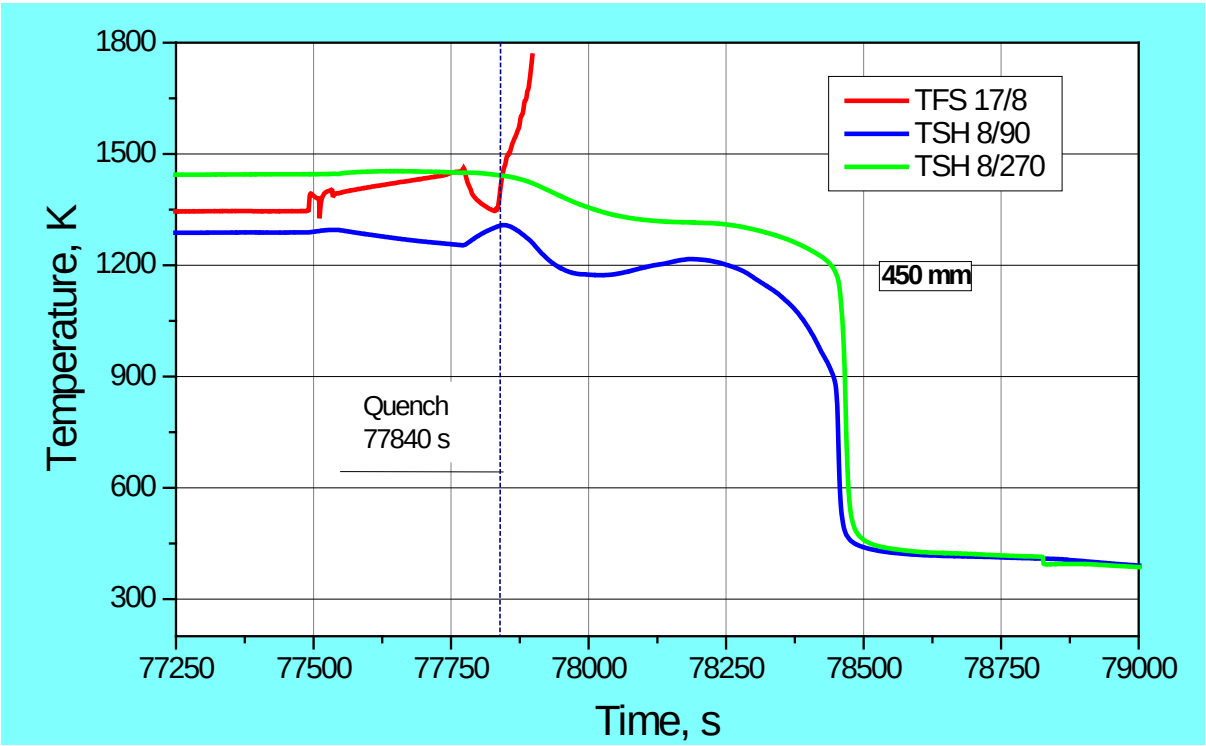

Figure 28 QUENCH-17; temperatures measured by rod cladding (TFS 17/8) and shroud (TSH) thermocouples at 450 mm elevation.

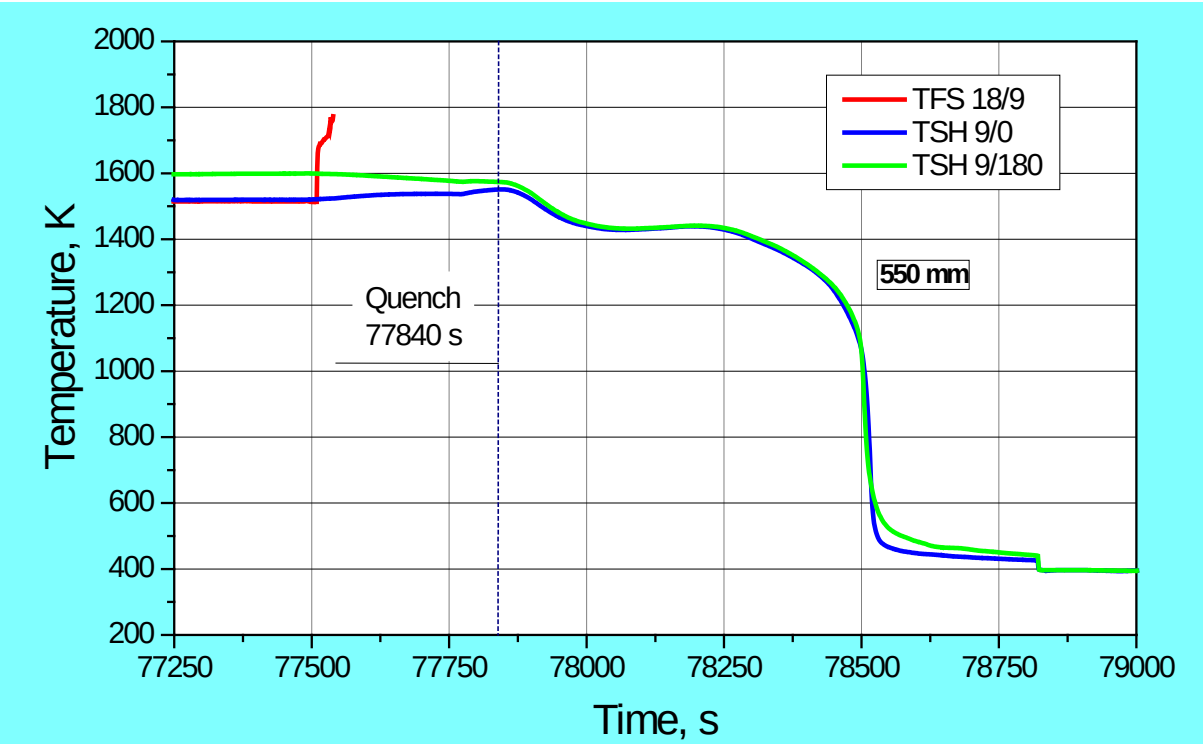

Figure 29 QUENCH-17; temperatures measured by rod cladding (TFS 18/9) and shroud (TSH) thermocouples at 550 mm elevation.

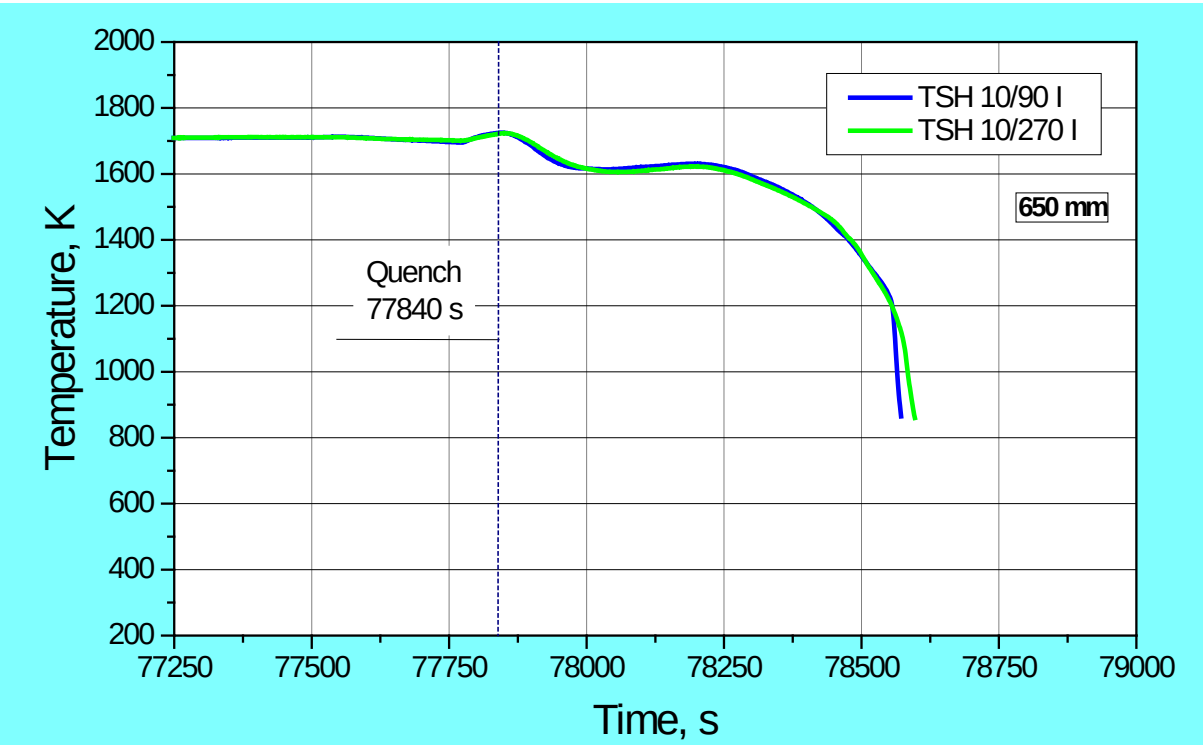

Figure 30 QUENCH-17; temperatures measured by shroud (TSH) thermocouples at 650 mm elevation.

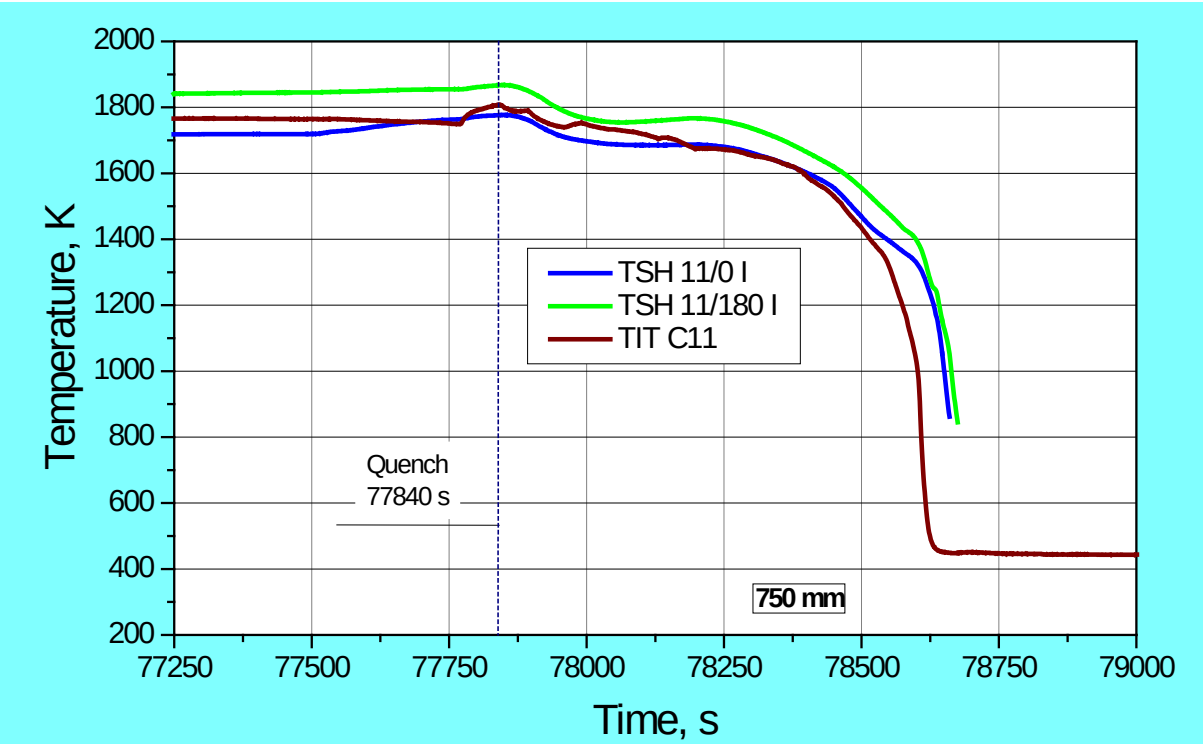

Figure 31 QUENCH-17; temperatures measured by shroud (TSH) and corner rod internal (TIT C/11) thermocouples at 750 mm elevation.

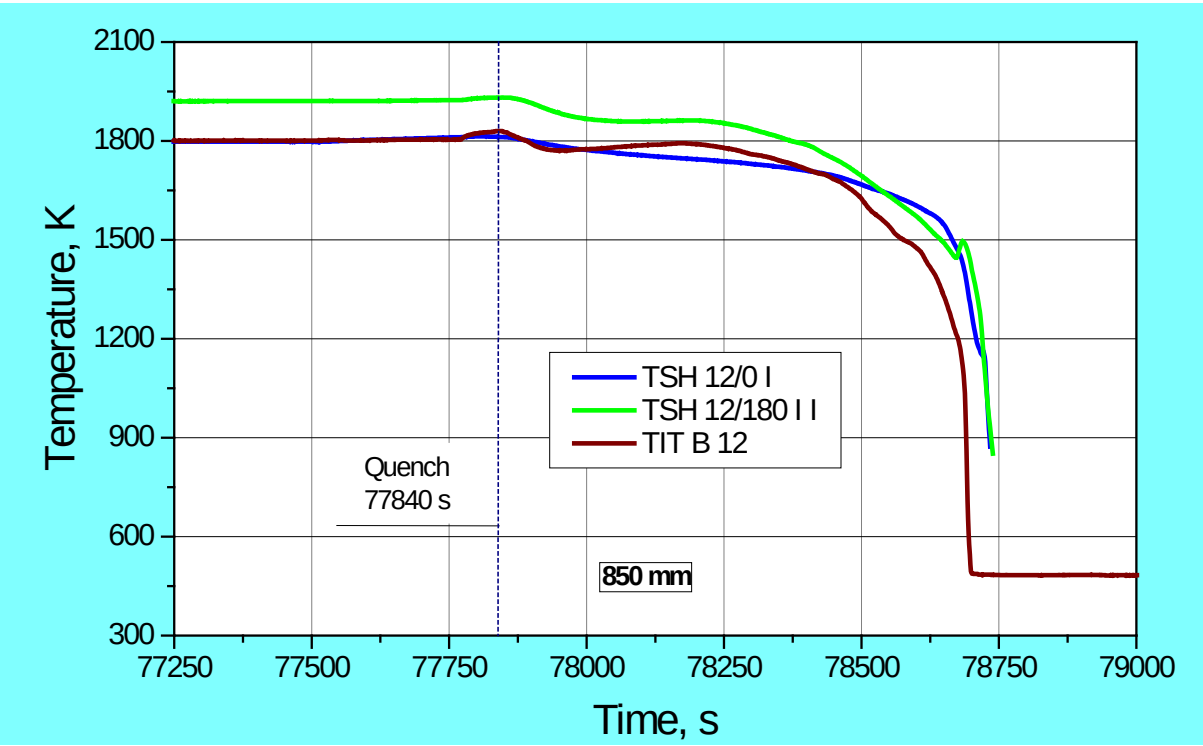

Figure 32 QUENCH-17; temperatures measured by shroud (TSH) and corner rod internal (TIT B/12) thermocouples at 850 mm elevation.

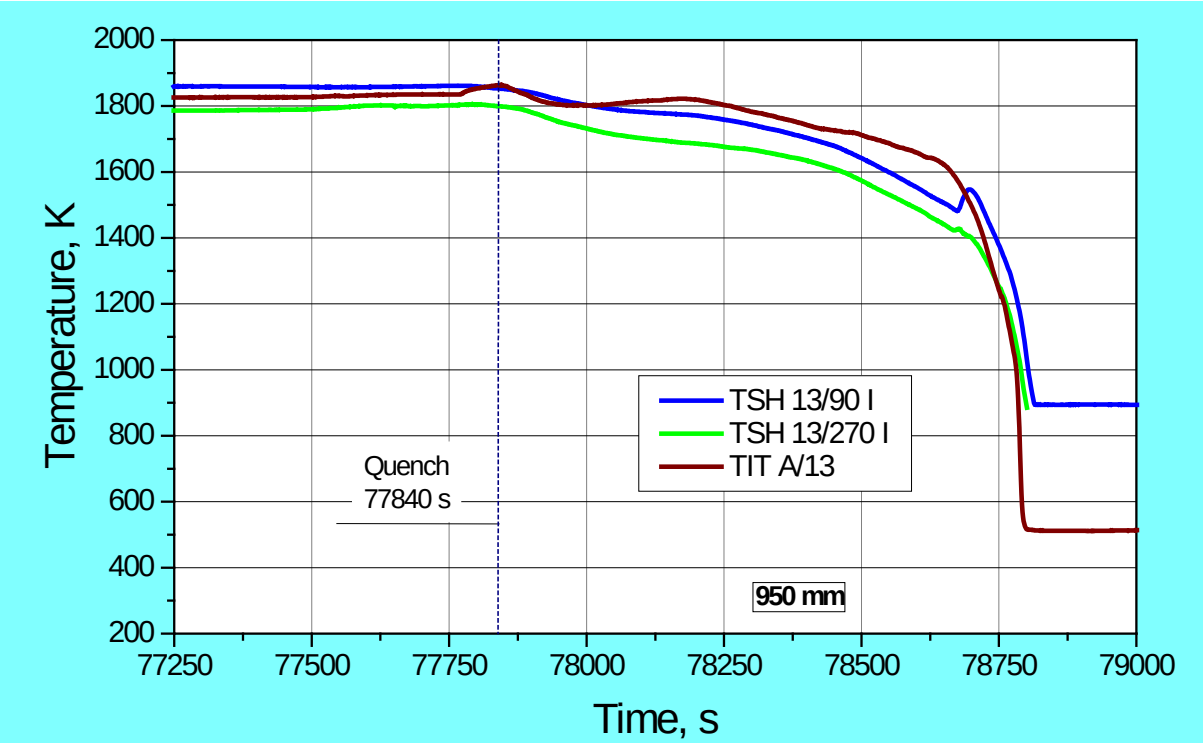

Figure 33 QUENCH-17; temperatures measured by shroud (TSH) and corner rod internal (TIT) thermocouples at 950 mm elevation.

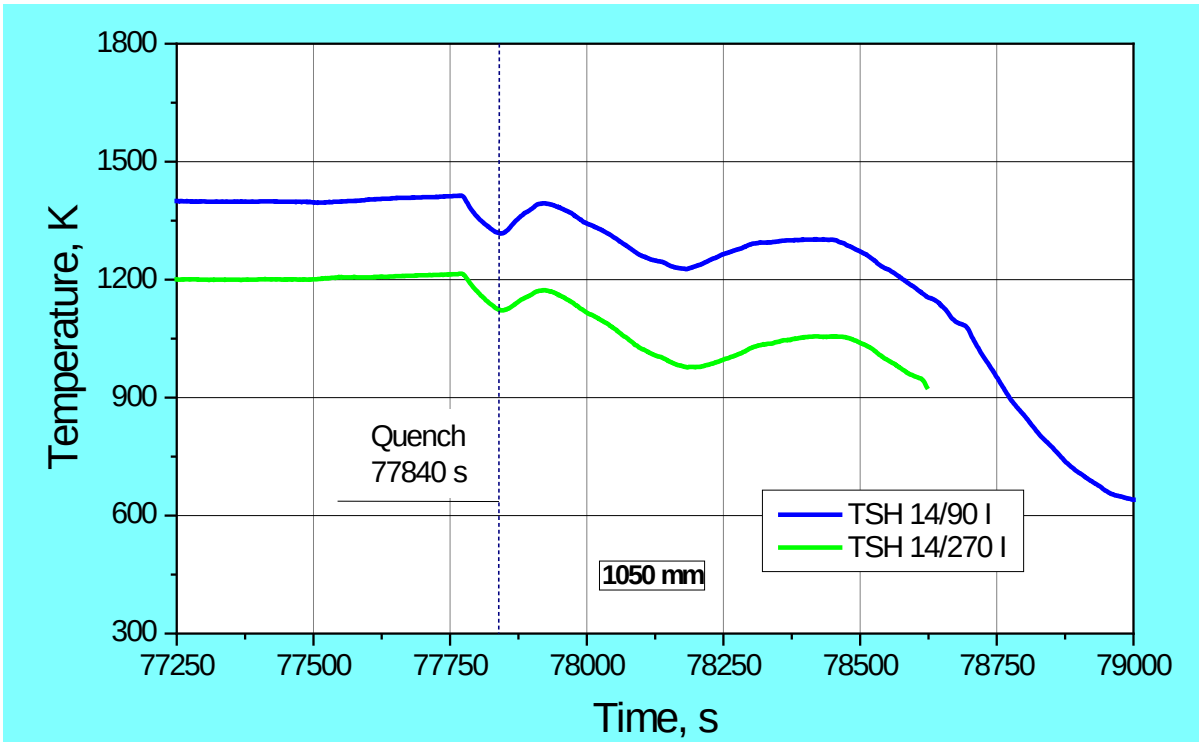

Figure 34 QUENCH-17; temperatures measured by shroud (TSH) thermocouples at 1050 mm elevation.

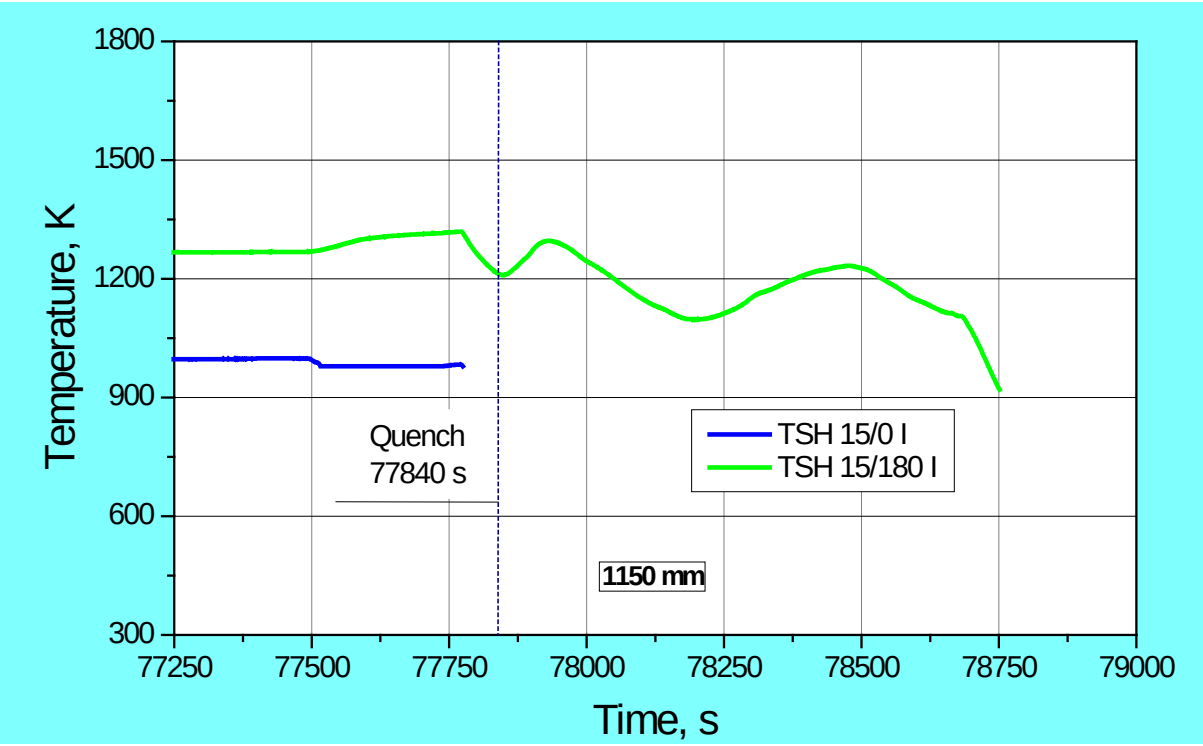

Figure 35 QUENCH-17; temperatures measured by shroud (TSH) thermocouples at 1150 mm elevation.

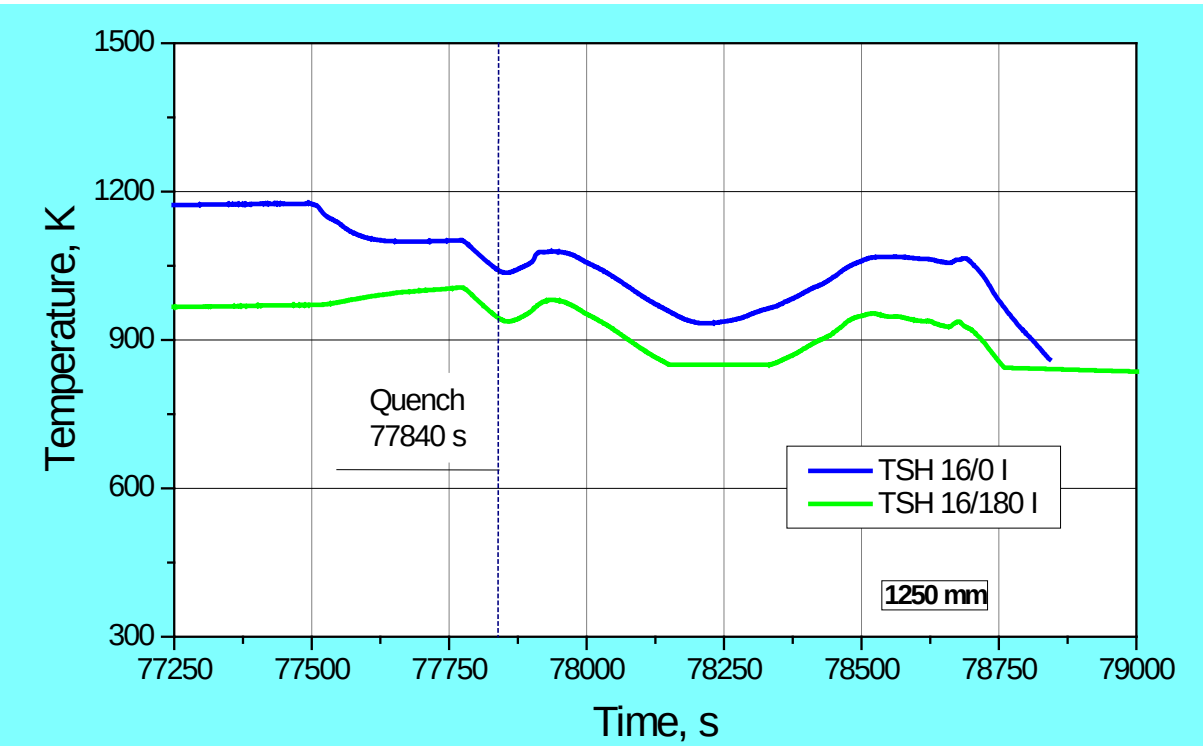

Figure 36 QUENCH-17; temperatures measured by shroud (TSH) thermocouples at 1250 mm elevation.

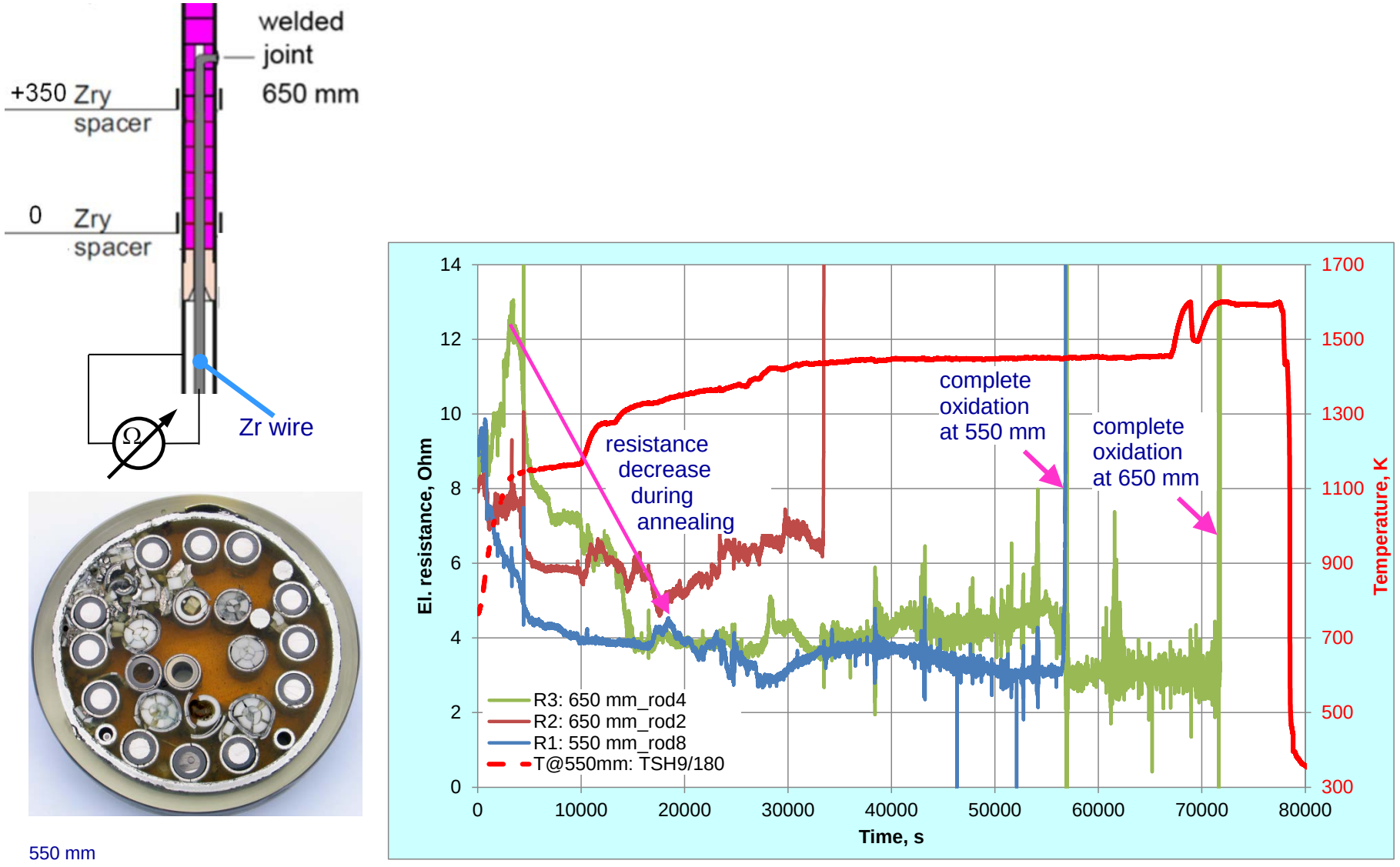

Figure 37 QUENCH-17; indication of strong cladding oxidation: abrupt increase of electrical resistance of cladding.

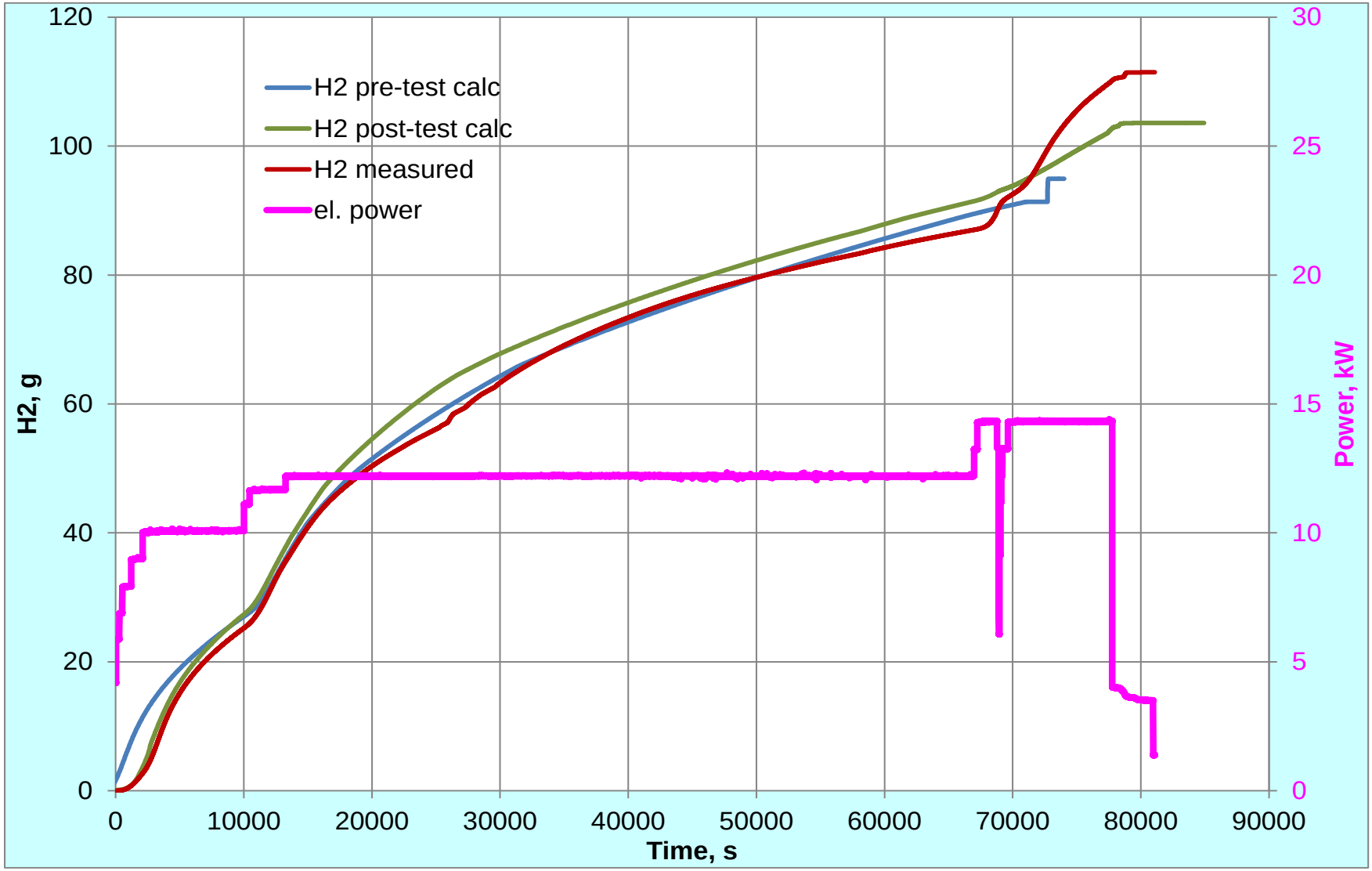

Figure 38 QUENCH-17; integral criterion of bundle oxidation progression: hydrogen release during oxidation of Zry and Hf parts.

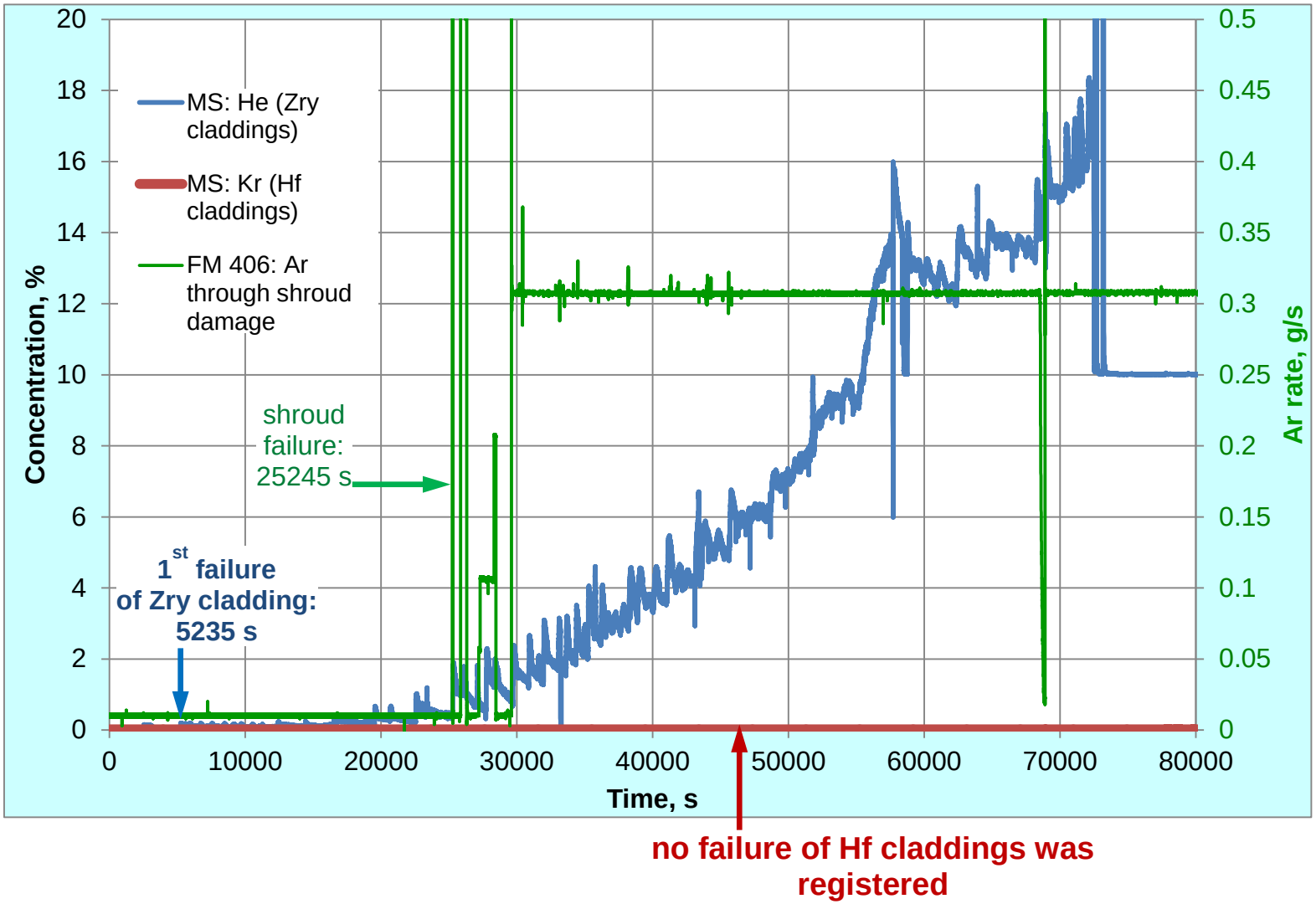

Figure 39 QUENCH-17; failures of Zry claddings and Hf shroud.

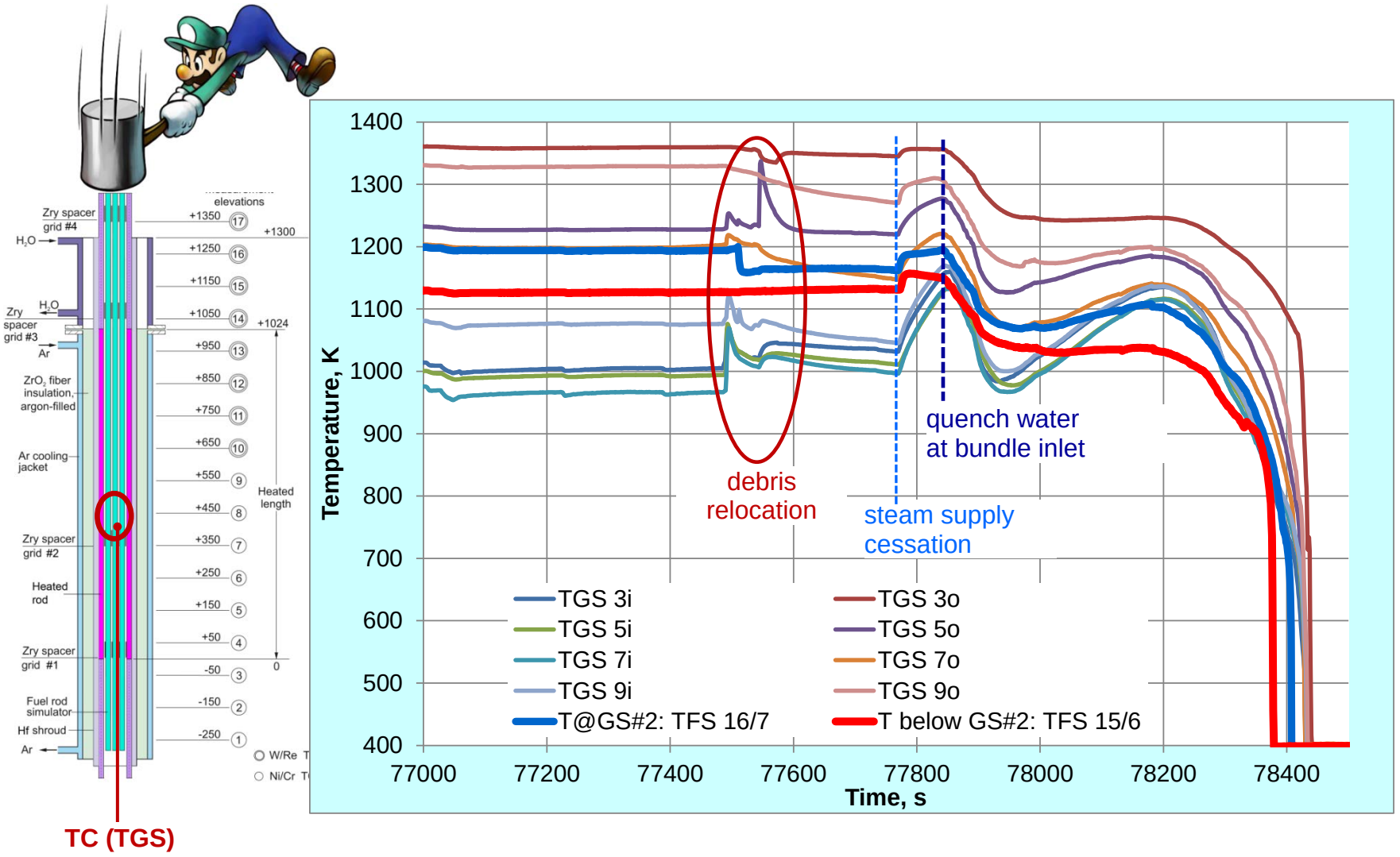

Figure 40 QUENCH-17; indication of debris relocation to GS#2 (reaction of thermocouples TGS at the top of GS#2) after mechanical impact on the bundle top.

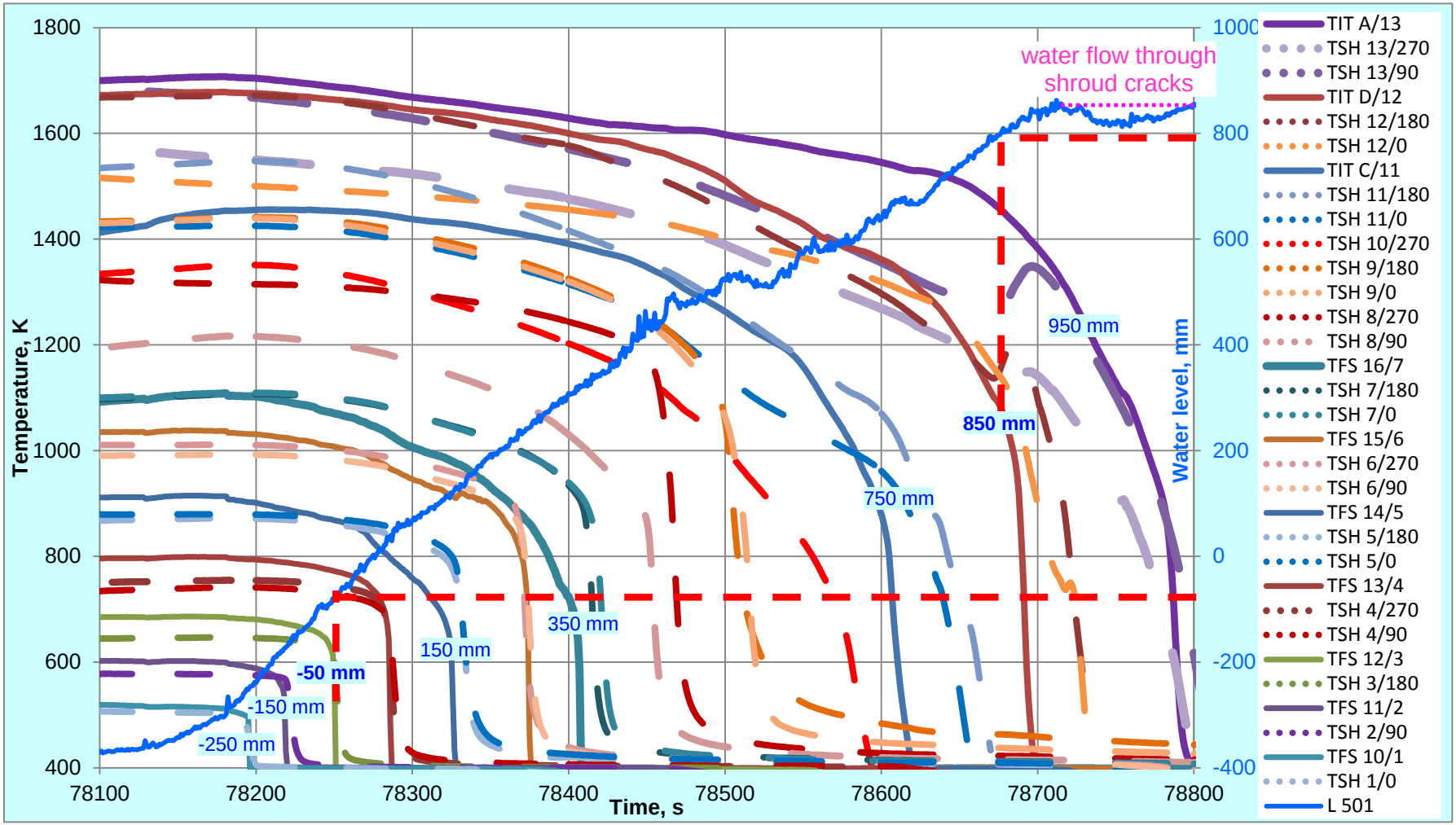

Figure 41 QUENCH-17; quench phase: collapsed water level and TC wetting by 2-phase fluid.

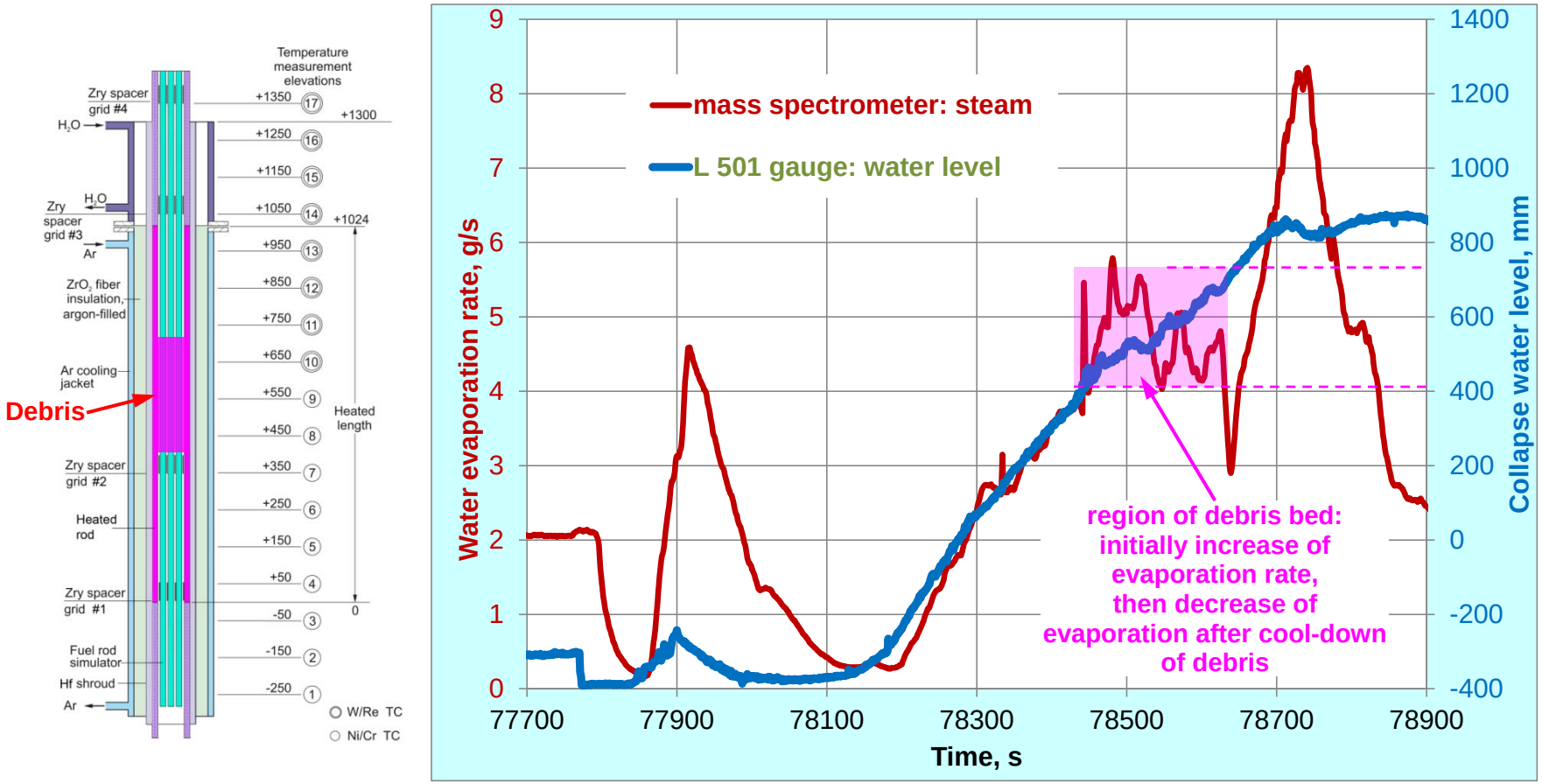

Figure 42 QUENCH-17; quench phase: water level growth and evaporation oscillations.

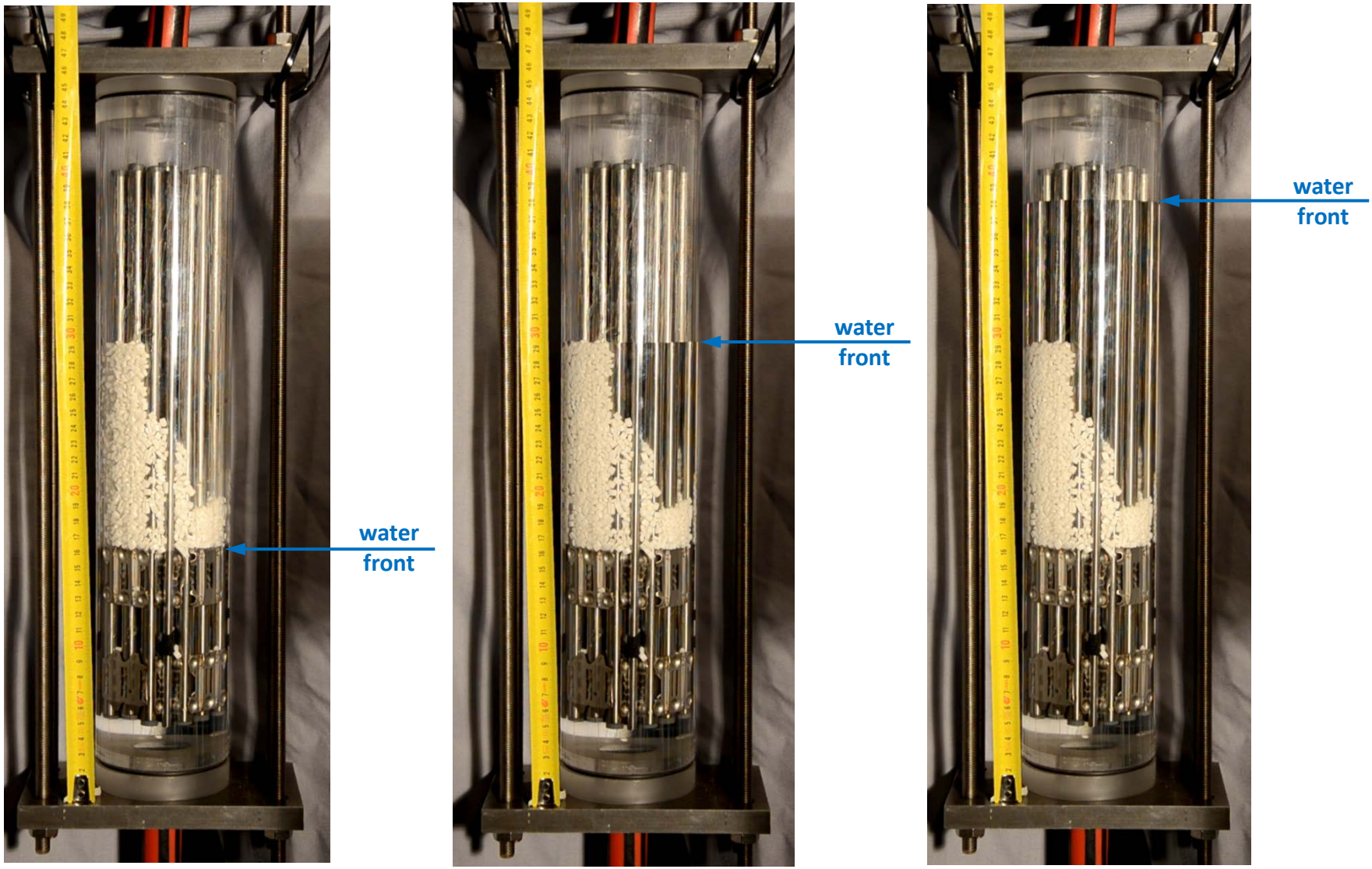

0 s | 27 s: propagation rate 4.9 mm/s | 55 s: propagation rate 3.2 mm/s

Figure 43 Check of velocity of cold water front propagation and absence of floating of pellet segments with water injection rate of 10 g/s, prototypical bundle and Plexiglas shroud with prototypical dimensions

Lower part of corner rod A

Upper part of corner rod C

Corner rod C: break location

Figure 44 QUENCH-17; different parts of Hf corner rods withdrawn from the bundle after the test

Figure 45 QUENCH-17; upper parts of unheated rods with Zry claddings

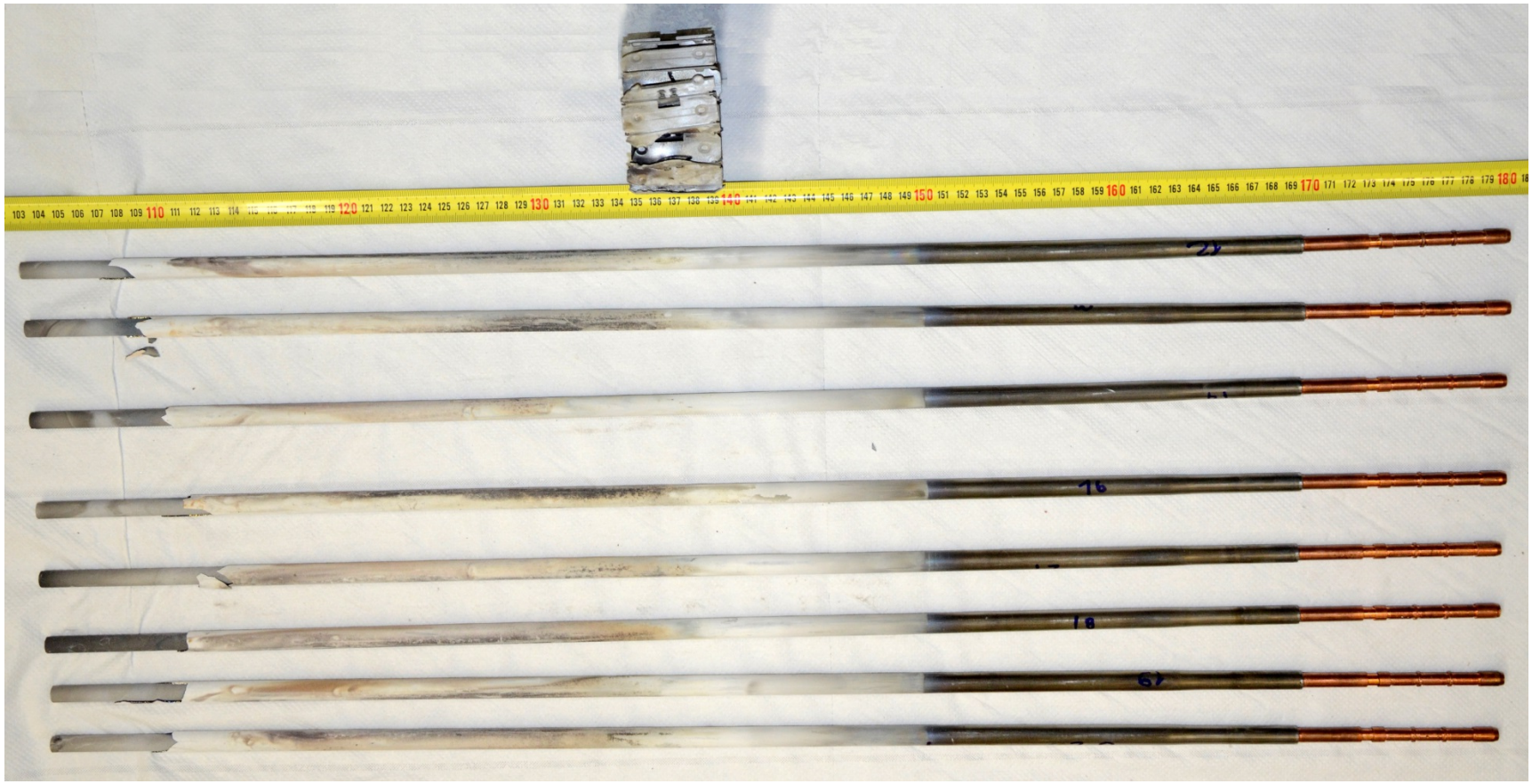

Figure 46 QUENCH-17; upper parts of heated rods with Hf claddings

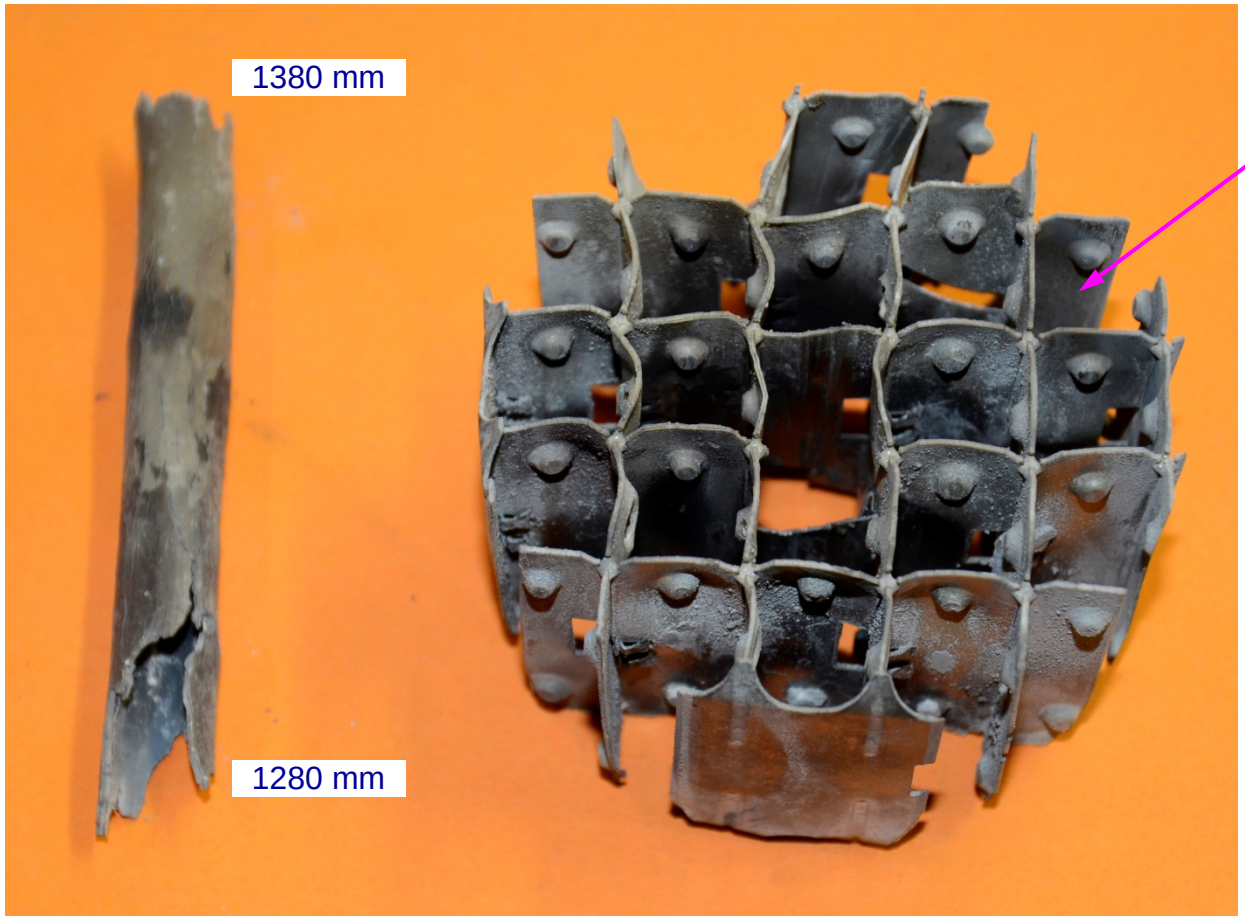

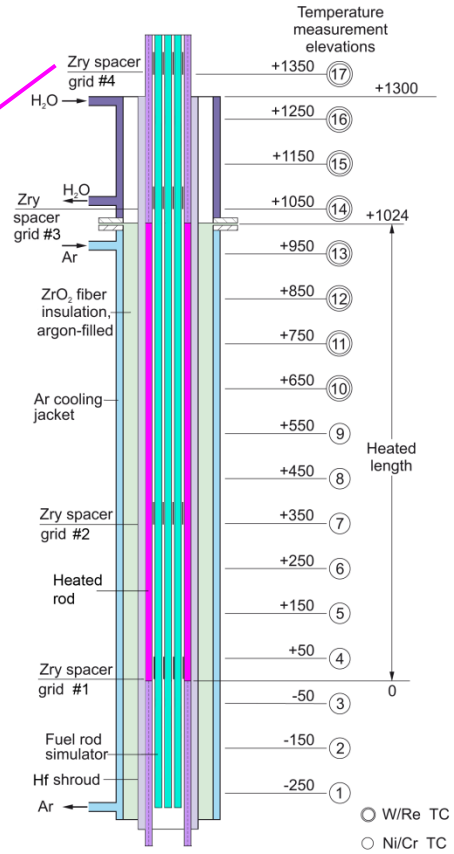

remnant of Zry clad #8:
significantly oxidized

Zry-4 GS #4 (highest elevation):
completely oxidized

Figure 47 QUENCH-17; withdrawn grid spacer #4 (1350 - 1390 mm) and remnant of cladding

1550 mm: oxidation of 12 Hf claddings under ceramic plate bottom (1500 mm) and top view of GS #4

1410 mm: view through the central cell of GS #4;
remnant of Zry cladding #8

1200 mm: pellet segments inside Zry cladding of rod #8

1150 mm: pellet segments inside Zry claddings and at the top of GS #3; through going cracks inside strong oxidized cladding #8; intact oxide of Hf claddings

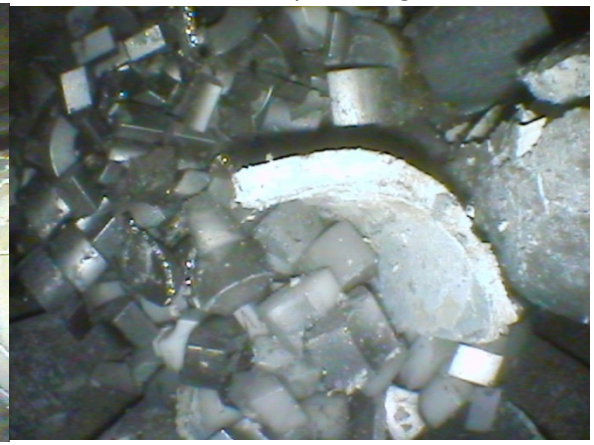

1100 mm: pellet and Zry cladding remnants at the top of GS #3

1100 mm: view of oxidized Zry claddings after partial removal of debris

Figure 48 QUENCH-17; videoscope observation (top view) of the bundle after removal of upper parts of 9 central unheated rods with Zry claddings and before removal of the Zry grid spacer GS #4.

1180 mm: overview of broken central rods with Zry claddings and almost intact (partial HfO_2 spalling) peripheral heated rods with Hf claddings

1120 mm: top of broken rod #5

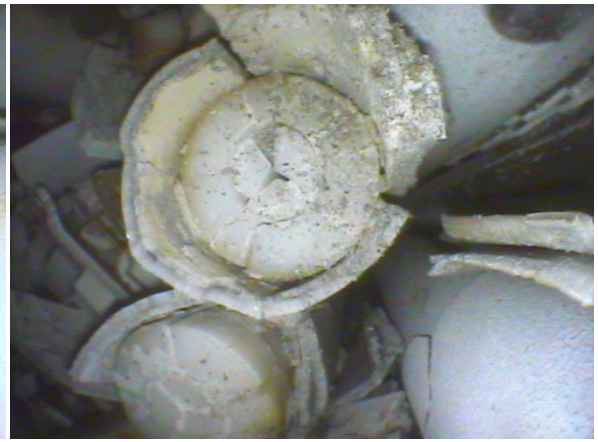

1100 mm: top of broken rods #3 (upper) and #4

1180 mm after strong mechanical intervention (shaking): spalling of oxide layers and emptying of rod #6

990 mm: view through the emptied rod #6

910 mm: view through rod #6, blockage of cooling channel

Figure 49 QUENCH-17; videoscope observation (top view) of the bundle after removal of upper parts of 9 central unheated rods with Zry claddings and Zry grid spacer GS #4.

950 mm: intact pellet segment stack of rod #8

920 mm: relocated pellet segments pellet segment stack of rod #7

910 mm: blockage between Zry and Hf claddings

Figure 50 QUENCH-17; videoscope observation (side view objective) of bundle elements below grid spacer GS #3.

Figure 51 QUENCH-17; post-test view of shroud.

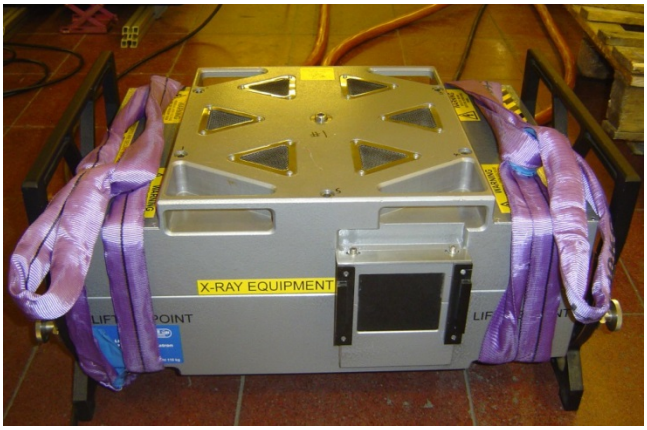

Betatron-7 with 5 MeV

QUENCH-17 embedded bundle inserted into the steel holder

Figure 52 High energy X-ray tomography at BAM.

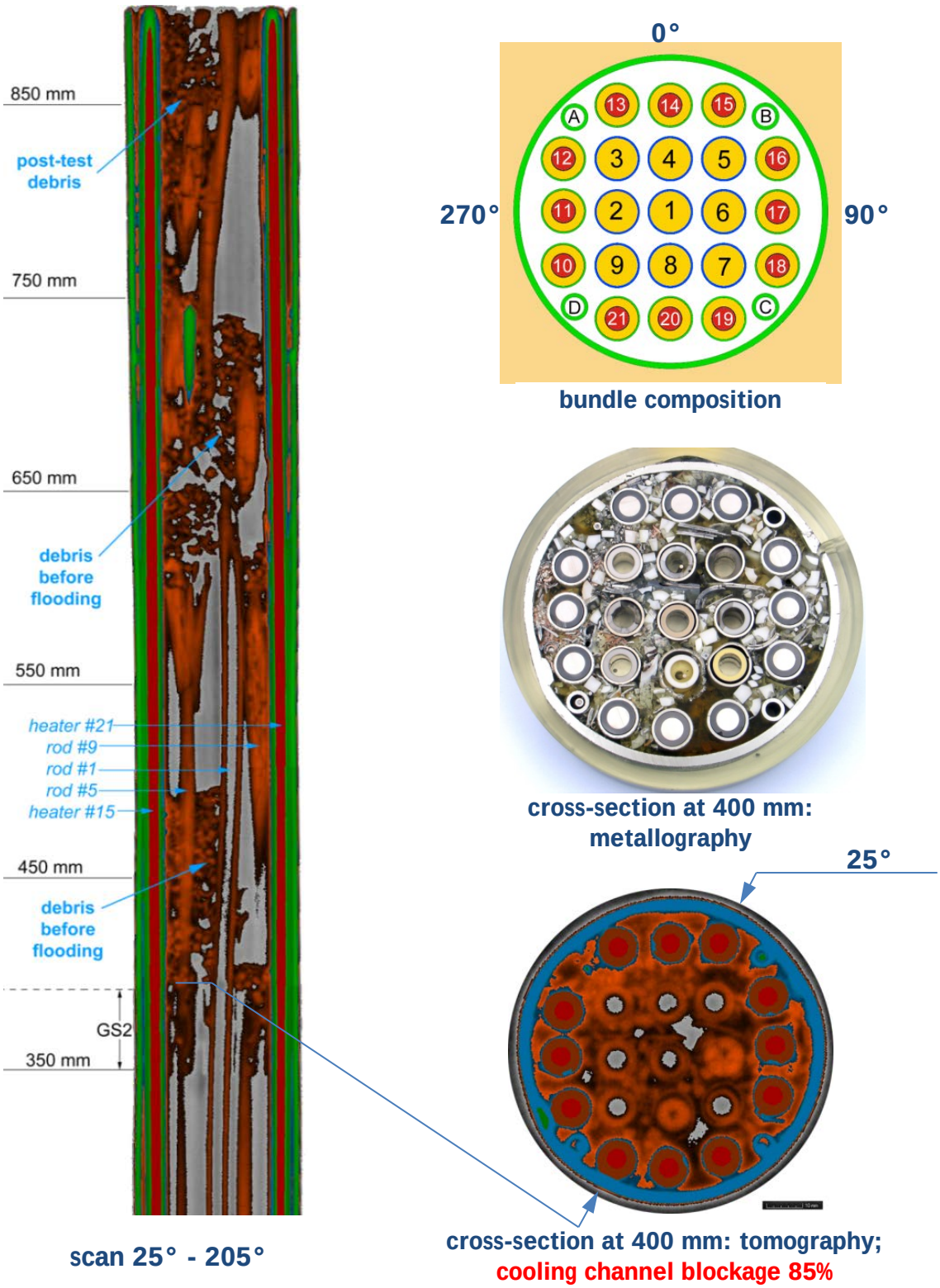

Figure 53 QUENCH-17; X-ray tomography: longitudinal section (left) and top view of cross section at 400 mm (right); comparison with corresponding metallographic view

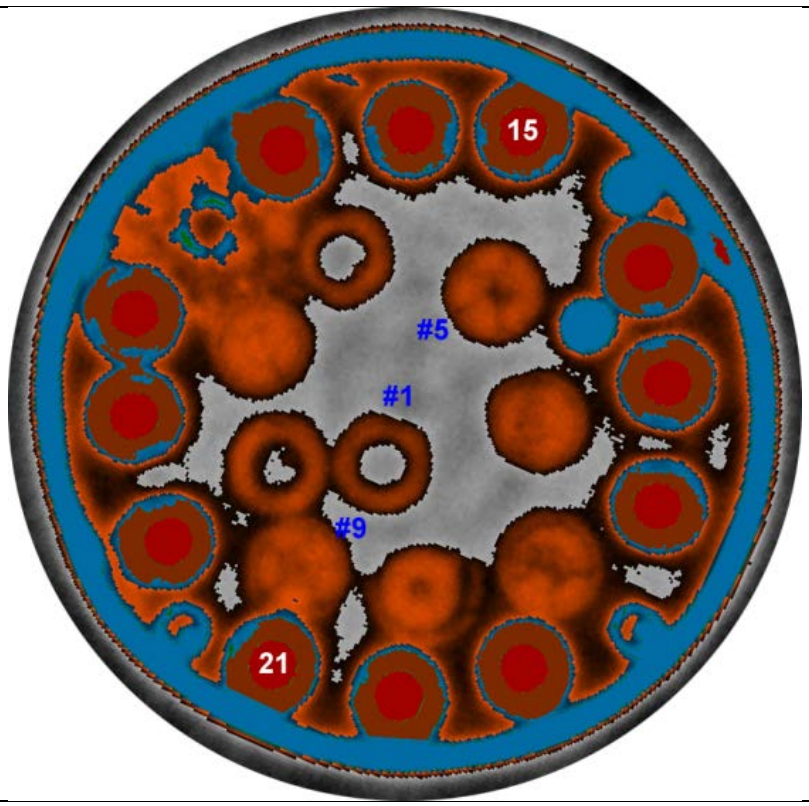

518 mm: only local blockage by relocated debris

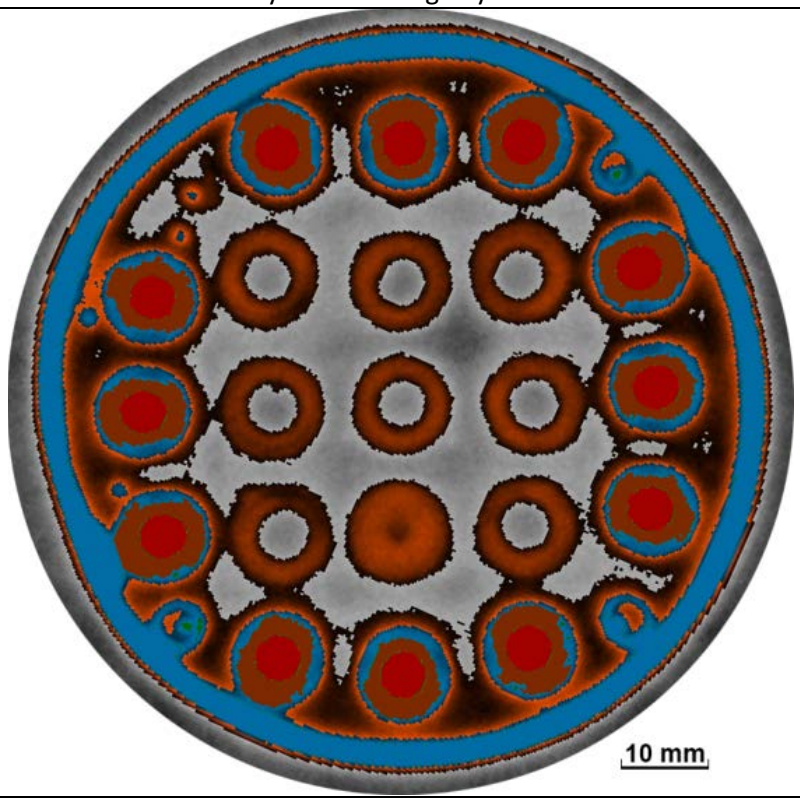

350 mm: no relocated debris under grid spacer GS2

Figure 54 QUENCH-17; results of tomography: negligible cooling channel blockage away from the grid spacer

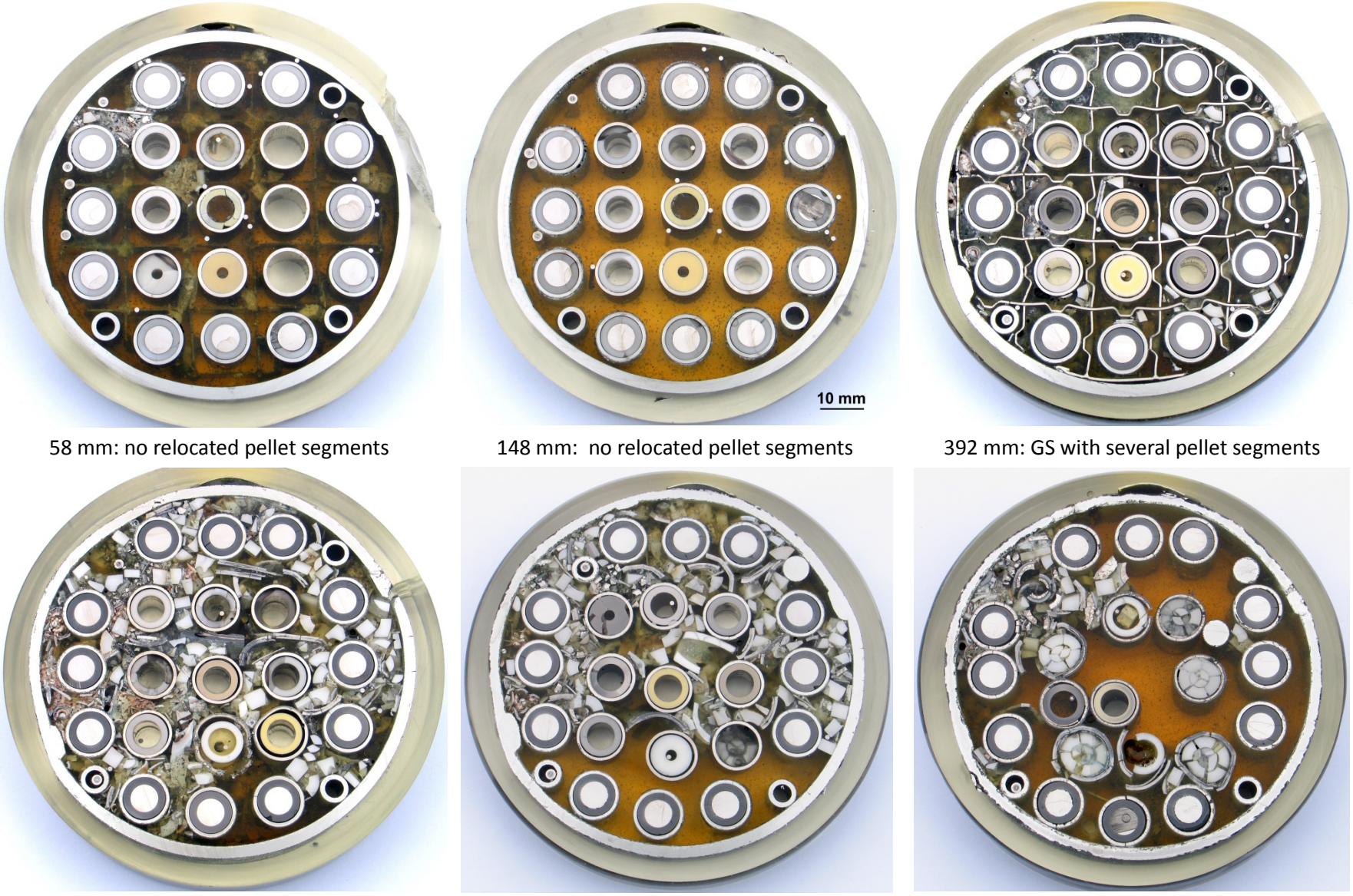

58 mm: no relocated pellet segments

148 mm: no relocated pellet segments

392 mm: GS with several pellet segments

411 mm: relocated pellet segments at the top of the grid spacer GS#2

449 mm; last cross section without segmented pellets inside claddings

549 mm; rods # 2, #4, #8 without internal segmented pellets (see Fig. 37)

Figure 55 QUENCH-17; lower bundle cross sections (as polished), top view.

633 mm

649 mm

749 mm: top of the axial region with debris relocated before reflood

850 mm: debris relocated after the test

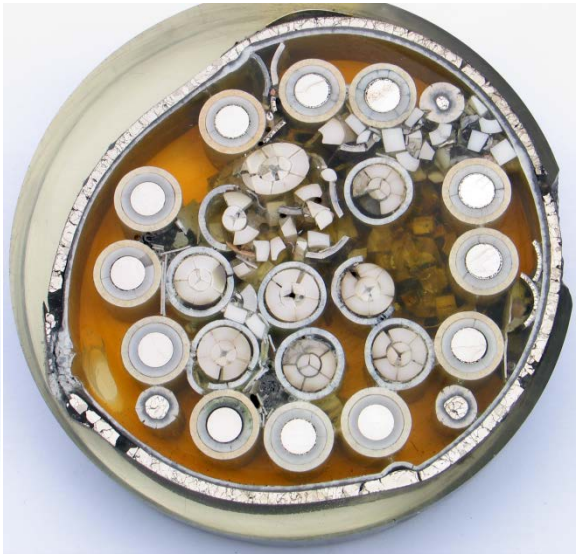

950 mm

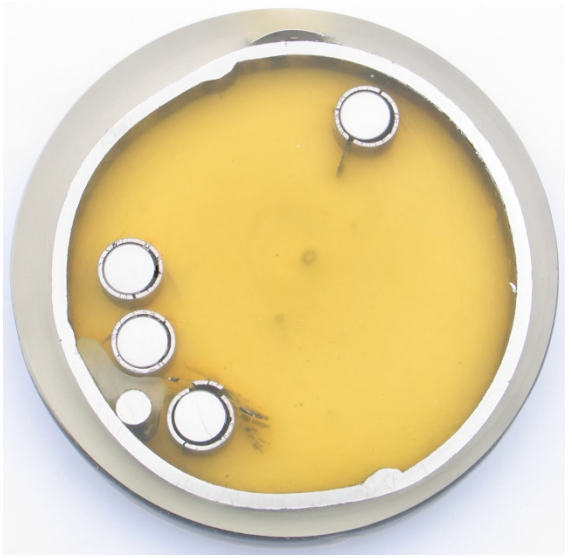

1104 mm

Figure 56 QUENCH-17; upper bundle cross sections (as polished), top view.

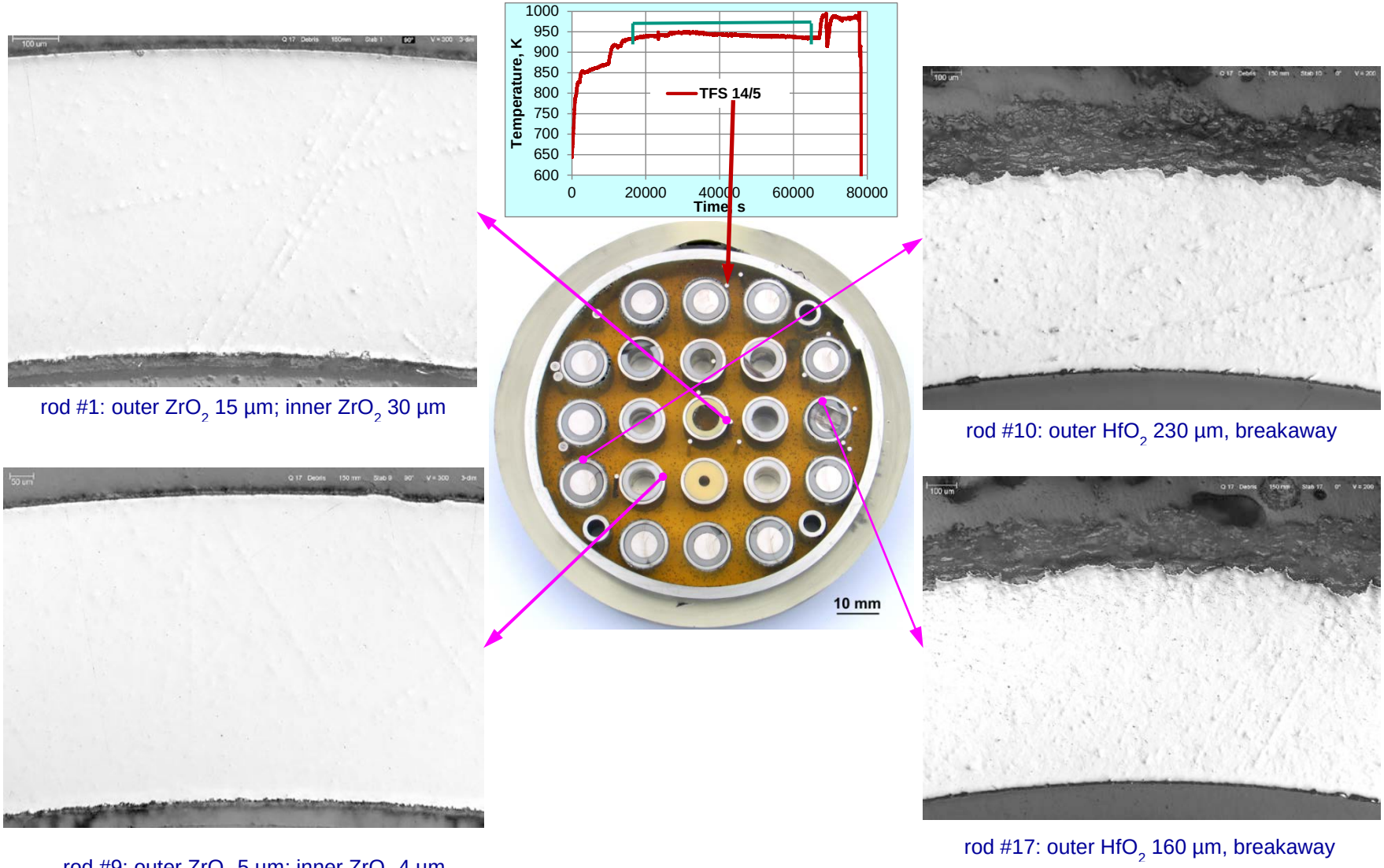

Figure 57 QUENCH-17; post-test structure of Zry and Hf claddings at 150 mm with continuous peak cladding temperature T=TFS 14/5=940 K

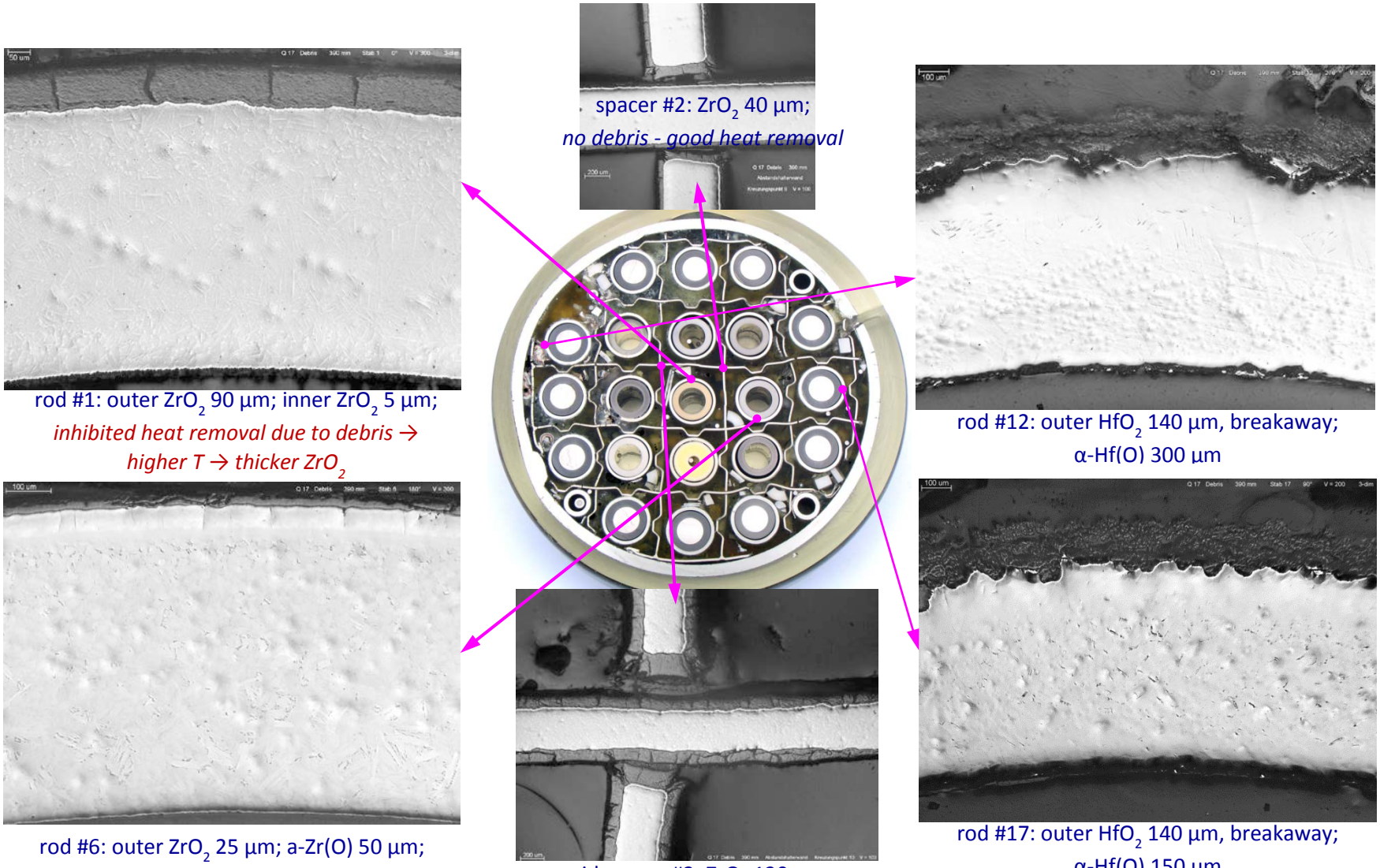

Figure 58 QUENCH-17; post-test structure of Zry and Hf claddings at 390 mm with continuous peak cladding temperature T=1200 K: local effects due to debris.

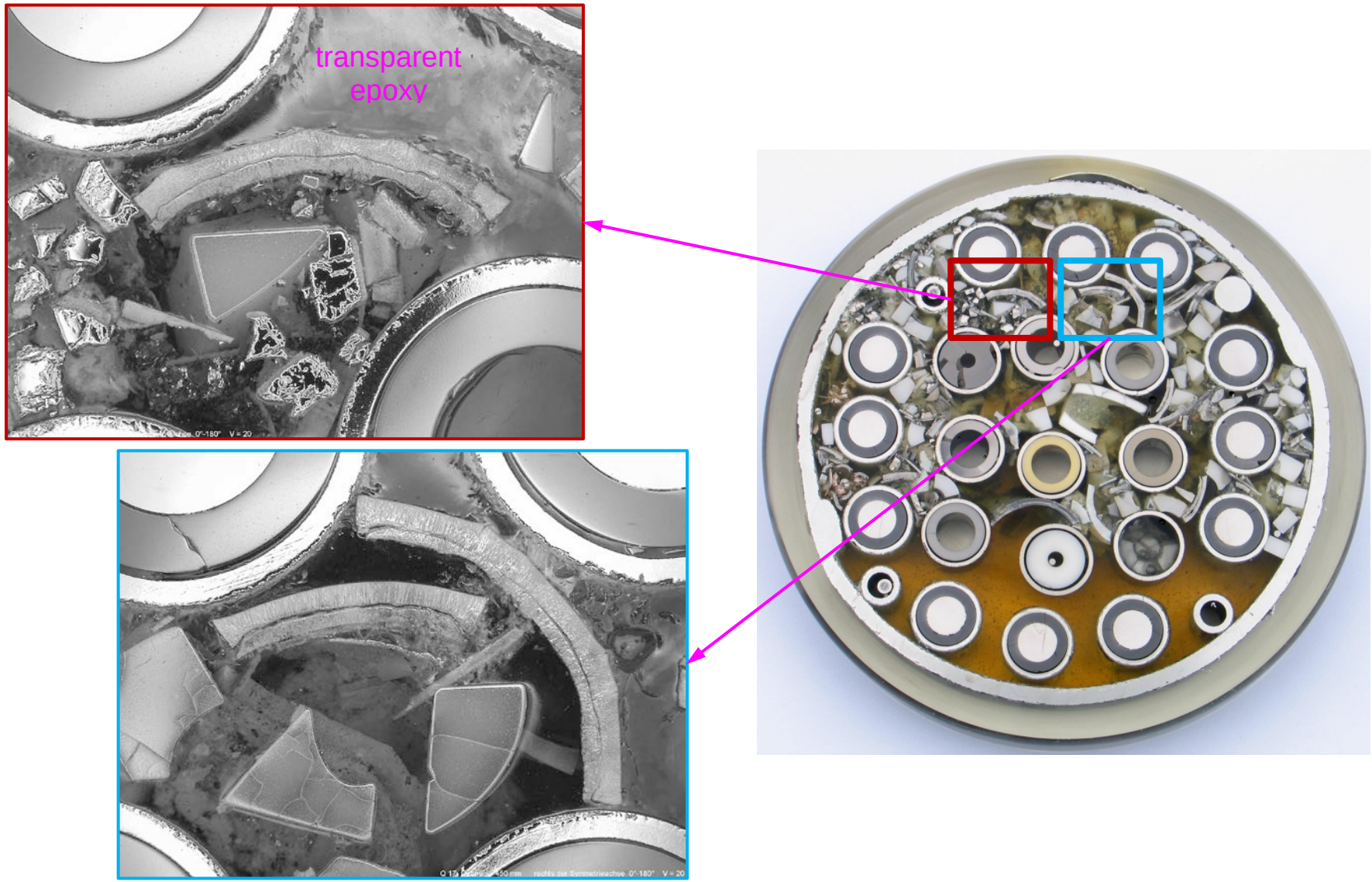

Figure 59 QUENCH-17; debris regions at elevation 450 mm

rod #3 (similar with #4 - #6):
outer ZrO_2 25 µm; α-Zr(O) 300 µm;
inner ZrO_2 25 µm; α-Zr(O) 40 µm

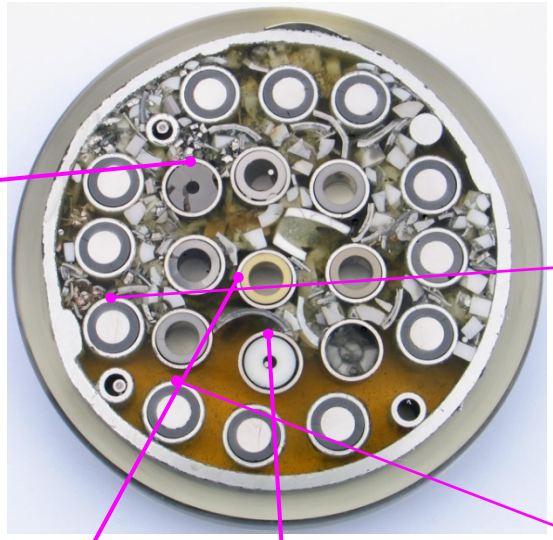

rod #10: outer HfO_2 130 µm, breakaway
α-Hf(O) 350 µm

rod #1: outer ZrO_2 30 µm; α-Zr(O) 90 µm;
inhibited heat removal due to debris → higher T → thicker ZrO_2

rod #8:
outer ZrO_2 100 µm; α-Zr(O) 70 µm;
inner ZrO_2 30 µm; α-Zr(O) 80 µm

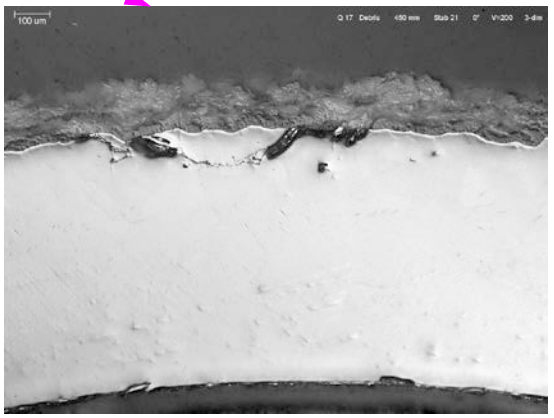

rod #21: outer HfO_2 120 µm, breakaway
α-Hf(O) 330 µm

Figure 60 QUENCH-17; post-test structure of Zry and Hf claddings at 450 mm with continuous peak cladding temperature T=TFS 17/8 =1250 K: local effects due to debris.

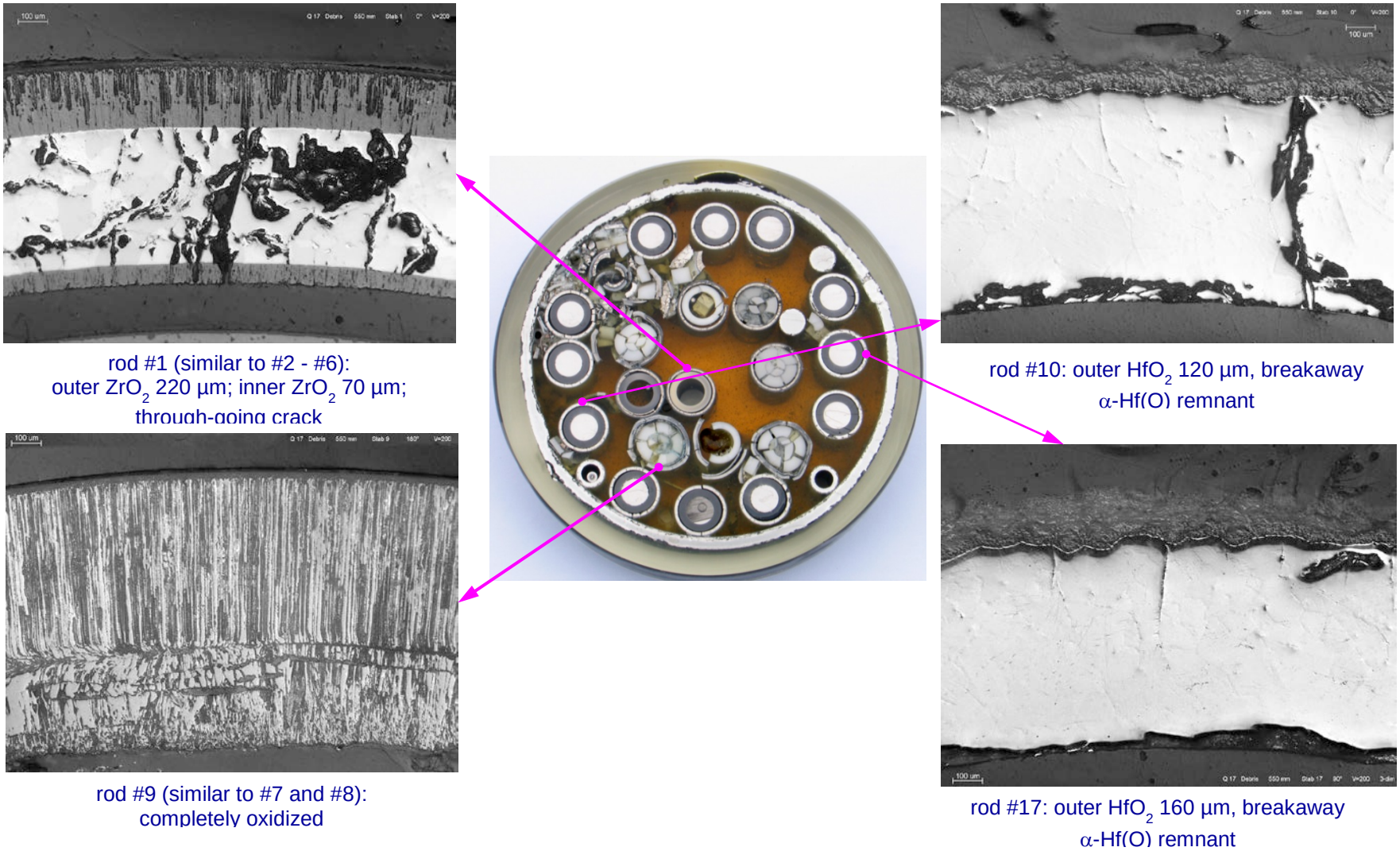

Figure 61 QUENCH-17; post-test structure of Zry and Hf claddings at 550 mm with continuous peak cladding temperature T=TFS 18/9 =1400 K: local effects due to debris.

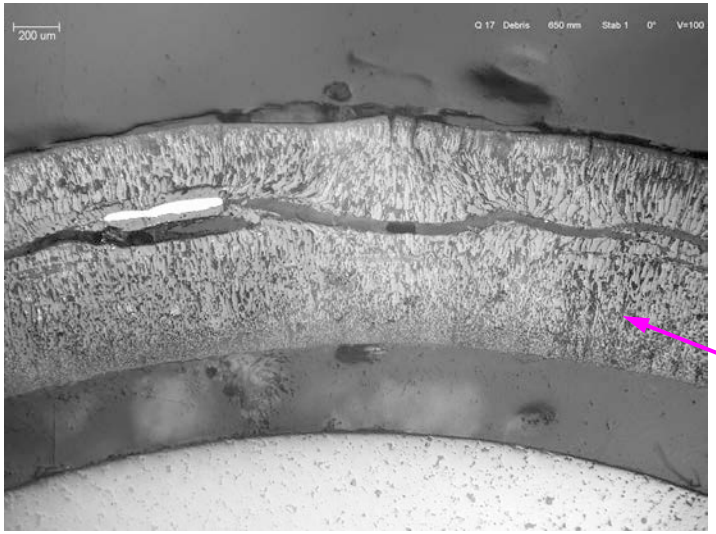

completely oxidized rod #1
(similar to rods #2 - #9)

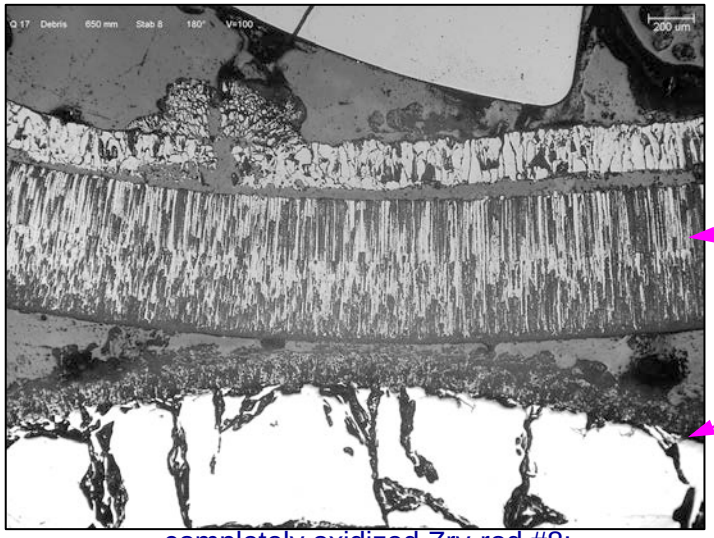

completely oxidized Zry-rod #8;
Hf-rod #20: HfO_2 200 µm; α-Hf(O) 650 µm

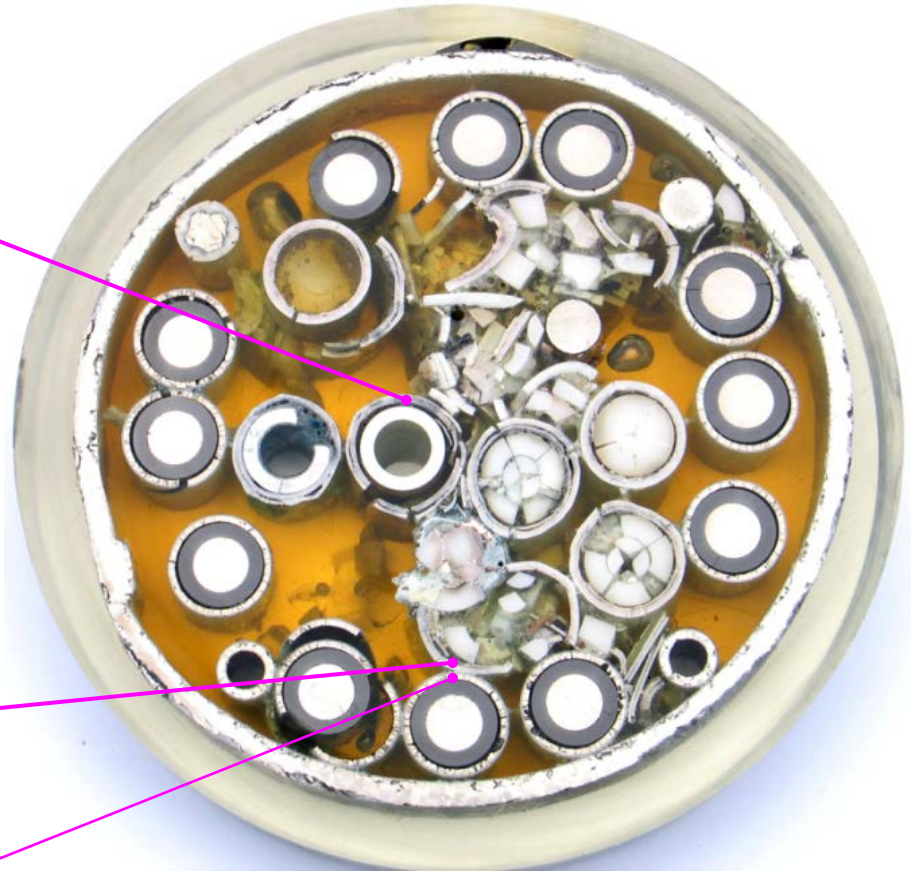

3 destroyed Zry-rods: #4, #5, #9

Figure 62 QUENCH-17; post-test structure of Zry and Hf claddings at 650 mm with continuous peak cladding temperature T=TIT D/12 =1550 K.

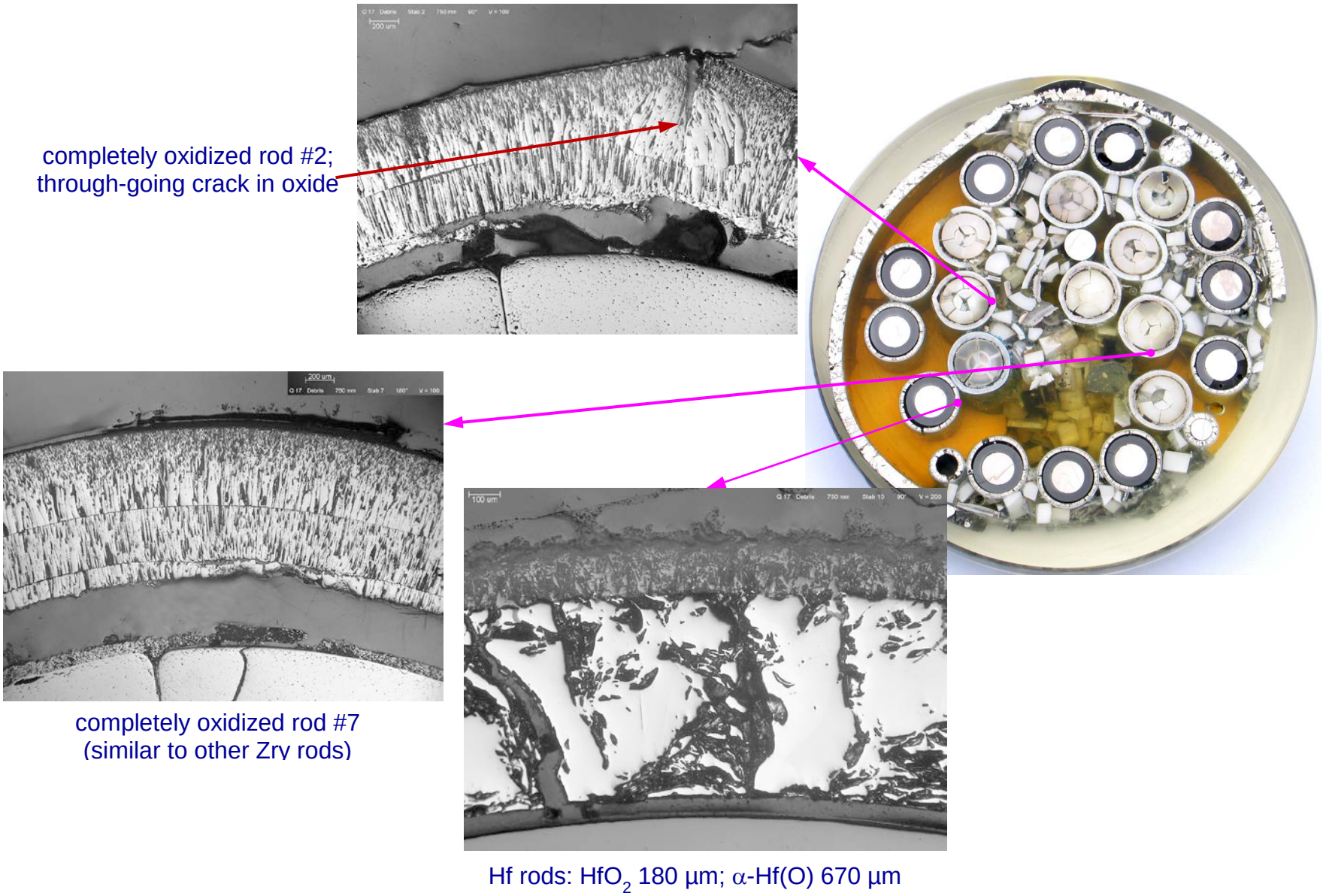

Figure 63 QUENCH-17; post-test structure of Zry and Hf claddings at 750 mm with continuous peak cladding temperature T=TIT C/11 =1700 K.

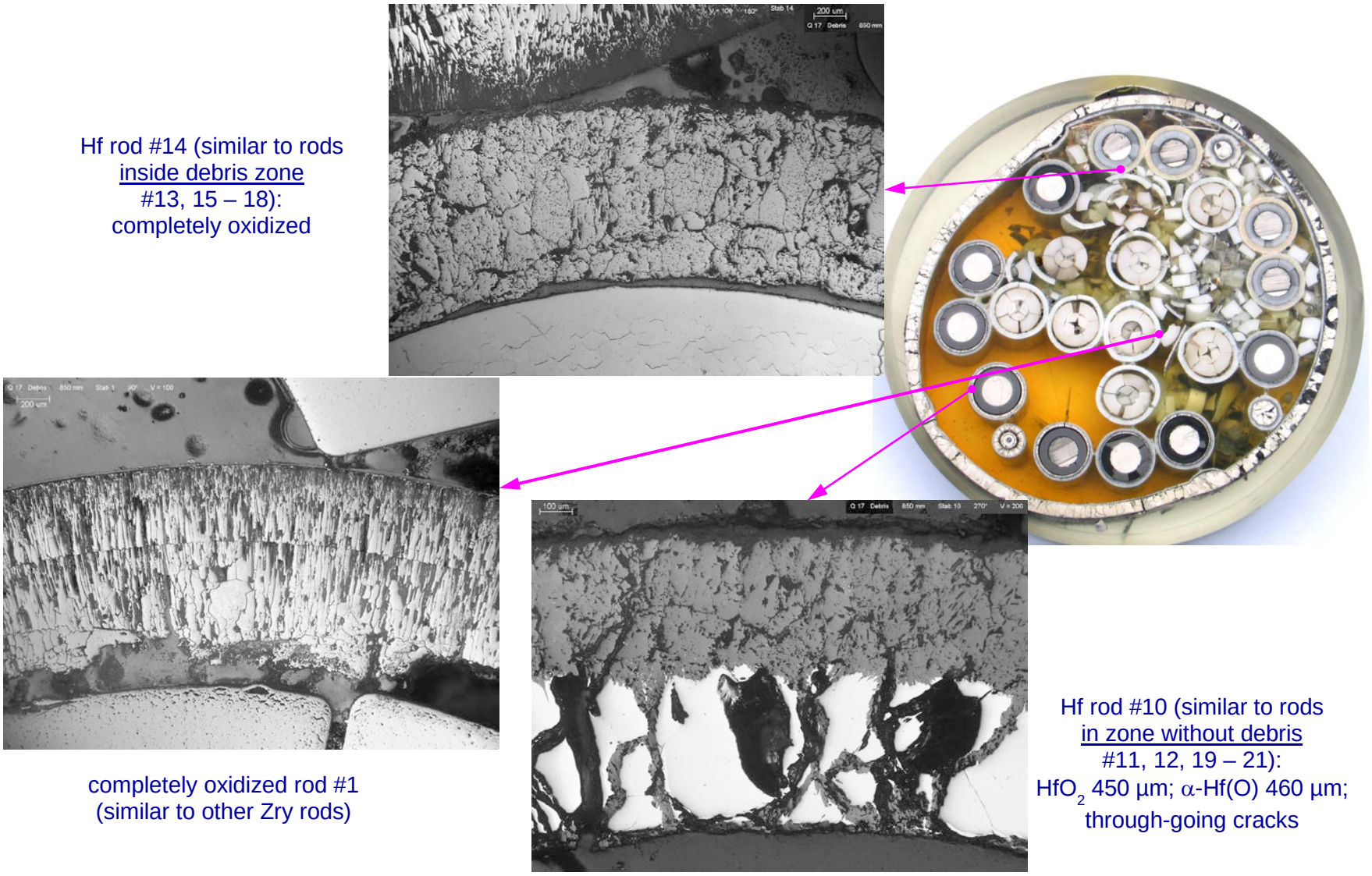

Figure 64 QUENCH-17; post-test structure of Zry and Hf claddings at 850 mm with continuous peak cladding temperature T=TIT D/12 =1750 K.

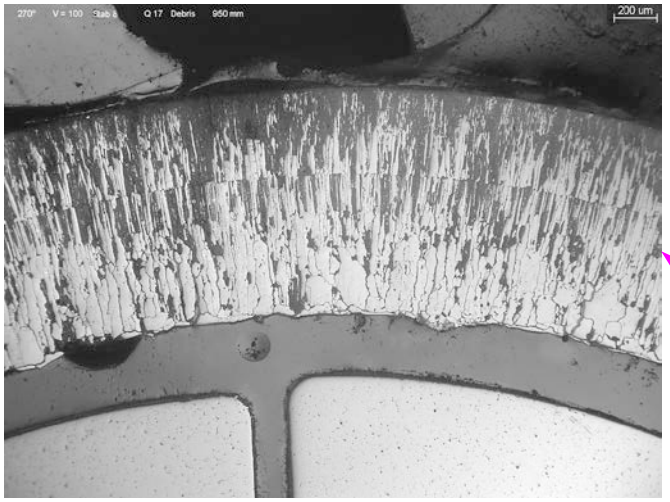

all Zry clads are completely oxidized

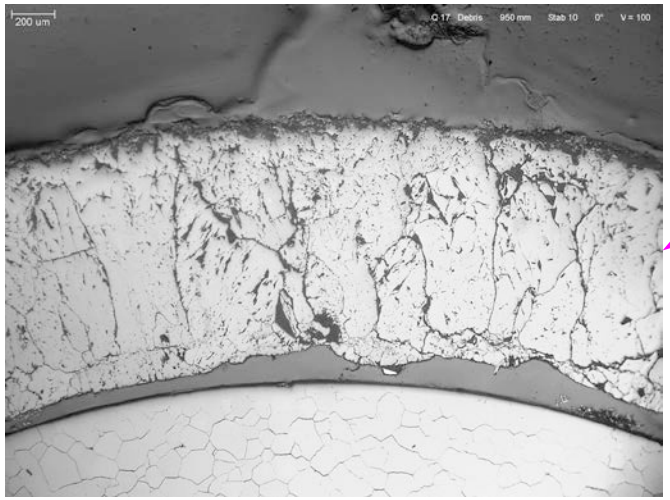

all Hf clads are completely oxidized

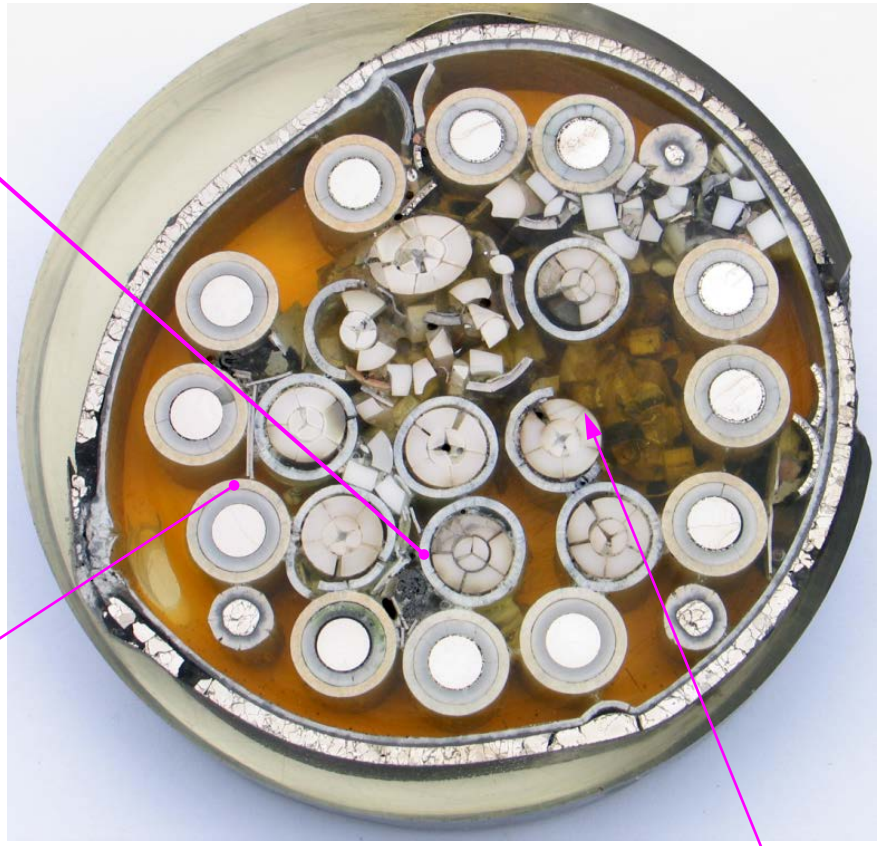

3 partially destroyed Zry clads: #3, #4, #6

Figure 65 QUENCH-17; post-test structure of Zry and Hf claddings at 950 mm with continuous peak cladding temperature T=TIT A/13 =1700 K.

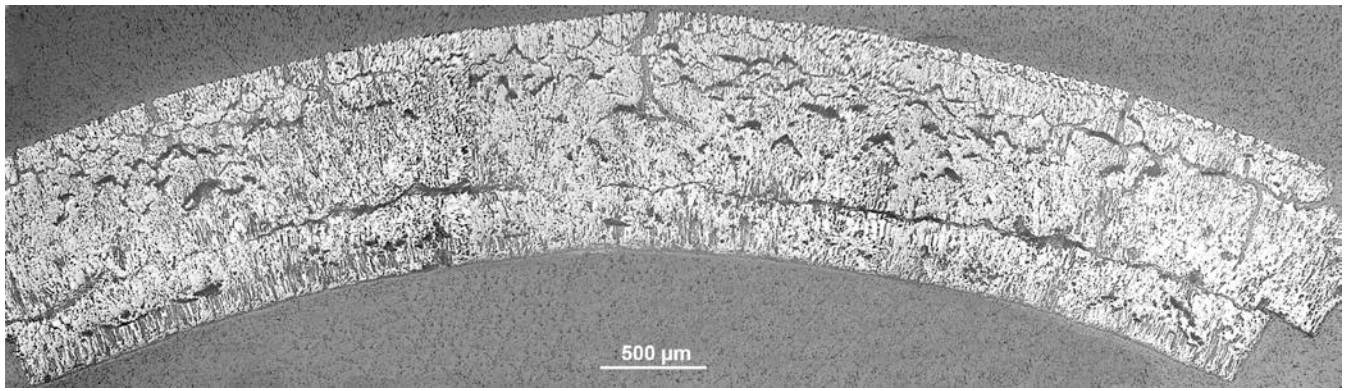

completely oxidized Zry cladding

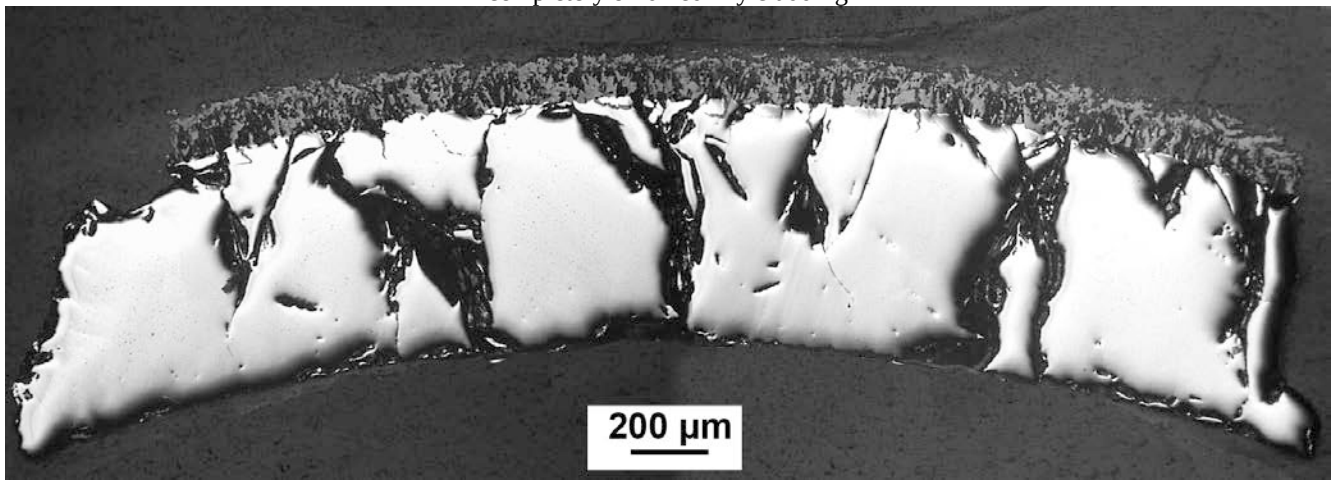

partially oxidized Hf cladding: HfO_2 140 µm; a-Hf(O) remnant 630 µm

Figure 66 QUENCH-17; post-test structure of Zry and Hf claddings at 1050 mm.

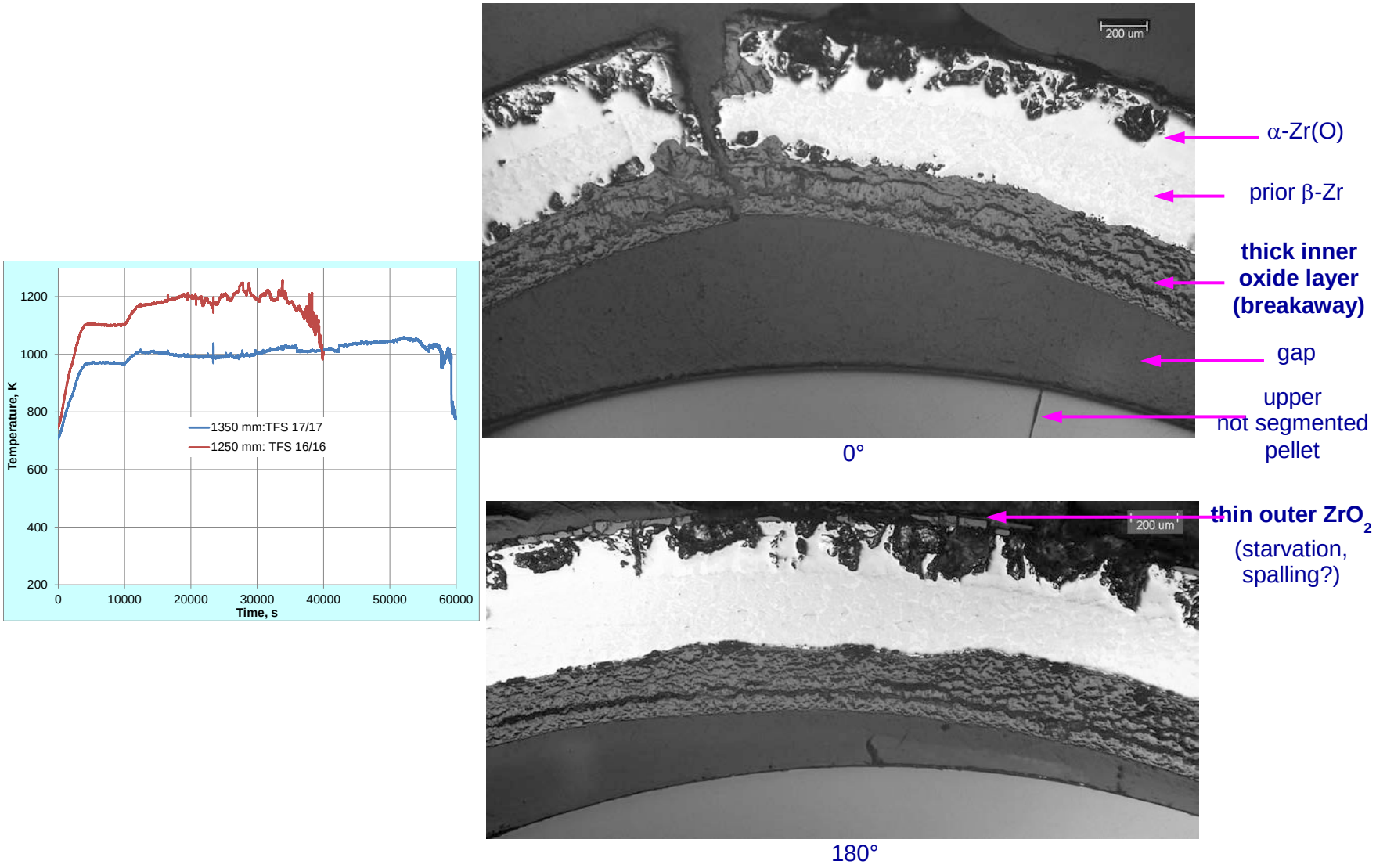

Figure 67 QUENCH-17; structure of oxidized Zry cladding remnant at 1328 mm, T ≈ 1000 K.

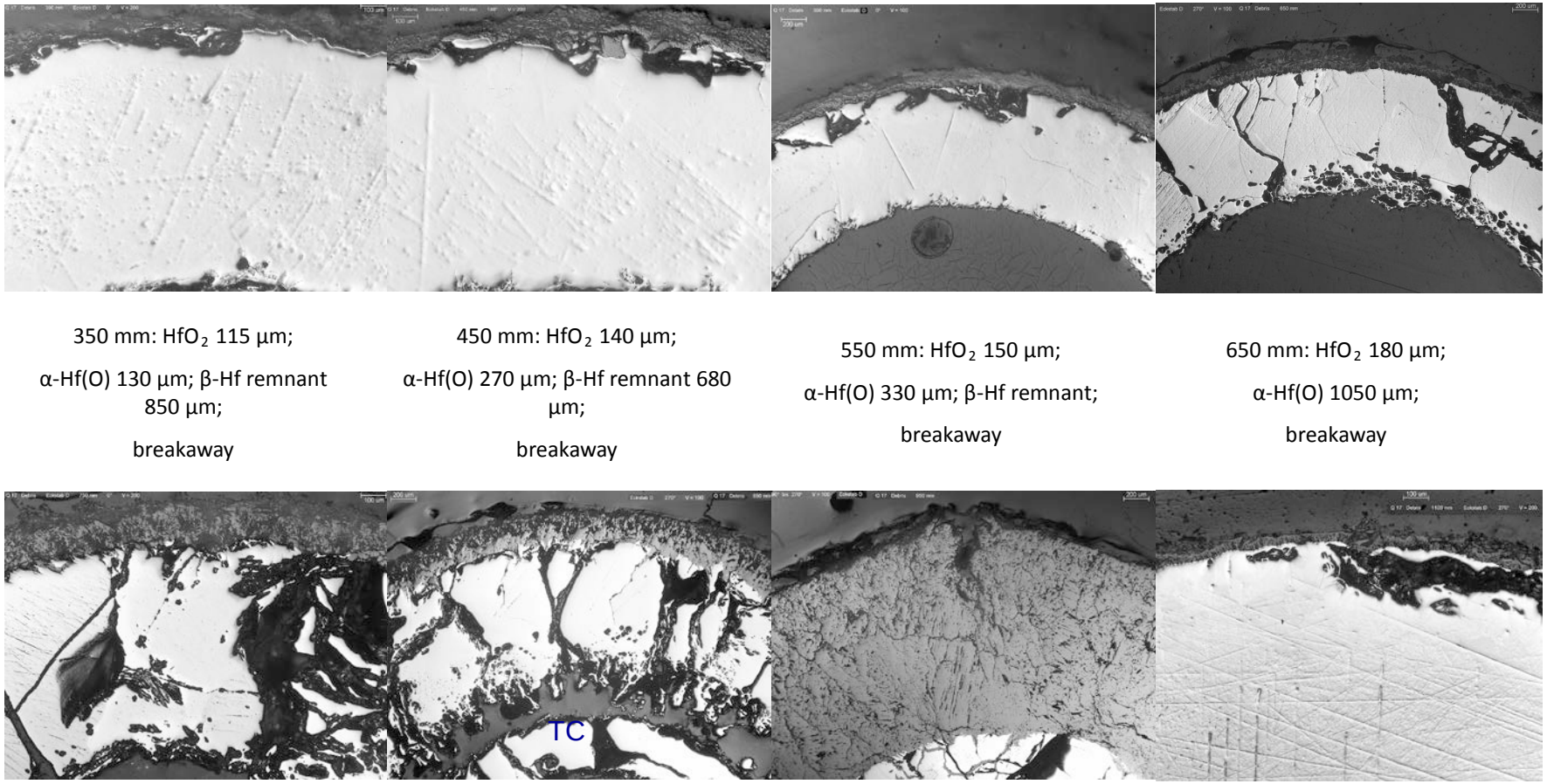

350 mm: HfO_2 115 µm;
α-Hf(O) 130 µm; β-Hf remnant 850 µm;
breakaway

450 mm: HfO_2 140 µm;
α-Hf(O) 270 µm; β-Hf remnant 680 µm;
breakaway

550 mm: HfO_2 150 µm;
α-Hf(O) 330 µm; β-Hf remnant;
breakaway

650 mm: HfO_2 180 µm;
α-Hf(O) 1050 µm;
breakaway

750 mm: HfO_2 160 µm;
α-Hf(O) 1030 µm;
no breakaway

850 mm: HfO_2 270 µm;
α-Hf(O) 1120 µm;
no breakaway

950 mm: HfO_2 1550 µm;
no breakaway

1100 mm: HfO_2 70 µm;
α -Hf(O) 250 µm;
breakaway

Figure 68 QUENCH-17; oxidation of Hf corner rod D at different elevations.

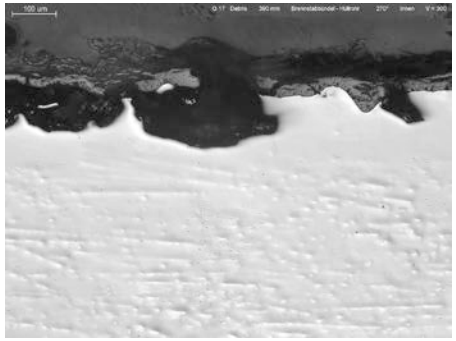

390 mm: HfO_2 70 µm;
α-Hf(O) 140 µm

450 mm: HfO_2 100 µm;
α-Hf(O) 330 µm

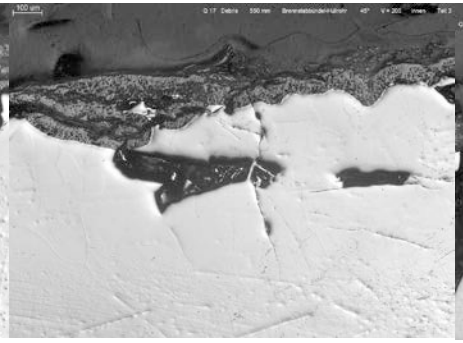

550 mm: HfO_2 110 µm;
α-Hf(O) 450 µm;
breakaway

650 mm: HfO_2 190 µm;
breakaway

750 mm: HfO_2 90 µm;
no breakaway

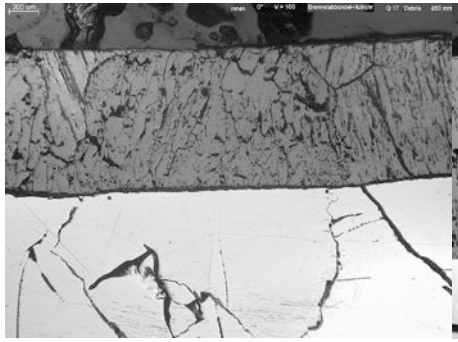

850 mm: HfO_2 950 µm;
no breakaway

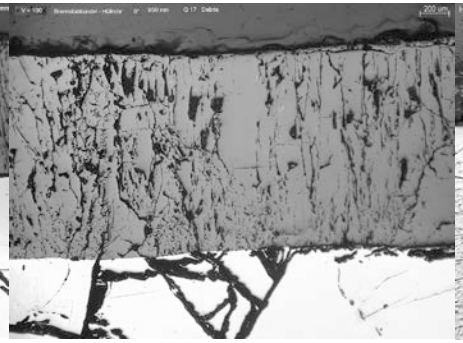

950 mm: HfO_2 1200 µm;
no breakaway

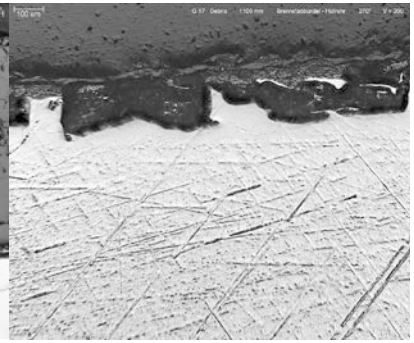

1100 mm: HfO_2 80 µm;
α-Hf(O) 170 µm;
breakaway

Figure 69 QUENCH-17; oxidation of Hf shroud at different elevations.

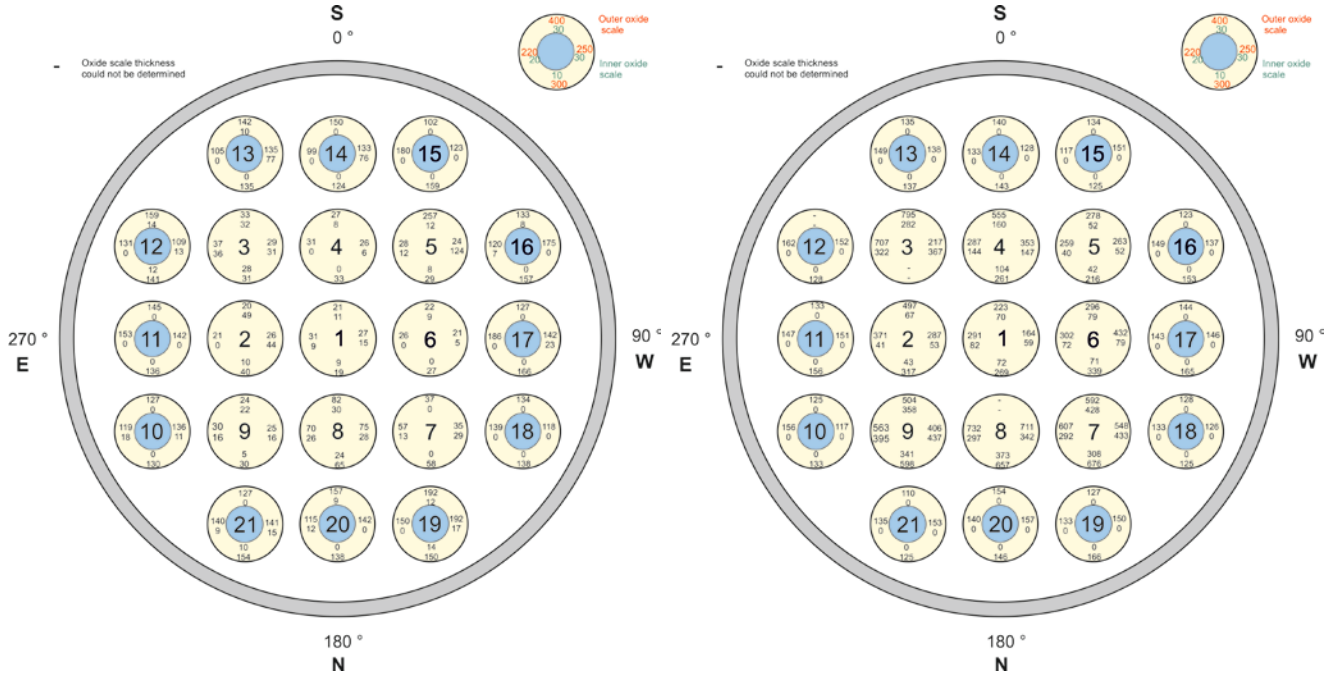

450 mm

550 mm

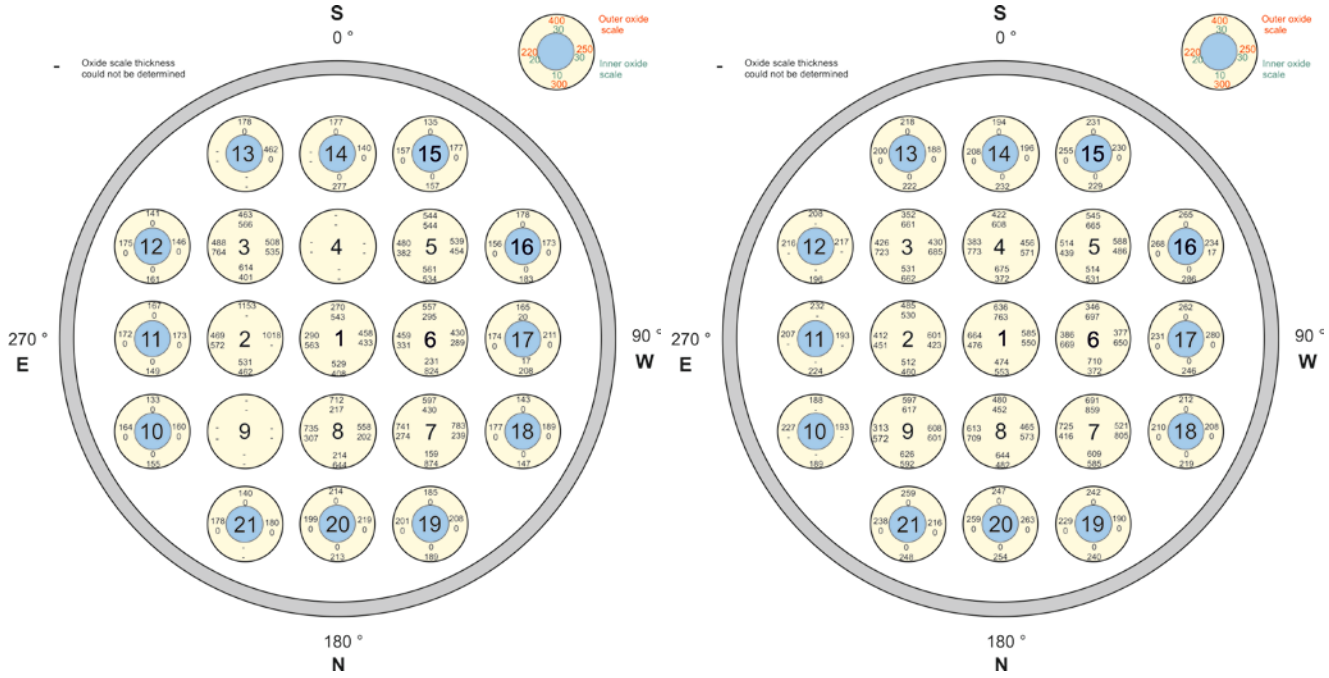

650 mm

750 mm

Figure 70 QUENCH-17; thicknesses of oxide layers for Zry-4 (nine inner rods) and Hf claddings (twelve outer rods).

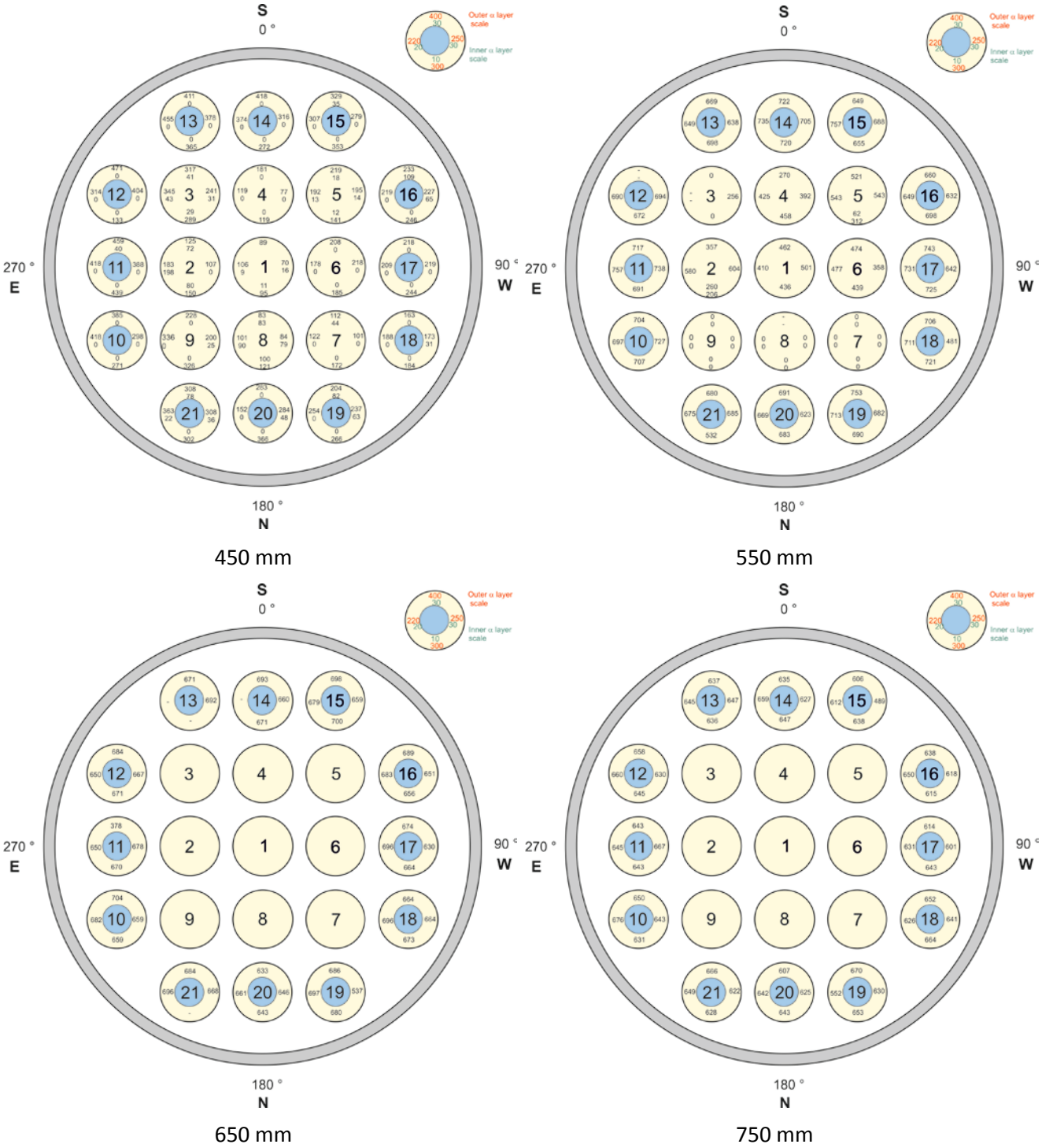

Figure 71 QUENCH-17; thicknesses of α-Zr(O) (inner nine rods) and α-Hf(O) (outer twelve rods) layers.

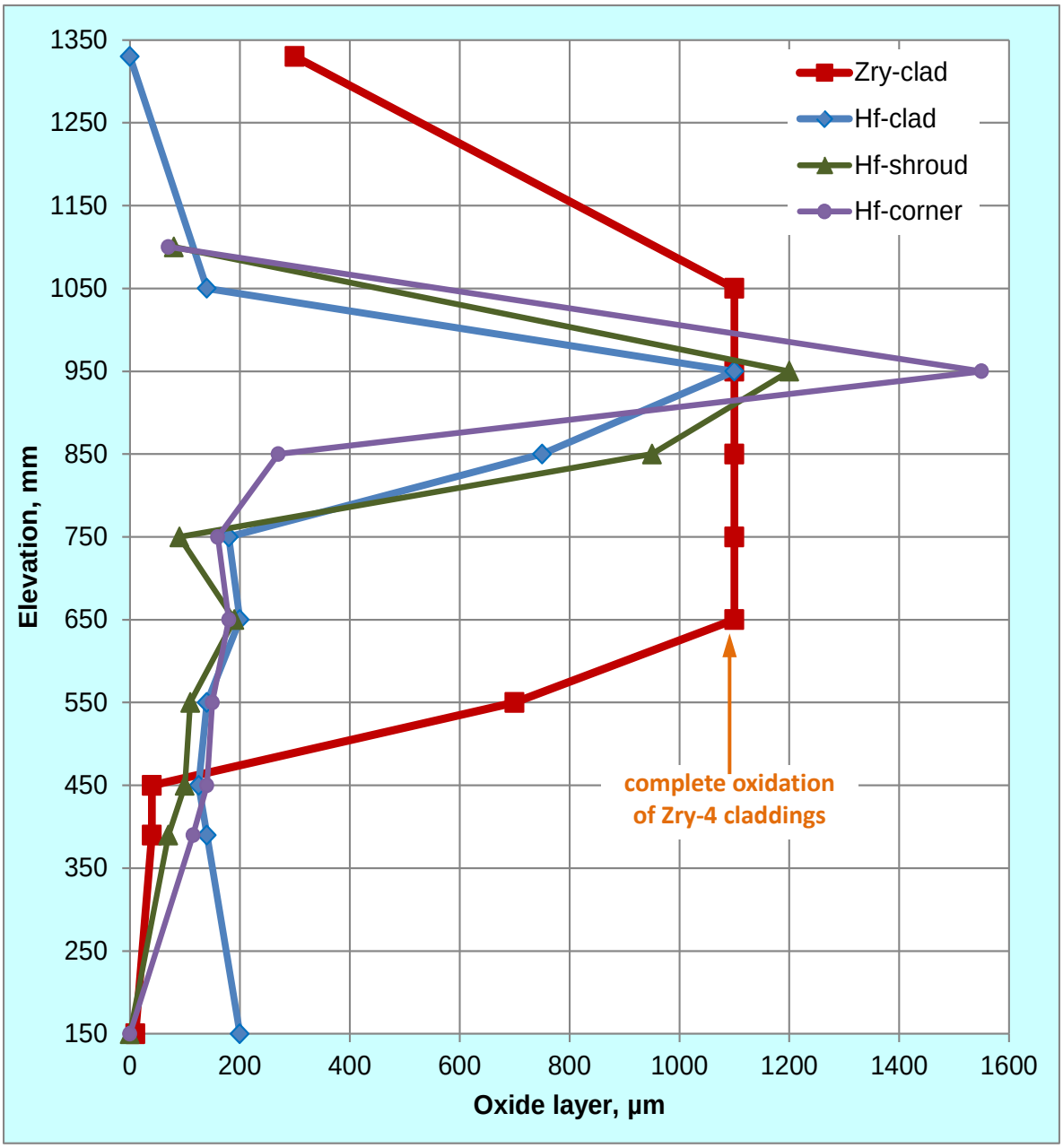

Figure 72 QUENCH-17; axial distribution of outer oxide layers (if not completely oxidized)

Figure 73 QUENCH-17; debris collected at the top of grid spacer #3 (1090 mm)

In the framework of the SARNET-2 European program the QUENCH-DEBRIS test was conducted as the 17th severe accident test using the QUENCH facility at KIT to investigate the formation and coolability of a prototypic debris bed. The test bundle with length of about 2 m contains the hafnium shroud tube and 12 heated peripheral rods with claddings made of hafnium. Hafnium was chosen because of its much higher melting temperature and the about one order of magnitude lower oxidation rate compared to zirconium. The claddings of the inner nine rods were made from Zry-4. They were filled with pre-fragmented zirconia pellets. The test started with an oxidation phase of 20 h at peak cladding temperature about 1800 K to reach complete oxidation of the Zry-4 claddings over a height of 500 mm. The temperatures expected from the pre-test simulation fitted well the experimentally observed evolution of the bundle conditions.

The possibly surviving inner Zry-4 claddings were destroyed by the application of an axial mechanical force resulting in material relocation and formation of a heterogeneous debris bed consisting of segmented pellets and larger cladding tube fragments at the grid spacer #2 (350 mm bundle elevation) and in a smaller amount at grid spacer #3 (1050 mm elevation). The so destroyed bundle was quenched with 10 g/s water. The evaporation rate generally showed an increasing trend during the reflood, except at the time of water penetration through the debris bed at spacer #2 when stagnation was observed. During the oxidation phase about 100 g hydrogen was released.

The post-test examinations comprised videoscope inspections, high energy X-ray-tomography and metallographic investigations. Most of the Zry-4 claddings experienced relatively limited damage, and there was generally only minor damage of the geometrical integrity of the internal 9 rod sub-assembly. All peripheral hafnium claddings survived the whole test. The oxidation degree of Hf claddings inside the high temperature region of the bundle was noticeably lower compared with the oxidation of Zry claddings. The porosity of the debris bed was significant, no dense packing of debris particles was observed. Large empty volumes formed due to bending of rods.